# Towards holographic models for atoms at unitarity

Cover designed by Bastiaan Schravendeel
ISBN: 978-94-6380-213-0
Printed by: ProefschriftMaken || www.proefschriftmaken.nl

# Towards holographic models for atoms at unitarity

Op weg naar holografische modellen voor unitaire atomen

(met een samenvatting in het Nederlands)

Proefschrift

ter verkrijging van de graad van doctor aan de Universiteit Utrecht op gezag van de rector magnificus, prof. dr. H. R. B. M. Kummeling, ingevolge het besluit van het college voor promoties in het openbaar te verdedigen op maandag 28 januari 2019 des middags te 12.45 uur

door

Nicholas William Maria Plantz

geboren op 1 maart 1991
te Best

Promotor: prof. dr. ir. H.T.C. Stoof

# Contents

# List of Publications

The content of the following chapters is based on the following work.

- **Chapter 2** is based on parts of:

  N.W.M. Plantz, H.T.C. Stoof and S.J.G. Vandoren, "Order parameter fluctuations in the holographic superconductor," Journal of Physics B: Atomic, Molecular and Optical Physics **50**, 064001 (2017) [1]

- **Chapter 3** is based on:

  N.W.M. Plantz, F. García Flórez and H.T.C. Stoof, "Massive Dirac fermions from holography," Journal of High Energy Physics **2018**, 123 (2018) [2]

- **Chapter 4** is based on:

  N.W.M. Plantz and H.T.C. Stoof, "Nonrelativistic fermions with holographic interactions and the unitary Fermi gas," accepted for publication in Phys. Rev. A, arXiv:1810.09759 [3]

Chapter 5 is based on ongoing research.

# Preface

This thesis is the result of four years of research, done at the Institute for Theoretical Physics under supervision of prof. dr. ir. Henk Stoof.

Although not without struggles, this research has been conducted with much zeal and ardor and I am pleased to share its results with the reader.

Nick Plantz
November 2018, Utrecht

# 1 Introduction

As suggested by its title, this is a thesis on holography. The majority of people will associate this with the science of creating holograms, which encode all information about some three-dimensional structure on a two-dimensional image. While the most famous examples of such holograms often occur in science fiction, there are also many practical applications. For example, our credit cards contain holograms that are used for authentication purposes. Moreover, according to some media, a hologram of the late Ronnie James Dio is currently being used in live concerts.[1] In 1971, Dennis Gabor was awarded the Nobel Prize in Physics for inventing the holographic method.

About twenty years later, holography gained an alternative meaning in the context of the so-called holographic principle of quantum gravity [4, 5]. A particular case of this principle, called the AdS/CFT correspondence [6], roughly states that some physical systems without gravity in $d$ dimensions have an equivalent description in terms of a theory with gravity in $d+1$ dimensions. Because of the difference in dimensions, the former could then be seen as a holographic image of the latter.[2] Therefore, this correspondence is also known under the name of holography. In this thesis we aim to use this alternative meaning of holography to construct a model for ultracold atomic gases at unitarity.

## 1.1 Unitary gases

First and foremost, let us illustrate the physical systems that we ultimately want to study in this thesis. These are *ultracold*, *strongly interacting*, *atomic* gases. We start by discussing the meaning of these three italicized adjectives (and the adverb) in more detail.

[1] This is actually fake news: the hologram of Dio is not really a hologram, but rather an image created by the so-called Pepper's ghost illusion technique.

[2] Although this has led to many claims that the world we live in is a hologram, it is better to view this nomenclature as just a metaphor.

## Winter is coming

How cold is *ultracold*? Typically, experiments involving ultracold gases are carried out at temperatures that range from nanokelvins to microkelvins, although even temperatures of the order of tens to hundreds of picokelvins have been achieved [7, 8]. Given that a winter night below 250 K is usually already considered quite cold, this indeed validates the use of the prefix 'ultra'. Another justification for this can be found by comparing to the cosmic microwave background radiation, which has a temperature of about 3 K.

Nevertheless, in physics we do not usually compare quantities with an arbitrary everyday scale, such as a winter night's temperature. Instead, we compare with the other relevant scales that are present in the physical system of interest. A physically more interesting observation can be found by considering the interaction potential between the atoms. For ultracold gases, the range $R$ of this potential is typically much smaller than the thermal de Broglie wavelength $\Lambda_{\mathrm{th}}$, which scales as $T^{-1/2}$. In particular, the temperature $T$ in these gases is such that the typical energy corresponding to two scattering atoms is too low to overcome the centrifugal barrier[3] that has to be added to the interaction potential, even for orbital quantum number $l = 1$. The collision processes between two atoms are therefore dominated by $s$-wave scattering, for which $l = 0$ and this barrier vanishes. This leads to the important conclusion that we can use the $s$-wave scattering length $a$ as a parameter that completely determines the interatomic interactions in these systems. As we shall see later, this scattering length can diverge. When this happens, the system is said to be at unitarity.[4]

The next relevant scale is set by the density $n$, or equivalently the average

[3] As a reminder, this barrier is proportional to $l(l+1)$.

[4] This nomenclature stems from the following. When calculating the scattering amplitude $f_k$ of two atoms in the gas with a relative momentum of magnitude $\hbar k$, one can show that conservation of probability requires that $|1 + 2ikf_k| = 1$ [9] and furthermore that this in the long-wavelength limit leads to

$$f_k \simeq \frac{-1}{a^{-1} + ik}. \tag{1.1}$$

As a consequence, the largest value of $|f_k|$ that is allowed by the unitarity of the evolution operator is given by $|f_k| = 1/k$, which is attained in the unitarity limit $a \to \infty$, i.e., when the scattering length diverges.

interparticle spacing $d \simeq n^{-1/3}$. Ultracold gases are normally very dilute, which means that also $d$ is much larger than the range of the interaction potential $R$. However, as the temperature is very low in these systems, we can have that $d \simeq \Lambda_{\mathrm{th}}$. This means that the temperature is of the order of the critical temperature at which the system becomes quantum degenerate, i.e., quantum statistics become important.

## Fermions vs. bosons

Another adjective we promised to discuss is *atomic*. Needless to say, this implies that the constituents of the ultracold gas are atoms. The important distinction we should make is between bosonic and fermionic atoms. In comparison to unitary bosons, unitary Fermi gases have been studied much more extensively in the lab. Although there is also much interest in the experimental realization of a unitary Bose gas, this turns out to be more complicated to achieve, owing to the so-called Efimov effect.

In 1970, Efimov predicted the existence of a set of three-body bound states in a system of bosons near the resonance of a two-body interaction that occurs at unitarity [10]. Approaching the resonance at $1/a = 0$ from below, the first of such three-body states already appears at some finite value $a_1 < 0$, where no two-body bound state exists. Increasing $a$ gives rise to more trimer states, where the scattering length at which the $n$th state appears is given by $a_n \simeq 22.7 a_{n-1}$. Moreover, the energy of these states obeys $E_n \simeq E_{n-1}/22.7^2$ [11, 12]. According to this, at unitarity an infinite amount of Efimov trimers should exist, whose binding energies can become arbitrarily low. Such Efimov states have indeed been observed in experiments with ultracold Bose gases at strong coupling [13, 14].

The existence of these Efimov states negatively impacts the lifetime of a unitary Bose gas. This is because when three atoms collide and a bound state is formed, the increase in kinetic energy to compensate the binding energy is often enough for the atoms to escape the trapping potential of the cloud. This leads to a three-body loss rate $L_3$ defined by

$$\dot{N}/N = -L_3 \left\langle n^2 \right\rangle , \tag{1.2}$$

where $\dot{N}$ denotes the derivative with respect to time of the particle number $N$ and the brackets denote a trap average. For a dilute gas at zero temperature

this loss rate follows the scaling behavior [11][5]

$$L_3 \propto a^4. \tag{1.3}$$

This indeed leads to quite a leviathan loss rate as the unitarity limit is approached. On the other hand, at nonzero temperature the loss rate remains finite as $a \to \infty$, but then it scales as [15–17]

$$L_3 \propto \Lambda_{\mathrm{th}}^4 \propto T^{-2}, \tag{1.4}$$

which still strongly enhances the loss near resonance at extremely low tempatures. Although this loss rate impedes the experimental realization of a metastable unitary Bose gas, many experimental attempts have been performed [17–19].

## Controlling scattering and creating universality

As mentioned before, the $s$-wave scattering length $a$ plays the role of the relevant measure for the interactions in ultracold gases. *Strongly interacting*, the final phrase we promised to discuss, therefore means that $|a|$ is large, in fact even much larger than the interparticle distance $d$. In this thesis we are particularly interested in the unitarity limit, where $a$ diverges. Such a resonance already occurs for simple interaction potentials such as a spherical well with depth $-|V_0|$ and radius $R$. Solving the radial Schrödinger equation for the relative motion of the two scattering atoms with this potential yields a scattering length [20]

$$a = R\left(1 - \frac{\tan\sqrt{|\tilde{V}_0|}}{\sqrt{|\tilde{V}_0|}}\right), \tag{1.5}$$

where we defined the dimensionless interaction strength $\tilde{V}_0 \equiv mR^2V_0/\hbar^2$ of the potential, with $m$ the atomic mass. The resonance can be seen in Fig. 1.1. Also shown in this figure is the energy of the bound state that exists for the shown values of $V_0$. We see that the resonance occurs at the same point at which this weakly bound state appears.

[5] Here and in eq. (1.4) we ignore a prefactor that is log-periodic in $a$ and $T$ respectively, due to the Efimov tower of trimer states.

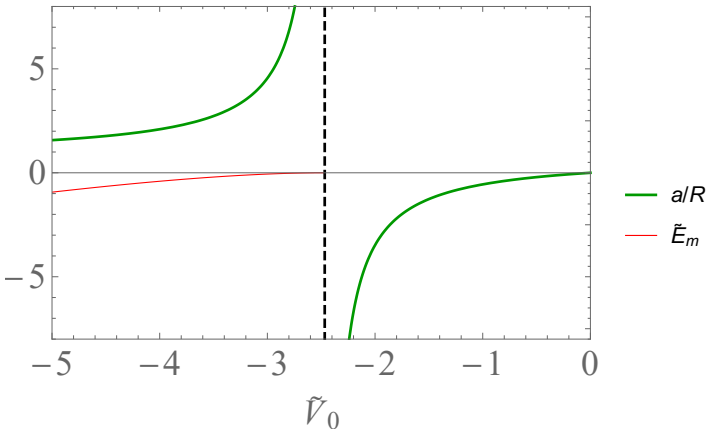


Figure 1.1: The scattering length $a$ and the dimensionless molecular bound-state energy $\tilde{E}_m \equiv mR^2E_m/\hbar^2$ for the spherical-well potential as a function of the dimensionless interaction strength $\tilde{V}_0 \equiv mR^2V_0/\hbar^2$. The black dashed line denotes the location of the resonance. Close to the resonance, the energy of the bound state is given by $E_m = -\hbar^2/ma^2$ with $a \geq 0$.

In 1993 [21], it was discovered that it should be possible to gain experimental control over the energy difference between the weakly bound state and the continuum threshold of the two colliding atoms at $E = 0$ by using a so-called Feshbach resonance.[6] Here one uses a molecular state that differs from the two scattering atoms in its magnetic moment, which leads to different Zeeman shifts when applying a magnetic field. Quite amazingly, this has the consequence that it is possible to effectively tune the scattering length in these systems by simply applying a magnetic field. This was verified experimentally five years later in Ref. [23] in an ultracold gas of sodium atoms, as shown in Fig. 1.2. The effective scattering length $a(B)$ in this system is now given by

$$a(B) = a_{\mathrm{bg}}\left(1 - \frac{\Delta}{B - B_0}\right), \tag{1.6}$$

[6] Herman Feshbach's field of research was actually nuclear physics. Ironically, when a colleague who had just read the term 'Feshbach resonance' in a paper came to ask Feshbach what it was, his first reaction was 'Beats me!'. It is, however, unknown whether this was a joke [22].

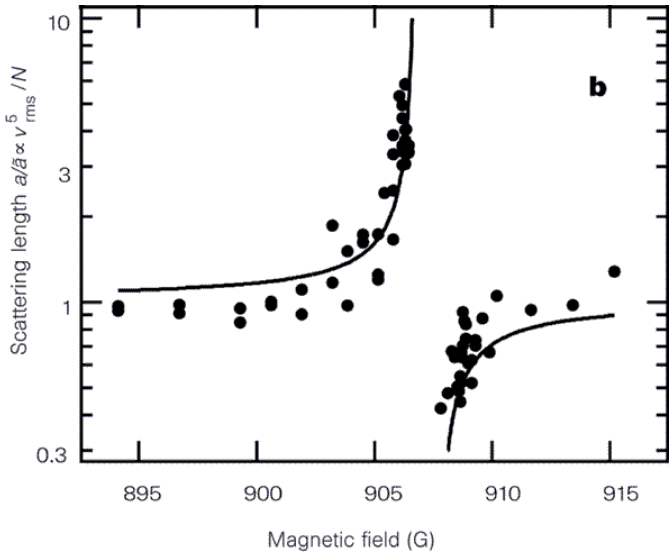


Figure 1.2: Experimental observation of a Feshbach resonance. Here the scattering length $a$ is normalized by its background value $a_{\mathrm{bg}}$ that appears in eq. (1.6). Reprinted by permission from Springer Nature Customer Service Centre GmbH: Springer Nature, Nature, *Observation of Feshbach resonances in a Bose–Einstein condensate*, S. Inouye, M. R. Andrews, J. Stenger, H.-J. Miesner, D. M. Stamper-Kurn et al., copyright 1998 [23].

where $a_{\mathrm{bg}}$ is the scattering length away from the resonance and $\Delta$ and $B_0$ are the width and the position of the resonance respectively. Note that this is indeed very similar to the situation that occurs in Fig. 1.1, the main difference being that the magnetic field strength now effectively allows for experimental control over the interaction strength $V_0$.

This exceptional experimental control over the scattering properties has made ultracold gases an ultrahot research topic. It has for example led to many studies on the transition from the BCS regime where $1/k_F a < -1$, to the BEC regime where $1/k_F a > 1$ [24–29]. Here $k_F$ is the Fermi wavenumber, which at zero temperature is fixed by the density by $k_F^3 = 6\pi^2 n/(2s+1)$ with $2s+1$ the spin degeneracy. Note that we use this definition also for bosonic gases in the following. Furthermore, it is possible to create ultracold gases at strong coupling by tuning the magnetic field near the value $B_0$ in eq. (1.6),

and in particular we can study the properties of the gas at unitarity.

An interesting feature of unitary gases is that the only two relevant length scales that are left are the thermal de Broglie wavelength $\Lambda_{\rm th}$ and the interatomic spacing $d \propto k_F^{-1}$ that is set by the density $n$.[7] At zero temperature $d$ is the only scale left. Consequently, all dimensionless thermodynamic quantities, such as the ratio $\mu/\epsilon_F$ of the chemical potential and the Fermi energy $\epsilon_F = \hbar^2 k_F^2/2m$, must become constants. In other words, the thermodynamic properties of unitary gases are universal [30]. These universal constants can be measured in experiments. Theoretically, we can already demonstrate the universality by for simplicity considering fermions described by BCS theory in the unitarity limit. This theory is based on the BCS wave function for the many-body ground state

$$|\Psi_{\rm BCS}\rangle = \prod_{\mathbf{k}} \left( u_{\mathbf{k}} + v_{\mathbf{k}} \psi^\dagger_{\mathbf{k},\uparrow} \psi^\dagger_{-\mathbf{k},\downarrow} \right) |0\rangle \,, \tag{1.7}$$

where $\psi^\dagger_{\mathbf{k},\sigma}$ creates an atom with momentum $\hbar\mathbf{k}$ and spin $\sigma$. Minimizing the energy with respect to the coefficients $u_{\mathbf{k}}$ and $v_{\mathbf{k}}$ then yields the famous gap equation and the equation for the density [31]. In this manner we obtain at zero temperature that

$$\frac{-m}{2\pi\hbar^2 a} = \int \frac{\mathrm{d}^3\mathbf{k}}{(2\pi)^3} \left( \frac{1}{\sqrt{(\epsilon_{\mathbf{k}} - \mu)^2 + \Delta^2}} - \frac{1}{\epsilon_{\mathbf{k}}} \right), \tag{1.8}$$

$$n = \int \frac{\mathrm{d}^3\mathbf{k}}{(2\pi)^3} \left( 1 - \frac{\epsilon_{\mathbf{k}} - \mu}{\sqrt{(\epsilon_{\mathbf{k}} - \mu)^2 + \Delta^2}} \right). \tag{1.9}$$

Here $\epsilon_{\mathbf{k}} = \hbar^2 k^2/2m$ with $k = |\mathbf{k}|$ and the gap $\Delta$ is the order parameter of BCS theory. We note that the integrand in eq. (1.9) gives the momentum distribution. For any given value of $k_F a$, the system above can be solved for $\mu$ and $\Delta$ in terms of the Fermi energy. In particular, at unitarity the left-hand side of eq. (1.8) vanishes, so that we can write it as

$$\int_0^\infty \mathrm{d}\overline{k} \left( 1 - \frac{\overline{k}^2}{\sqrt{\left(\overline{k}^2 - x\right)^2 + 1}} \right) = 0, \tag{1.10}$$

[7] Note that here we once again assume that $k_F R \ll 1$, i.e., the range of the interaction potential is negligible. However, for an atomic Bose gas $R$ could in fact play a role when including Efimov physics.

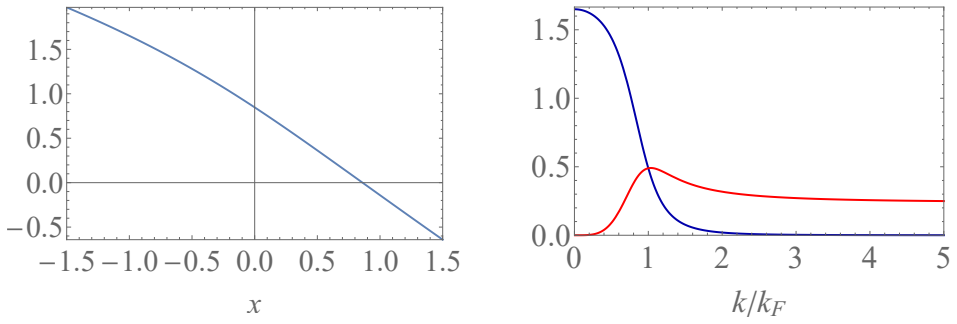


(a) (b)

Figure 1.3: (a) The left-hand side of eq. (1.10) as a function of $x = \mu/\Delta$. Finding the root of this function shows that eq. (1.10) holds for $x \simeq 0.86$. (b) The momentum distribution as a function of $k/k_F$, where the red curve was obtained by multiplying the blue curve by $k^4/k_F^4$ to reveal the asymptotic behavior. The contact parameter that follows from this is $C/k_F^4 \simeq 0.24$, or in terms of the chemical potential, $C\hbar^4/\mu^2 m^2 \simeq 2.7$.

where $\overline{k} \equiv \hbar k/\sqrt{2m\Delta}$ and $x \equiv \mu/\Delta$. This can be numerically solved for $x$ to find $x \simeq 0.86$, as shown in Fig. 1.3a. After this we can write eq. (1.9) as

$$y \equiv \left(\frac{\Delta}{\epsilon_F}\right)^{-\frac{3}{2}} = \frac{3}{2}\int_0^\infty \mathrm{d}\overline{k}\,\overline{k}^2 \left(1 - \frac{\overline{k}^2 - x}{\sqrt{\left(\overline{k}^2 - x\right)^2 + 1}}\right) \simeq 1.76, \qquad (1.11)$$

which we have evaluated numerically using the previously found value for $x$. We therefore indeed find that dimensionless quantities such as $x$ and $\Delta/\epsilon_F = y^{-2/3}$ are universal numbers, i.e., they do not depend on what species of atoms the gas consists of. Moreover, we can now plot the momentum distribution as shown in Fig. 1.3b, which asymptotically behaves as $C/k^4$. This universal behavior defines the contact parameter $C$ [32], which has also been measured experimentally at unitarity [33].

We can use the obtained values of the constants $x$ and $y$ above to calculate some other common dimensionless constants for unitary gases. These include $\xi$ and $\beta$ that are defined by $\Delta = \xi\epsilon_F$ and $\mu = (1+\beta)\epsilon_F$. From BCS theory we obtain that $\xi = y^{-2/3} \simeq 0.69$ and $\beta = xy^{-2/3} - 1 \simeq -0.41$. We can compare this to the experimental values $\xi \simeq 0.5$ and $\beta \simeq -0.6$ that were obtained in

unitary Fermi gases [27, 28, 34]. The difference is easily explained, since BCS theory corresponds to the weakly interacting regime $1/k_F a \ll 1$, so that BCS theory is not expected to hold at unitarity. Theoretically, it is challenging to compute these universal constants more precisely, as we cannot perform perturbation theory in the strongly interacting regime. Nevertheless, more elaborate models based on for example Monte-Carlo simulations [35, 36] and renormalization-group methods [37] have been able to reproduce the above experimental values of the constants.

If, despite the complications caused by Efimov physics, it is possible to create a metastable Bose gas at unitarity, then these Bose gases are also expected to exhibit universal properties. However, the universal constants such as $\beta \equiv -1 + \mu/\epsilon_F$ will have different values from their fermionic counterparts, as the constituents of the Bose gas obey different statistics. Still, for comparison to the currently available experiments it may prove necessary to include the three-body effects if we wish to model unitary bosons. This spoils the universality, as this introduces an additional scale to the system which is dependent on the atomic species [11]. On a positive note, the inclusion of Efimov physics also introduces many new interesting phenomena, such as a much richer phase diagram [38].

## 1.2 Holography

Having explained our physical system of interest, we now turn to our computational tool. This is based on a completely different physical theory than quantum mechanics, namely general relativity. The central object of this theory is the metric $g_{\mu\nu}$ that determines the geometry of the spacetime. In particular, we will be interested in theories of gravity described by the action

$$S = \frac{c^3}{16\pi G_{d+1}} \int \mathrm{d}^{d+1}x\sqrt{-g}\,(R - 2\Lambda)\,, \tag{1.12}$$

with $G_{d+1}$ Newton's gravitational constant in $d+1$ spacetime dimensions, $R$ the Ricci scalar and $g$ the determinant of the metric. Most importantly, the action includes a cosmological constant $\Lambda$ that is negative, as opposed to the one in the universe we live in. The spacetime corresponding to the above action is the so-called anti-de Sitter spacetime,[8] often abbreviated as

[8] For now we ignore the black-hole solutions.

$\mathrm{AdS}_{d+1}$, or simply AdS.

What makes this spacetime useful to us, is that it is conjectured to be dual to a strongly coupled conformal field theory (CFT) in $d$ spacetime dimensions, which lives on the (conformal) boundary of the AdS spacetime. This conjecture originates from string theory and is known as the AdS/CFT correspondence, or sometimes as gauge/gravity duality or holography. More precisely, the original form of this conjecture states that a type IIB string theory on a $\mathrm{AdS}_5 \times \mathrm{S}^5$ spacetime is dual to $\mathcal{N} = 4$ supersymmetric Yang-Mills theory in four spacetime dimensions [6]. This means that it is possible to compute quantities in this CFT by performing calculations in the string theory. Moreover, the latter can be reduced to general-relativity calculations by taking the low-energy limit and the classical limit of the string theory. The duality then tells us that in this limit the CFT becomes (infinitely) strongly coupled and that the number of colors $N_c$ in the CFT goes to infinity. The latter is known as the large-$N$ limit, where $N$ is the number of degrees of freedom in the CFT.

Stringy details aside, the point here is that the AdS/CFT correspondence provides a tool of describing strongly coupled, scale-invariant field theories, with a large number of degrees of freedom. Nevertheless, from a condensed-matter perspective it would be more interesting to describe other field theories than the supersymmetric one above. In principle, the way to go is then to start from a string theory such as the above-mentioned one and modify it a bit, which hopefully results in a more interesting CFT. Although this approach, called the top-down approach, yields precise results on the CFT side, it is in practice intractable to perform the modifications needed to arrive at a field theory that describes a certain system of interest.

In this thesis we therefore exclusively employ the alternative bottom-up approach to the duality. This is based on the more general holographic principle that relates an (asymptotically) $\mathrm{AdS}_{d+1}$ spacetime to a strongly coupled field theory in $d$ dimensions, without explicitly invoking string theory. Equating the partition functions of these theories, the large-$N$ limit then implies that the free energy of the field theory can be found from the on-shell action of the AdS spacetime. The calculational tool that is central

to this bottom-up approach is given by the celebrated GKPW[9] rule [39, 40]

$$\left\langle e^{i\int \mathrm{d}^d x J(x)\mathcal{O}(x)} \right\rangle_{\mathrm{CFT}} = e^{iS_{\mathrm{AdS}}[\phi\to J]/\hbar}. \tag{1.13}$$

Basically, this tells us that we can deform the CFT by an operator $\mathcal{O}$, that is sourced by $J$, by adding a field $\phi$ to the AdS spacetime which has this source $J$ as its on-shell boundary value. The latter is implied by the notation $S_{\mathrm{AdS}}[\phi \to J]$.[10] The GKPW rule then gives us the generating functional, so that we can calculate all the correlation functions of $\mathcal{O}$ by studying fluctuations of the scalar field in the gravity theory. This procedure is discussed in more detail in chapter 2.

The plan of action of bottom-up holography is then as follows. We start with an AdS spacetime, also known as the bulk, described by the action in eq. (1.12). Next, we introduce additional content to the bulk in order to introduce the desired deformations in the CFT. To find out exactly what should be added to the gravity theory, we appeal to the so-called holographic dictionary, which is based on the GKPW rule and translates between quantities in the field theory and their gravitational duals. Below, we list some entries taken from this dictionary that we will use in this thesis.

- To introduce a temperature in the boundary theory, we must add a black hole to the bulk. The temperature is then given by the Hawking temperature of this black hole.

- To study the field theory at a nonzero chemical potential, we must add a $U(1)$ gauge field to the gravity theory. This is part of a more general entry, which states that a global symmetry on the boundary is dual to a local symmetry in the bulk.

- A scalar field in the bulk is dual to a composite scalar operator on the boundary. The bulk mass of the scalar field determines the conformal dimension of the operator. A specific case of this entry can be used to introduce a mass deformation in the boundary [41], as we discuss in more detail in chapter 3 and chapter 5.

[9] Named after Gubser, Klebanov, Polyakov and Witten.

[10] More precisely, the source is in general not equal to the value of $\phi$ at the boundary, but it is found from the near-boundary behavior of $\phi$ on shell.

- A Dirac spinor in the bulk is dual to a chiral operator on the boundary.[11] Therefore, to get a Dirac fermion on the boundary, we need two Dirac spinors in the bulk, as we show in chapter 3.

Finally, having added all the necessary ingredients to the bulk, we apply the GKPW rule once again to compute the correlation functions in the boundary theory.

A drawback of the bottom-up approach is that it yields expectation values of composite operators in the CFT, whose microscopic origin remains concealed. It is therefore a more phenomenological approach to holography than the top-down path. The obvious advantage is that it leads to less sophisticated models, that are given by eq. (1.12) supplemented with the actions of the additional fields and which are already able to reveal many universal features of physical systems. Moreover, it allows us to avoid the behemoth of technical wizardry that arises when truncating string theories. Nonetheless, we should keep in mind that the mathematical validity of bottom-up models depends on the existence of an embedding of the bulk in a higher-dimensional string theory.

## 1.3 Unitary gases with holographic interactions

In the previous sections, we described the physical system we are interested in and the computational tool we are going to apply. What makes atomic gases at unitary suitable for a description based on holographic machinery? For starters, unitary gases are strongly coupled systems, in which the attractive interactions between the atoms diverge. Furthermore, as we have seen in section 1.1, at unitarity the thermodynamic properties of the system become universal. This is a consequence of the system being almost scale invariant, meaning that the only scale in these gases at zero temperature is set by the density. In section 1.2 we have seen that holography is used to describe exactly this type of theories. In particular, it enables us to compute universal features of (deformed) scale invariant theories at strong coupling. Combined with the fact that these systems can be experimentally

[11] This is true for the examples considered in this thesis, where the number of spacetime dimensions of the boundary theory is $d = 4$. For odd $d$, however, we get a Dirac fermion on the boundary.

realized using Feshbach resonances, ultracold gases at unitarity thus present a benchmark problem for experimental tests of the holographic principle.

Naturally, before we can make sense of any comparison with experiments, we need to compute something that is experimentally measurable. Therefore, a prominent quantity in this thesis is the single-particle spectral function $\rho(\omega, \mathbf{k})$, which in atomic gases can be measured using radio-frequency spectroscopy. It is found from the imaginary part of the single-particle Green's function and satisfies a frequency sum rule which in our conventions reads

$$\int \mathrm{d}\omega \rho(\omega, \mathbf{k}) = f, \tag{1.14}$$

with $f$ the number of degrees of freedom, e.g., $f = 4$ for a Dirac fermion, $f = 2$ for a nonrelativistic spin-1/2 particle and $f = 1$ for a nonrelativistic spinless particle. To compute such a spectral-weight function, we consider an elementary field $\psi$ and couple it to a composite operator $\mathcal{O}$ that lives in a strongly interacting CFT with a large amount of degrees of freedom $N$. The corresponding action is given by

$$S = \int \frac{\mathrm{d}^4 k}{(2\pi)^4} \left( \psi^\dagger(k) G_0(k)^{-1} \psi(k) + g\psi^\dagger(k)\mathcal{O}(k) + g\mathcal{O}^\dagger(k)\psi(k) \right) + S_{\mathrm{CFT}}, \tag{1.15}$$

where $g$ is a coupling constant, $G_0$ is the noninteracting Green's function of $\psi$ and $S_{\mathrm{CFT}}$ is the action governing the (deformed) CFT. Although the microscopic interpretation of the composite operator $\mathcal{O}$ is camouflaged by the bottom-up approach, from a condensed-matter perspective we think of it as part of a CFT that is described by collective variables of $\psi$. We can now integrate out the CFT to obtain the effective action

$$S_{\mathrm{eff}} = \int \frac{\mathrm{d}^4 k}{(2\pi)^4} \psi^\dagger(k) \left( G_0(k)^{-1} - \Sigma(k) \right) \psi(k), \tag{1.16}$$

where the self-energy $\Sigma(k) = g^2 G_{\mathcal{O}}(k)$ is given by the two-point function of $\mathcal{O}$, because the large-$N$ limit suppresses the connected parts of $n$-point functions for $n > 2$. This is the point where holography comes in, which we use to compute the two-point function $G_{\mathcal{O}}$ by means of the GKPW rule mentioned in section 1.2. This approach, in which we use holography to describe the self-energy of an elementary field, is also known as semiholography. In chapter 3 and 5 we discuss how to implement this approach in the bulk, in such

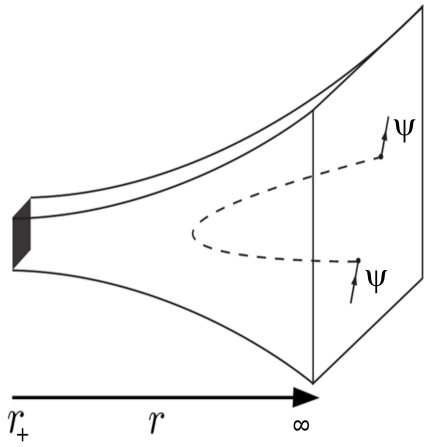


Figure 1.4: Illustration of the method used to find the Green's function for $\psi$ with holographic interactions. Here the self-energy, depicted by the dashed curve, is found by linearly coupling the field $\psi$ to the CFT through the operator $\mathcal{O}$. Essentially, the self-energy is then computed by having the field probe into the gravitational bulk that is dual to the CFT in which $\mathcal{O}$ lives. Here $r$ is the additional radial coordinate of the bulk theory, such that the boundary is at $r = \infty$ and there is a black-hole horizon at $r = r_+$.

a way that the appropriate sum rule is satisfied by construction. Because holography usually describes relativistic theories, note that the field $\psi$ above is also relativistic, such as a Klein-Gordon field or a Dirac spinor. Thus, to obtain the spectral function for a single atom from this procedure, we must take the nonrelativistic limit, which we discuss in chapter 4 for the fermionic case.

The ultimate goal of this thesis is to model the universal properties of unitary gases by computing single-atom spectral functions with this procedure. Note that we can obtain the universal thermodynamic properties from these spectral functions by firstly finding the momentum distributions

$$N(\mathbf{k}) = \int \mathrm{d}\omega \rho(\omega, \mathbf{k}) n_{B/F}(\omega), \tag{1.17}$$

with $n_{B/F}$ the Bose-Einstein or Fermi-Dirac distribution respectively, and

subsequently use these to find the density

$$n = \int \frac{\mathrm{d}^3\mathbf{k}}{(2\pi)^3} N(\mathbf{k}). \tag{1.18}$$

This density as a function of temperature and chemical potential gives us the equation of state, from which all thermodynamic functions follow.

## 1.4 Outline of the thesis

As stated, our holy grail is the construction of a holographic model for unitary atoms. This thesis presents our progress towards this achievement. Basically, we can subdivide the road towards this goal in three steps:

1. Construct a CFT by finding a suitable gravitational background
2. Add probe fields on top of this background to compute single-particle spectra containing a mass gap
3. Take the nonrelativistic limit of the spectra by making the mass gap large

Each of the following three chapters can be thought of as a single step in this process for the unitary Fermi gas.

In more detail, in chapter 2 we discuss the holographic superconductor, which is one of the first attempts to describe a condensed-matter system using the AdS/CFT-correspondence. Although we already study some spectral functions in this chapter, the main importance of this chapter for the rest of this thesis is to provide an extensive discussion of the gravitational background of the holographic superconductor. Hence, this chapter represents step 1 above, as this background is very similar to the one that is used in the other chapters.

In particular, in chapter 3, which represents step 2 above, we use a similar background to obtain spectra of Dirac fermions from holography that include a mass gap. Since recently it has been discovered that also a number of electronic condensed-matter systems have an effective description in terms of Dirac theory, this chapter also discusses the interpretation of our obtained spectra in this perspective.

In chapter 4 we then use the method from chapter 3 to prepare spectral functions that contain a mass gap and subsequently study the nonrelativistic limit of such spectral functions, thereby completing step 3. We also discuss the equation of state that results from these spectral functions of nonrelativistic fermions.

As an encore, chapter 5 contains some first results of our ongoing research to apply the above three-step process to bosons as well.

# 2 The holographic superconductor background

## 2.1 Introduction

Ginzburg-Landau theory [42] has been used to describe physics near a conventional superconducting phase transition with great success. Based on the Landau approach to continuous phase transitions, it makes use of a complex order parameter which acquires a nonzero expectation value in the superconducting phase. As this is a phenomenological model, a microscopic interpretation of the order parameter was not included. This interpretation was provided by Gor'kov several years after the Ginzburg-Landau theory [43], using the microscopic model of superconductivity by Bardeen, Cooper, and Schrieffer [31]. Here, superconductivity is described as the condensation of Cooper pairs, which consist of a pair of electrons on top of a filled Fermi sea, bound together due to a phonon-mediated attractive interaction. By elegantly using a variational *Ansatz* for the BCS ground state, BCS mean-field theory has succeeded in producing many accurate quantitative results that have been confirmed experimentally in weakly coupled superconductors.

As BCS mean-field theory only describes superconductors in the weakly coupled regime, several different approaches have been used to study strongly coupled superconductors. One example of such an approach is Eliashberg theory, which goes beyond the BCS mean-field theory by providing a more accurate treatment of the phonons interacting with the electrons. The self-energy due to these interactions now includes retardation effects, in contrast to the BCS model. Consequently, the Eliashberg formalism is able to provide more accurate quantitative results [44] than the BCS formalism. However, in the class of high-temperature superconductors, the pairing mechanism cannot be described by means of interactions with phonons. Therefore even the Eliashberg approach is inapplicable and methods to describe high-temperature superconductors remain mysterious. Fermion gases at unitarity

are superconductors at infinite coupling.[1] These have been described by numerical approaches based on the quantum Monte Carlo method [45–47]. Moreover, an analytical description by means of renormalization group theory can be found in Ref. [37].

A novel approach to strongly coupled systems, which has become very popular over the past decade, is the use of the holographic duality. Inspired by ideas in Refs. [48, 49], a bottom-up approach of the AdS/CFT correspondence to superconductivity was first given in Ref. [50], followed by many other papers [51]. One of the most used models within this framework describes the superconducting phase transition as the condensation of some complex order parameter in the boundary theory that arises from a dual complex scalar field in the classical gravitational theory. From this model, many characteristics of superconductivity have been reproduced, such as the diverging DC conductivity, an energy gap, and a Meissner effect [52]. The microscopic interpretation of the order parameter is not known, since bottom-up holography usually provides us with expectation values of unknown composite operators rather than the single-particle or single-pair operators which naturally arise in condensed-matter systems. It is therefore unsurprising that results obtained through this approach are generally different from BCS derivations. However, one might wonder whether a phenomenological Ginzburg-Landau theory can still be applied. The answer to this question seems positive, based on e.g. the mean-field critical exponents near the transition temperature [53].

The long-term aim of this work is to study ultracold fermion gases at unitarity using a holographic approach. The holographic superconductor mentioned above seems like a logical starting point towards this aim, since this model should in principle also consist of strongly correlated fermions. We therefore study the properties of the holographic superconductor in detail in this paper. The outline is as follows. In section 2.2, we discuss the background theory that will be used throughout this paper. This includes a short review of the holographic superconductor solution and a comparison with a number of universal BCS results. Moreover, our notation and conventions are introduced here. Section 2.3 covers the scalar field fluctuations on top

[1] Although these fermion gases at unitarity consist of Cooper pairs in a condensed state, the Cooper pairs consist of neutral fermions. Therefore the term superfluid may be more appropriate.

of the holographic superconductor background, including the resulting two-point function of the order parameter in the dual theory in the normal phase. Using a gradient expansion we then arrive at a local Ginzburg-Landau theory for the holographic superconductor. A similar calculation was performed in Ref. [54] above the critical temperature. We end with a brief discussion on the superconducting phase in section 2.4.

## 2.2 The holographic superconductor

In this section, we describe the bulk geometry that we use throughout this paper. This geometry was introduced in Ref. [52]. The purpose of this section is to outline its properties that are most relevant to our results, as well as to introduce our notation and conventions. After giving the bulk solutions, we specify on how many and on which parameters this solution exactly depends. We end the section by discussing the superconducting phase transition that appears in the dual field theory and comparing its properties with universal results which follow from BCS theory.

For the sake of generality, we give the gravitational bulk for an arbitrary spatial dimension $d$. However, we will always specify to $d = 4$ when discussing the dual field theory, which then has three spatial dimensions. Although many high-$T_c$ superconductors consist of layers and are thus effectively two-dimensional, we are interested in three-dimensional superconductors here. Examples of these include the ultracold gases at unitarity mentioned in the introduction.

### 2.2.1 The gravity solutions

The gravitational background that we use follows from the action that describes gravity minimally coupled to a $U(1)$ gauge field $A_\mu$ and a charged scalar field $\phi$. In SI units, it is given by

$$S = \int \mathrm{d}^{d+1}x\sqrt{-g}\left[\frac{c^3}{16\pi G}(R-2\Lambda)-\frac{1}{4\mu_0 c}F^2-\left(|D\phi|^2+\frac{m^2c^2}{\hbar^2}|\phi|^2\right)\right]. \quad (2.1)$$

Here the scalar field has mass $m$ and charge $q$. Furthermore, $G$ and $\mu_0$ are Newton's constant and the vacuum permeability in $d$ spatial dimensions respectively. In addition, $\Lambda < 0$ is the cosmological constant and $D_\mu$ is the

gauge covariant derivative

$$D_\mu = \nabla_\mu - \frac{iq}{\hbar} A_\mu \,. \tag{2.2}$$

The equations of motion that follow from this action describe the gauge field and the scalar field backreacting on the geometry. Here, we consider static solutions to these equations, with planar symmetry. The metric *Ansatz* can then be written as [52]

$$\mathrm{d}s^2 = -f(r) e^{-\chi(r)} c^2 \mathrm{d}t^2 + \frac{1}{f(r)} \mathrm{d}r^2 + \frac{r^2}{L^2} \mathrm{d}\mathbf{x}_{d-1}^2 \,, \tag{2.3}$$

where the AdS radius $L$ is given by $L^2 = d(d-1)/(-2\Lambda)$. Here the coordinate $r$ runs from the horizon $r = r_+$, where $f(r_+) = 0$, to the boundary at $r = \infty$. Demanding there to be no conical singularity in the imaginary-time geometry at $r_+$ gives the Hawking temperature

$$k_B T = \frac{\hbar c f'(r_+) e^{-\chi(r_+)/2}}{4\pi} \,, \tag{2.4}$$

where $k_B$ is Boltzmann's constant. Furthermore, the gauge field is temporal, i.e., $A = A_t(r)\mathrm{d}t$, and we choose a gauge in which $\phi$ is real. With these *Ansätze* the equations of motion become

$$\phi'' + \left( \frac{f'}{f} + \frac{d-1}{r} - \frac{\chi'}{2} \right) \phi' - \frac{m^2 c^4 - q^2 A_t^2 \frac{e^\chi}{f}}{\hbar^2 c^2 f} \phi = 0 \,, \tag{2.5}$$

$$A_t'' + \left( \frac{d-1}{r} + \frac{\chi'}{2} \right) A_t' - 2 \frac{q^2 \mu_0 c \phi^2}{\hbar^2 f} A_t = 0 \,, \tag{2.6}$$

$$\chi' + \frac{32\pi G}{(d-1)c^3} r \left( \phi'^2 + \frac{q^2 A_t^2 e^\chi}{\hbar^2 c^2 f^2} \phi^2 \right) = 0 \,, \tag{2.7}$$

$$f' + \left( \frac{d-2}{r} - \frac{\chi'}{2} \right) f - \frac{rd}{L^2} + \frac{16\pi G}{(d-1)c^3} r \left( \frac{e^\chi A_t'^2}{2\mu_0 c^3} + \frac{m^2 c^2}{\hbar^2} \phi^2 \right) = 0 \,. \tag{2.8}$$

Our gravitational background consists of solutions to these equations, which we consider next.

Firstly, we consider the solution with a trivial scalar field profile. This is just the well-known Reissner-Nordström black brane, given by $\phi = \chi = 0$,

$$A_t = \frac{\mu}{q} \left[ 1 - \left( \frac{r_+}{r} \right)^{d-2} \right] \tag{2.9}$$

and

$$f = \frac{r^2}{L^2} - \left(\frac{r_+}{r}\right)^{d-2} \frac{r_+^2}{L^2} + \frac{8\pi G}{\mu_0 c^6} \frac{d-2}{d-1} \left(\frac{\mu}{q}\right)^2 \left[ \left(\frac{r_+}{r}\right)^{2(d-2)} - \left(\frac{r_+}{r}\right)^{d-2} \right]. \quad (2.10)$$

This solution exists for any temperature $T$. We have written the solution such that the integration constant $\mu$ has indeed the dimension of energy, consistent with its interpretation as a chemical potential in the dual field theory. A peculiar feature of this solution is that the event horizon and hence the entropy remain nonzero when $T = 0$, making this a very unstable phase at low temperatures.

The other solution we consider has a nontrivial scalar field. From the equations of motion, we can derive that as $r \to \infty$, this scalar field behaves as

$$\phi = \phi_s \left(\frac{r}{L}\right)^{-\Delta_-} + \phi_v \left(\frac{r}{L}\right)^{-\Delta_+} + \dots \quad (2.11)$$

with $\Delta_\pm = d/2 \pm \nu \equiv d/2 \pm \sqrt{d^2 + 4\,(mcL/\hbar)^2}/2$. The particular solutions for which the source $\phi_s = 0$ are holographic superconductor solutions in so-called standard quantization.[2] Upon imposing the boundary conditions that we discuss in the next subsection, we can numerically find multiple of such solutions which can be characterized by the number of zeros of $\phi$. These hairy black branes only exist below a certain critical temperature $T_c$, which is proportional to $\mu$ and depends on $d$, $m^2$, and $q$. Keeping $\mu$ fixed, we have checked that the solutions where the scalar field has no nodes have the highest critical temperature. In Fig. 2.1 three solutions for $\phi$ with a different number of nodes are plotted just below their critical temperature.

Note that the parameter $m^2$ is constrained by the Breitenlohner-Freedman bound to $(mcL/\hbar)^2 > -d^2/4$, so that the coefficients $\Delta_\pm$ are always real. Moreover, we will restrict ourselves to $(mcL/\hbar)^2 \leq -d^2/4 + 1$. By doing so, we can compare our results in the following section to results where alternative quantization is used. Within this range for $m^2$, hairy black brane solutions should exist for any $q$ [55]. However, finding solutions for $q < 1$ turned out to be very difficult numerically.

Choosing the solutions with the lowest thermodynamic potential for a fixed $\mu$, i.e., using the grand-canonical ensemble, our gravitational background is

[2] In alternative quantization, $\phi_v = 0$ is used instead. This is only possible when the term with $\phi_s$ in eq. (5.30) has a normalizable fall-off.

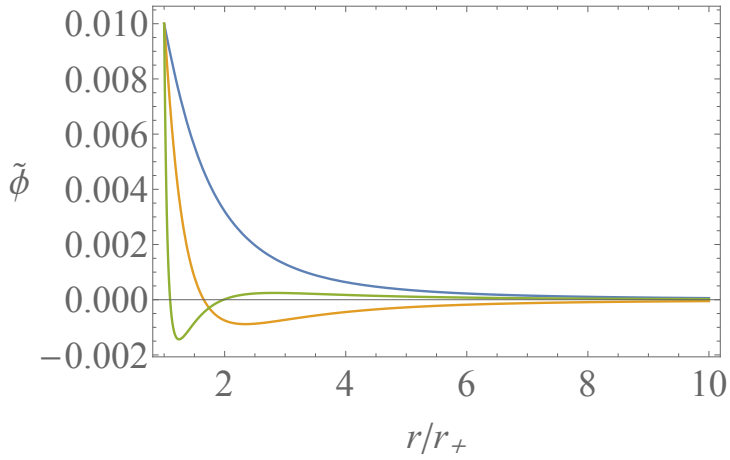


Figure 2.1: The scalar field profile for three different solutions of the equations of motion with $\tilde{q} = 3$ and $\tilde{m}^2 = -3.5$. Here we already use the dimensionless quantities $\tilde{\phi}$, $\tilde{q}$, and $\tilde{m}^2$ defined in eq. (2.12). For each solution the temperature is fixed slightly below the critical temperature, so that $\tilde{\phi}$ remains small. The solution with zero nodes has the highest critical temperature, namely $k_B T_{c0}/\mu \approx 0.075$. The solution with one node has $T_{c1} \approx 0.22 T_{c0}$ and the one with two nodes $T_{c2} \approx 0.031 T_{c0}$.

given by the Reissner-Nordström solution for temperatures above $T_c$. Below $T_c$, the hairy black brane where the scalar field has no zeros is thermodynamically favorable [53]. We can show that for $T = 0$, the event horizon of this hairy black brane vanishes [55], so that we no longer suffer from the abovementioned instability of the Reissner-Nordström solution.

### 2.2.2 Free parameters and boundary conditions

An important property of the solutions is the number of parameters we can tune. Hence we proceed by listing the boundary conditions imposed on the solutions. First of all, we introduce the following dimensionless fields and

coordinates:

$$\begin{cases} (\tilde{t}, \tilde{\mathbf{x}}, \tilde{r}) = (ct, \mathbf{x}, r)/L \\ \tilde{m} = \frac{cL}{\hbar} m \\ \tilde{A}_{\tilde{t}} = \sqrt{\frac{16\pi G}{\mu_0 c^6}} A_t \\ \tilde{\phi} = \sqrt{\frac{16\pi G}{c^3}} \phi \\ \tilde{q} = \sqrt{\frac{\mu_0 c^6}{16\pi G}} \frac{L}{\hbar c} q. \end{cases} \tag{2.12}$$

Notice that this eliminates $G$, $\mu_0$, and $L$ from the equations of motion. In the remainder of this paper we will only use dimensionless units derived from the ones above, while omitting the tildes on the quantities. This implies that energy scales, such as $qA_t$, $\mu$, and $k_B T$, are measured in units of $\hbar c/L$, whereas all length scales are measured in units of $L$. The results can easily be converted back to SI units using eq. (2.12).

Upon introducing the dimensionless quantities from eq. (2.12) in the action in eq. (3.1), we obtain that

$$S/\hbar = \frac{c^3 L^{d-1}}{16\pi G \hbar} \tilde{S} \equiv N_G \tilde{S}, \tag{2.13}$$

where $\tilde{S}$ is the dimensionless action that no longer explicitly contains the quantities $G$, $\mu_0$, and $L$. Hence, the action is proportional to the dimensionless constant $N_G$, which is related to the integer $N$ of the large-$N$ limit of the dual field theory. The dimensionless quantities in eq. (2.12) are defined exactly such that they do not depend on $N$. However, some SI quantities in the action necessarily contain a dependence on $N$, and therefore on $G$, as we will see later on.

Given a dimension $d$, the remaining parameters that determine the bulk geometry are $m^2$ and $q$. Furthermore, as the equations of motion are of first order for $\chi$ and $f$ and of second order for $A_t$ and $\phi$, we need six initial conditions for a particular solution. Finally, we have the position of the event horizon $r_+$, at which we will impose the initial conditions.

Two conditions at the event horizon are given by $A_t(r_+) = 0$ and $f(r_+) = 0$. Furthermore, multiplying eq. (2.5) by $f$ and evaluating at $r_+$ yields the constraint

$$f'(r_+)\phi'(r_+) = m^2 \phi(r_+), \tag{2.14}$$

leaving three initial conditions. Requiring the solution to be asymptotically AdS implies requiring that $\chi(\infty) = 0$. This condition can be incorporated

by first using the initial condition $\chi(r_+) = 0$ and afterwards rescaling the solution using the symmetry

$$e^{\chi} \to C^2 e^{\chi}, \qquad t \to Ct, \qquad A_t \to A_t/C, \tag{2.15}$$

with $C = e^{-\chi(\infty)/2}$, which leaves the equations of motion invariant. Finally, we fix another initial condition by requiring $\phi_s = 0$ in eq. (5.30), corresponding to an unsourced vacuum expectation value. We are thus left with only one initial condition that is unspecified.

Using another symmetry of the equations of motion given by

$$r \to ar, \quad (t, \mathbf{x}) \to (t, \mathbf{x})/a, \quad f \to a^2 f, \quad A_t \to a A_t, \tag{2.16}$$

we can obtain any solution from a solution with $r_+ = 1$. Thus we see that our bulk solution can only nontrivially depend on $d$, $m^2$, $q$ and, due to the unspecified initial condition, on one additional parameter which we take to be $k_B T/\mu$.

Naturally, the geometry of the Reissner-Nordström black brane does not depend on the parameters $m^2$ and $q$. The dependence on these parameters becomes visible only after including scalar fluctuations to this background.

### 2.2.3 The phase transition and Ginzburg-Landau theory

To describe the theory on the boundary, we concentrate on the case $d = 4$, such that the boundary has three spatial dimensions. After having solved the equations of motion, we can extract boundary values corresponding to physical quantities from the solution. From the scalar field expansion eq. (5.30), we obtain the order parameter $\langle O \rangle = 2\nu\phi_v$ which is sourced by $\phi_s$, see e.g. Ref. [56]. Similarly, we can expand the gauge field near the boundary as

$$A_t = \frac{\mu}{q} - \frac{nq}{2} r^{-2} + \dots . \tag{2.17}$$

Here we have written the integration constants in such a way that $\mu$ corresponds to the dimensionless chemical potential, measured in units of $\hbar c/L$. The quantity $n$ corresponds to a dimensionless number density in the dual field theory. Finally, given a bulk solution, we obtain the temperature of the dual field theory from the Hawking temperature in eq. (3.3).

From the discussion in the previous subsection it follows that for a given $q$ and $m^2$ physical quantities can depend on $k_B T/\mu$, but may also contain a dependence on $N_G$. This dependence follows directly from the proportionality of the bulk action to $N_G$ in eq. (2.13). Additionally, we may wonder about the physical meaning of the bulk parameters. The mass $m$ determines the scaling dimension of the order parameter $\langle O \rangle$, as follows from the expansion in eq. (5.30). The charge $q$ also defines a property of the field theory. In particular, it is related to the structure constants that appear in the three-point functions [49]. Note that the dimensionless charge $q$ does not give the charge of the operator $\langle O \rangle$, which can most easily be seen from its definition in eq. (2.12). As we have no numerical value of the AdS radius $L$ and the constants $\mu_0$ and $G$ in $d = 4$ dimensions, the proportionality factor between the charge in SI units and its dimensionless counterpart remains unknown. Thus, even if we consider $\langle O \rangle$ as an expectation value related to Cooper pairs, so that we know there are two particles involved, we do not know the value of $q$. Finally, we have the parameter $N_G$, which is proportional to the integer $N$ of the large-$N$ limit. Hence in this limit we still have a finite parameter $N/N_G$.

As the source term in the background is put to zero by construction, the dual theory acquires an unsourced expectation value below $T_c$. This corresponds to an order parameter of a phase transition which spontaneously breaks the $U(1)$ symmetry. In Fig. 2.2 the order parameter is shown as a function of the ratio $k_B T/\mu$ for various values of $q$ and $m^2$. We can deduce from this that the phase transition is always of second order. Therefore, we can describe the order parameter $\langle O \rangle$ with a Ginzburg-Landau model. More specifically, such a model can be represented by the action

$$S = -\int \mathrm{d}t \int \mathrm{d}^3\mathbf{x} \left( \alpha |O|^2 + \frac{\beta}{2} |O|^4 \right), \tag{2.18}$$

where $\alpha$ and $\beta$ are temperature-dependent real coefficients. For $\beta > 0$, there appears a nontrivial global minimum

$$\langle O \rangle = \sqrt{-\frac{\alpha}{\beta}}, \tag{2.19}$$

when $\alpha$ becomes negative below the transition temperature. Note that we have chosen the expectation value of $O$ to be real here, which corresponds to

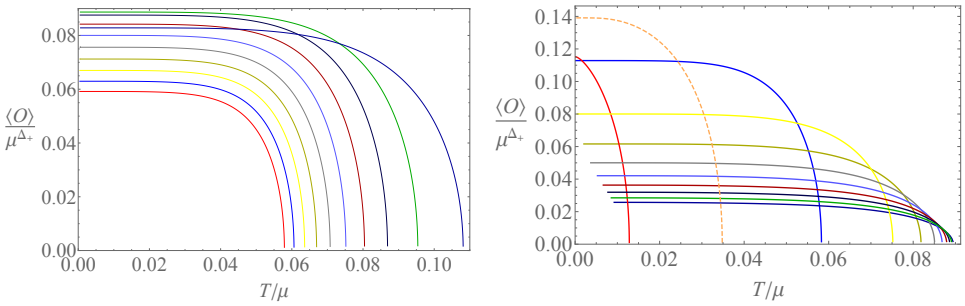


(a) $q = 3$ (b) $m^2 = -3.5$

Figure 2.2: The expectation value of the order parameter as a function of the temperature. In (a), $q$ is fixed and $m^2$ decreases from $m^2 = -3$ for the curve with the lowest critical value of $T/\mu$ to $m^2 = -3.9$ for the curve with the highest critical value of $T/\mu$, with steps $\Delta m^2 = -0.1$. In (b), $m^2$ is fixed and $q$ increases from $q = 1$ for the curve with the lowest critical value of $T/\mu$ to $q = 10$ for the curve with the highest critical value of $T/\mu$. We plotted integer values of $q$ here. The exception is the dashed orange curve for $q = 1.4$, which was added to show that the dependence on $q$ of the expectation value of the order parameter at zero temperature is not monotonic.

the gauge choice of a real $\phi$ in the bulk theory. Moreover, the numerical data yields that $\langle O \rangle \propto |T - T_c|^{1/2}$ near $T_c$. This suggests the conventional choice $\alpha(T) \approx \alpha_0(T - T_c)$ and $\beta = \beta_0 \neq 0$ for the coefficients near $T_c$, as from this we indeed obtain the well-known mean-field result $\langle O \rangle \propto |T - T_c|^{1/2}$ in the superconducting phase. The temperature dependence of $\alpha$ and $\beta$ is confirmed by the calculations performed below. However, it is in this bottom-up case not possible to extract such a temperature dependence from a microscopic theory, since as mentioned in the introduction, the microscopic origin of the order parameter is not known. It may however be possible to formulate a microscopic theory using a top-down approach, where one starts with the full duality between type IIB string theory and super Yang-Mills theory, and performs consistent truncations to arrive at the desired model.
Although the above Ginzburg-Landau model can be applied for all the cases shown in Fig. 2.2 , the parameters in the model can be seen to depend on $q$ and $m^2$. For example, the value of the order parameter at zero temperature has a nontrivial dependence on both $m^2$ and $q$. The figure shows that this

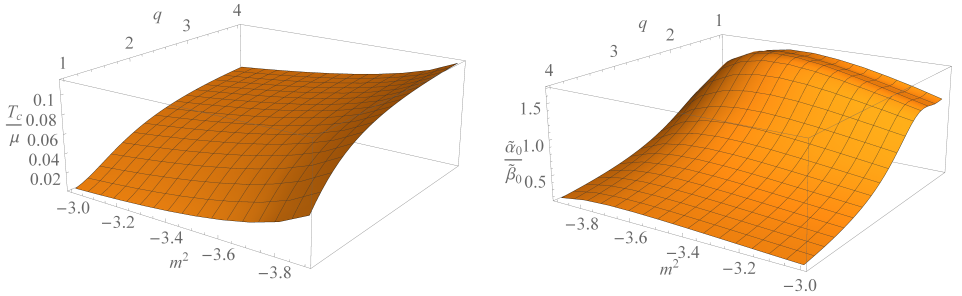


(a) Critical temperature (b) $\alpha_0/\beta_0$

Figure 2.3: (a) The critical temperature as a function of the parameters $q$ and $m^2$. (b) The proportionality constant between the order parameter and $|T - T_c|^{1/2}$ near the critical temperature as a function of $q$ and $m^2$. The tildes above the parameters imply that they are scaled with appropriate powers of $\mu$ to make their scaling dimension zero.

dependence is not monotonic. In general, the critical temperature increases upon increasing $q$ or $|m^2|$, as shown in Fig. 2.3a.[3] The coefficients $\alpha$ and $\beta$ also depend on $q$ and $m^2$. In Fig. 2.3b we have shown this dependence for the coefficient $\alpha_0/\beta_0$, which is the square of the proportionality constant between $\langle O \rangle$ and $|T - T_c|^{1/2}$ near the transition temperature. Scaling the temperature by $T_c$ and the order parameter by its value at $T = 0$, we obtain from Fig. 2.2 the plots in Fig. 2.4 . We see that the rescaled curves show very little dependence on $m^2$ and $q$, except for lower values of $q$. The black curve corresponds to BCS theory. This is a universal result, i.e., this curve is common to all BCS superconductors. Hence, deviations from this curve are a result of strong-coupling effects.

In BCS theory, the order parameter corresponds to the energy gap $\Delta$ of the fermionic single-particle excitation spectrum. The quantity $\langle O \rangle$ does not in general have the (scaling) dimension of energy. Nevertheless, since both $\Delta$ and $\langle O \rangle$ show mean-field behavior near the transition temperature, $\langle O \rangle$ could be proportional to the gap. The proportionality constant can still depend on $q$ and $m^2$ in a nontrivial way. This proportionality constant should cancel in Fig. 2.4 , i.e., $\langle O \rangle \,/\, \langle O \rangle_{T=0} = \langle \Delta \rangle \,/\, \langle \Delta \rangle_{T=0}$. We have therefore attempted to

[3] We have checked that in alternative quantization, the critical temperature increases upon *decreasing* $|m^2|$.

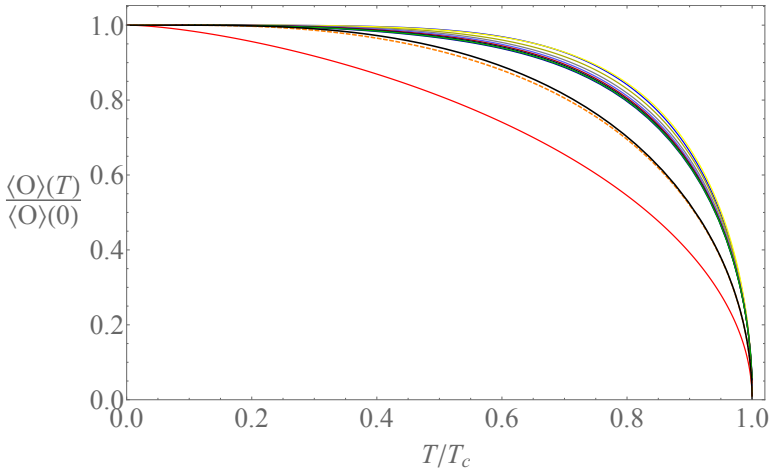


Figure 2.4: The scaled order parameter $\langle O\rangle / \langle O\rangle_{T=0}$ as a function of $T/T_c$ for different values of $q$ and $m^2$. We have used all values of $q$ and $m^2$ which are plotted in Fig. 2.2 as well. The black curve is the result from BCS theory. Apart from the red curve and dashed orange curve, corresponding to $q = 1$ and $q = 1.4$ respectively and $m^2 = -3.5$, the dependence on $q$ and $m^2$ seems small. The other curves have $q \geq 2$.

extract this proportionality constant from this figure in a different manner, using the fact that at small temperatures we have the behavior [57]

$$\frac{\langle\Delta\rangle(T)}{\langle\Delta\rangle(0)} - 1 \propto \exp\big[-\langle\Delta\rangle(0)/T\big]. \tag{2.20}$$

However, as we approached zero temperature, our numerical data became too inaccurate to reliably obtain the gap from this expression.
Finally, we have shown in Fig. 2.5a the dependence of the zero-temperature (dimensionless) number density $n(0)$ on the parameters $q$ and $m^2$. This number density is determined from the bulk solution using eq. (2.17). Notice that for a given $q$ and $m^2$, the ratio $n(0)/\mu^3$ is fixed. In contrast, since the action is proportional to $N_G$ as defined in eq. (2.13), the total density in SI units contains an additional factor of $N_G$ with respect to its dimensionless counterpart. The exact relation is

$$n = N_G \tilde{n} L^{-3}, \tag{2.21}$$

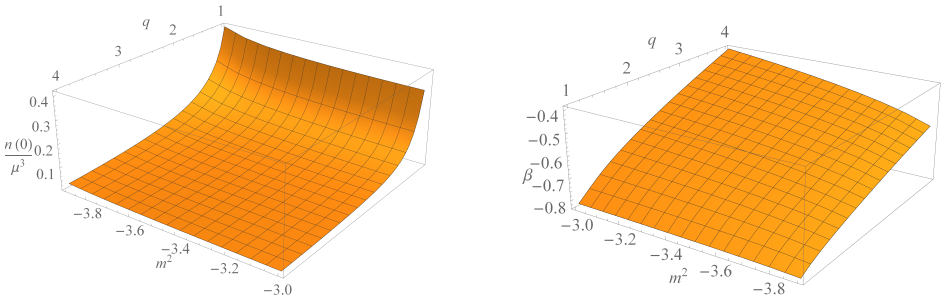


(a) (b)

Figure 2.5: (a) The total number density of the holographic superconductor at zero temperature. (b) The parameter $\beta \equiv -1 + \mu/\epsilon_F$ as a function of $q$ and $m^2$. Here we have taken $N/N_G = 1$.

where we temporarily restored the tilde to distinguish the dimensionless density $\tilde{n}$ from the dimensionful one $n$. It follows that the total density diverges in the large-$N$ limit. However, we are interested in the density of one species, i.e., the total density divided by the number of species $N$. This density coincides with the density numerically obtained from eq. (2.17) up to the factor $N_G/N$, which remains an unknown parameter, but should in principle be fixed by a top-down approach.

The fixed value of $n(0)/\mu^3$ is reminiscent of an ultracold fermion gas near a Feshbach resonance [58]. In such an ultracold gas, there are two independent length scales at zero temperature. One of these is the $s$-wave scattering length $a$, which controls the strength of the interaction between the fermions within a Cooper pair. The other length scale is the inverse Fermi wavelength $k_F^{-1}$, which at zero temperature is related to the number density by $n = k_F^3/(3\pi^2)$ for a single fermion species with two spin components. All dimensionless thermodynamic quantities can then be expressed as a function of the dimensionless quantity $1/k_F a$. In the weakly coupled BCS limit there are small attractive interactions, so that $1/k_F a$ becomes very negative, whereas in the BEC limit $1/k_F a$ is positive and the Cooper pairs form two-body bound states. In the strongly coupled regime $1/k_F|a| < 1$ there is a smooth crossover between the BEC and BCS regime, which is appropriately called the BEC-BCS crossover. In the unitarity limit, $1/k_F a = 0$ as $a$ diverges, such that the thermodynamics can only depend on $k_F$. Similar to the

situation in our dual field theory, dimensionless quantities like $\mu/\epsilon_F \equiv 1+\beta$, with $\epsilon_F$ the Fermi energy, then become universal constants. This is one of the claims of the so-called universality hypothesis [30].

The function $\beta(k_F a)$, not to be confused with the parameter $\beta$ in the Ginzburg-Landau action in eq. (2.18), can be determined from experiments. For an ideal gas at zero temperature one has $\mu = \epsilon_F$, so that $\beta = 0$. In the weakly coupled BCS limit one has small attractive interactions, so that $\beta$ becomes a small negative number. For an ultracold Fermi gas at unitarity, the variational BCS wave function yields that $\beta = -0.4$ [9], whereas Monte-Carlo simulations show that $\beta \approx -0.6$ [45] and experiments have yielded $\beta = -0.7 \pm 0.1$ [59]. Naturally the strong coupling yields a deviation from the BCS theory result. In Fig. 2.5b , we have plotted the constant $\beta$ for the holographic superconductor. To obtain this figure, we assume that the bosonic order parameter comes from a pair of fermions[4] with Fermi velocity $c$, such that $\epsilon_F = \hbar c k_F$. This is because $\epsilon_F$ is defined with respect to the reference system dual to AdS spacetime without hair, which yields a relativistic field theory where the Dirac cones are just given by $\omega = \pm c|\mathbf{k}|$. Moreover, we have fixed the number of species to $N = N_G$. For the values of $q$ and $m^2$ shown, we see that the result obtained in Fig. 2.5b has the right order of magnitude for a superfluid in the BEC-BCS crossover regime.

The question now arises how high the critical temperature of the strongly coupled superconductor in the dual field theory actually is. As we have already noticed from Fig. 2.3a , the critical temperature is highest when $m^2$ is close to the BF-bound and $q$ is large. As shown in Fig. 2.6a , the critical ratio of $T$ and $\mu$ saturates for large $q$ to $T_c/\mu \approx 0.16 \approx 1/2\pi$. These values are comparable to the regime of unitary Fermi gases. If we rescale $T_c$ by the Fermi energy instead, using the same value for $N_G/N$ as before, we obtain Fig. 2.6b . We obtain that $T_c/\epsilon_F \propto q^{2/3}$ for large values of $q$. Due to this dependence on $q$ and $N_G/N$, we cannot unambiguously compare the value of $T_c/\epsilon_F$ to other results, obtained for example by experiments or quantum Monte-Carlo simulations. Finally we note that in alternative quantization, the critical temperature is the highest when $m^2$ is close to the upper bound $m^2 = -3$. Then the ratio $T_c/\mu$ saturates to about 1.7, which is more than ten times larger than in normal quantization.

[4] This means that $N$ corresponds to the number of *fermionic* species in our theory. See [1] for further details on this.

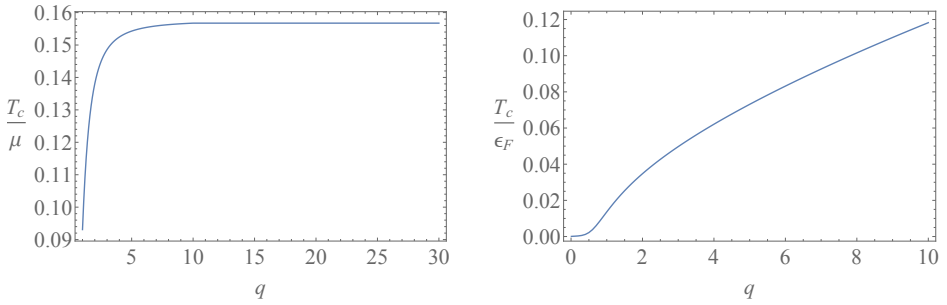


(a) $T_c/\mu$ (b) $T_c/\epsilon_F$

Figure 2.6: The critical temperature scaled by (a) the chemical potential and (b) the Fermi energy respectively. In both figures, $m^2 = -3.9999$. In (b), we used $N/N_G = 1$.

## 2.3 Order parameter fluctuations

In the previous section, we have specified which gravitational background and corresponding dual field theory we use. In this section, we study the scalar field fluctuations on top of this background. From these we subsequently determine the two-point function corresponding to the order parameter dynamics in the normal phase of the dual field theory and describe this with a time-dependent Ginzburg-Landau model.

### 2.3.1 Calculating two-point functions

When given an action for the bulk theory, there is a well-known procedure for calculating the corresponding retarded Green's function of the boundary. This gives information about the dynamics of the system, e.g., the quasinormal modes coincide with the poles of the retarded Green's function [60]. Let us first sketch how to find this retarded Green's function. A more extensive explanation of this approach can be found e.g. in Ref. [61]. Consider a bulk action that depends on the fields $\Phi^I$. Here, the index $I$ labels the different fields in the theory, which are in our case the scalar field $\phi$, the gauge field $A_\mu$, and the metric $g_{\mu\nu}$. To obtain the Green's function, we expand the action up to second order in the fluctuations $\delta\Phi^I$ of the bulk fields around their

expectation values $\langle \Phi^I \rangle$. The result can be written in the form

$$S^{(2)} = -\frac{1}{2}\int \mathrm{d}^{d+1}x\, \delta\Phi^\dagger \mathbf{G}_B^{-1}\delta\Phi + S_\partial^{(2)}, \tag{2.22}$$

where $S_\partial^{(2)}$ is a boundary action and $\mathbf{G}_B^{-1}$ is a linear operator acting on $\delta\Phi$. This defines the linearized equations of motion in the bulk as

$$\mathbf{G}_B^{-1}\delta\Phi = 0. \tag{2.23}$$

Because the matrix $\mathbf{G}_B^{-1}$ is in general not diagonal, this becomes a coupled system of linear ordinary differential equations.

Near the boundary, we can expand the solutions to the linearized equations of motion as

$$\delta\Phi^I = \delta\Phi_s^I r^{-\Delta_-^I} + \delta\Phi_v^I r^{-\Delta_+^I} + \dots . \tag{2.24}$$

Here, the values of the exponents $\Delta_\pm^I$ depend on which field is considered. For example, for the scalar field the exponents are given in eq. (5.30). Furthermore, the coefficients $\delta\Phi_v^I$ correspond to fluctuations in the expectation values of the operators in the dual field theory. The $\delta\Phi_s^I$ are the source fluctuations. In general, the fluctuation of a single source will lead to fluctuations in the expectation value of all operators. This is a direct consequence of the fact that the linearized equations of motion in eq. (2.23) are coupled. Writing the fluctuations in Fourier space as

$$\delta\Phi^I(r,\mathbf{x},t) = \int \frac{\mathrm{d}^d k}{(2\pi)^d}\delta\Phi^I(r,k)e^{ik_a x^a}, \tag{2.25}$$

with the dimensionless four-momentum $k_a = (-\omega, \mathbf{k})$,[5] we can write the boundary action $S_\partial^{(2)}$ in the form

$$S_\partial^{(2)} = \frac{1}{2}\frac{1}{(2\pi)^d}\int \mathrm{d}\omega \int \mathrm{d}^{d-1}\mathbf{k}\, \delta\Phi_s^\dagger \mathbf{G}_R \delta\Phi_s. \tag{2.26}$$

The matrix $\mathbf{G}_R(\omega,\mathbf{k})$ is the retarded Green's function of the boundary theory in Fourier space. It describes the dependencies of the fluctuations of the expectation values $\delta\Phi_v$ on the fluctuations of the sources $\delta\Phi_s$. These are

[5] The frequency and the wavevector are made dimensionless in the way consistent with eq. (2.12) i.e., $\tilde{\omega} = \omega L/c$ and $\tilde{\mathbf{k}} = \mathbf{k}L$.

in turn found from the solutions to the linearized equations of motion in eq. (2.23), using infalling boundary conditions at the horizon in order to get the *retarded* Green's function [60].

Now, suppose that we wish to study the full dynamics of the order parameter fluctuations by computing the correlator $\langle O'^* O' \rangle$, which is proportional to one of the components of the matrix $\mathbf{G}_R$ in eq. (2.26). By computing the on-shell action we obtain

$$S_\partial^{(2)} = \frac{1}{2}\frac{1}{(2\pi)^d}\int \mathrm{d}\omega \int \mathrm{d}^{d-1}\mathbf{k}[2\nu\left(\delta\phi_s^*\delta\phi_v + \text{h.c.}\right)] + \dots\,, \tag{2.27}$$

where we remind the reader that $\nu \equiv \sqrt{d^2 + 4\left(mcL/\hbar\right)^2}/2$, see after eq. (5.30). The bulk action does not contribute, as it vanishes due to the linearized equations of motion in eq. (2.23). The terms represented by the dots are associated with contributions from the other fields, but cannot yield any terms proportional to $\delta\phi_s^*\delta\phi_s$. Moreover, the hermitian conjugate (h.c.) terms contribute to the correlator $\langle O' O'^* \rangle$. From the expression above it follows that

$$i\langle O'^* O' \rangle = 2\nu \left(\frac{\partial \delta\phi_v}{\partial \delta\phi_s}\right)_{\delta\Phi_s^{I\neq\phi}}. \tag{2.28}$$

This expression denotes the variation of $\delta\phi_v$ with respect to $\delta\phi_s$, where the other sources are kept constant under this variation. We can calculate this as follows. Since in general the order parameter fluctuations are influenced by variations of all the sources in the theory, we can write the scalar field fluctuations near the boundary as

$$\begin{aligned}\delta\phi &= \delta\phi_s r^{-\Delta_-} + \delta\phi_v r^{-\Delta_+} + \dots \\ &= \delta\phi_s r^{-\Delta_-} + a_I \delta\Phi_s^I r^{-\Delta_+} + \dots\,,\end{aligned} \tag{2.29}$$

where the sum over $I$ is over all the field fluctuations and where $a_I$ are frequency and momentum dependent functions. In this case, from eq. (2.28) we would have $i\langle O'^* O' \rangle = 2\nu a_\phi$. Now assume that we have obtained a numerical solution to the linearized equations of motion eq. (2.23), which is a formidable task in practice. Then we would be able to read off the coefficients $\delta\phi_v$ and $\delta\phi_s$. Since $\delta\phi_v$ in general includes contributions from sources other than $\delta\phi_s$, we cannot find $\langle O'^* O' \rangle$ from simply taking the ratio of these coefficients. However, exploiting the linearity of eq. (2.23) enables

us to find a solution which on the boundary only sources the scalar field fluctuations. We then have that all source fluctuations $\delta\Phi_s^I$ vanish except for $\delta\phi_s$, so that $\delta\phi_v = a_\phi \delta\phi_s$ in eq. (2.29). As a consequence, for this particular solution the correlator $\langle O'^* O' \rangle$ can be found from the ratio of $\delta\phi_v$ and $\delta\phi_s$. [6]

Above the critical temperature, the fluctuations of the order parameter are decoupled from the other hydrodynamic fluctuations in the theory. In the bulk theory, we can then find a solution to the linearized equations of motion by simply setting $\delta A_\mu$ and $\delta g_{\mu\nu}$ to zero. As a consequence, we can then find the retarded Green's function of the order parameter by solving

$$\left(D_\mu D^\mu - m^2\right)\delta\phi = 0. \tag{2.30}$$

This equation is found from the linearized equations of motion in eq. (2.23) by just putting the other fluctuations to zero. Basically, this corresponds to the bulk-to-boundary propagator shown in Fig. 2.7. Here, the scalar field fluctuations propagate into the bulk without coupling to the other fluctuations that are present there. In Fourier space, eq. (2.30) for the order parameter fluctuations can be written as

$$\delta\phi'' + \left(\frac{f'}{f} + \frac{d-1}{r} - \frac{\chi'}{2}\right)\delta\phi' - \frac{m^2 - (qA_t+\omega)^2\frac{e^\chi}{f} + \frac{|\mathbf{k}|^2}{r^2}}{f}\delta\phi = 0. \tag{2.31}$$

The conjugate equation holds for $\delta\phi^*$. Notice that this implies that $\delta\phi^*$ is not coupled to $\delta\phi$. This implies that $\partial\delta\phi_v/\partial\delta\phi_s^* = 0$. As a consequence, we can always calculate the Green's function by first numerically solving eq. (2.31) and then computing the ratio of the resulting coefficients $\delta\phi_v$ and $\delta\phi_s$. As usual, we require infalling boundary conditions at the horizon, corresponding to the *retarded* Green's function. Naturally, besides depending on frequency and momentum, this two-point function depends on the background parameters, i.e., on $q$, $m^2$ and $T/\mu$.

### 2.3.2 Green's function in the normal phase

To obtain the retarded Green's function in the normal phase, we must solve eq. (2.31) with $\chi = 0$, and with $A_t$ and $f$ given by eqs. (2.9) and (2.10)

[6] With this particular solution, we can also find other correlators that follow from expressions like $\frac{\delta A_{\mu,v}}{\delta\phi_s}$. In fact, with this solution we can find exactly one column of the retarded Green's function matrix.

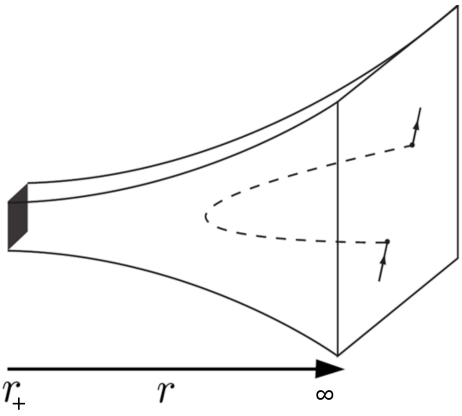


Figure 2.7: (a) Illustration of the bulk-to-boundary propagator. The dashed curve denotes the scalar field fluctuations propagating into the bulk geometry. This figure is an adapted version of Fig. 2 in [62].

respectively. We have done so numerically. Using the numerical solution, we obtain the retarded Green's function by using Eqs. (2.29) and computing the ratio of $\delta\phi_v$ and $\delta\phi_s$, because in the normal phase the fluctuations are decoupled.

Approaching the transition temperature from above, the physics can be described with a time-dependent Ginzburg-Landau model. This can be represented by the action

$$S = -\int \mathrm{d}t \int \mathrm{d}^3\mathbf{x} \left( iaO^*\partial_t O + \gamma|\nabla O|^2 + \alpha|O|^2 + \frac{\beta}{2}|O|^4 \right), \tag{2.32}$$

which incorporates the result of eq. (2.19). The first two terms of the integrand capture the long-wavelength and low-frequency behavior of the order parameter. Like $\alpha$ and $\beta$, the coefficients $\gamma$ and $a$ depend on the temperature. The coefficient $a$ is complex, since the system shows dissipation of the order parameter. This implies that the imaginary part of $a$ is negative. Physically, dissipation occurs as a consequence of temperature fluctuations, which can cause the fermion pairs to break up. From the above action, we obtain the retarded Green's function of $O$ in this model from the part of the action that is quadratic in the order parameter fluctuations, which we can subsequently compare with the retarded Green's function obtained holographically. Thus,

this is a tree-level calculation, even though AdS/CFT should provide us with the *full* partition function of the dual field theory. The reason is that contributions of higher orders in the fluctuations are suppressed by the large-$N$ limit, implicit in the AdS/CFT correspondence, and loop diagrams come with factors of $1/N$. This claim is motivated by the mean-field result for the critical exponent in Fig. 2.2 , which does not change when taking into account only Gaussian fluctuations.

Since the order parameter has a vanishing expectation value in the normal phase, the part of the Ginzburg-Landau action that is quadratic in the order parameter fluctuations $O' \equiv O - \langle O \rangle = O$ is given by

$$S_{\text{quad}} = \frac{-1}{(2\pi)^4} \int \mathrm{d}\omega \int \mathrm{d}^3\mathbf{k} O'^*(\omega, \mathbf{k})[a\omega + \gamma|\mathbf{k}|^2 + \alpha_0(T - T_c)]O'(\omega, \mathbf{k}) \quad (2.33)$$

near the transition temperature $T_c$. From this we obtain that the two-point function is given by

$$G_{R,O}(\omega, \mathbf{k}) = \frac{1}{a\omega + \gamma|\mathbf{k}|^2 + \alpha_0(T - T_c)}. \quad (2.34)$$

This result should hold for small frequencies and momenta, i.e., $\omega \ll \mu$ and $|\mathbf{k}| \ll \mu$, since the Ginzburg-Landau action in eq. (2.32) only contains the leading orders of the gradient expansion. Comparing the above expression to our numerical results, we can determine the coefficients $\alpha_0$, $a$, and $\gamma$ near $T_c$. The result is shown in Fig. 2.8 . Together with the result from Fig. 2.3b in the previous section, we then obtain all the coefficients in eq. (2.32) near the critical temperature. Although quantitatively, the results clearly depend on $m^2$ and $q$, the qualitative physics does not seem very different for different values of these parameters. Therefore we will restrict the following discussion of the retarded Green's function to the fixed values $q = 3$ and $m^2 = -3.5$.

From the retarded Green's function $G_{R,O}$, we can obtain the spectral function

$$\rho(\omega, \mathbf{k}) = \frac{1}{\pi} \operatorname{Im} G_{R,O}(\omega, \mathbf{k}). \quad (2.35)$$

This is an interesting quantity, as it yields the dispersion relations of the modes accessible to the order parameter dynamics as well as the corresponding lifetimes. In Fig. 2.9 this quantity is shown at the temperature $T = 1.5T_c$. Here we have plotted the absolute value of the spectral function, noting that the spectral function itself is negative for $\omega < 0$. Moreover, we have exploited

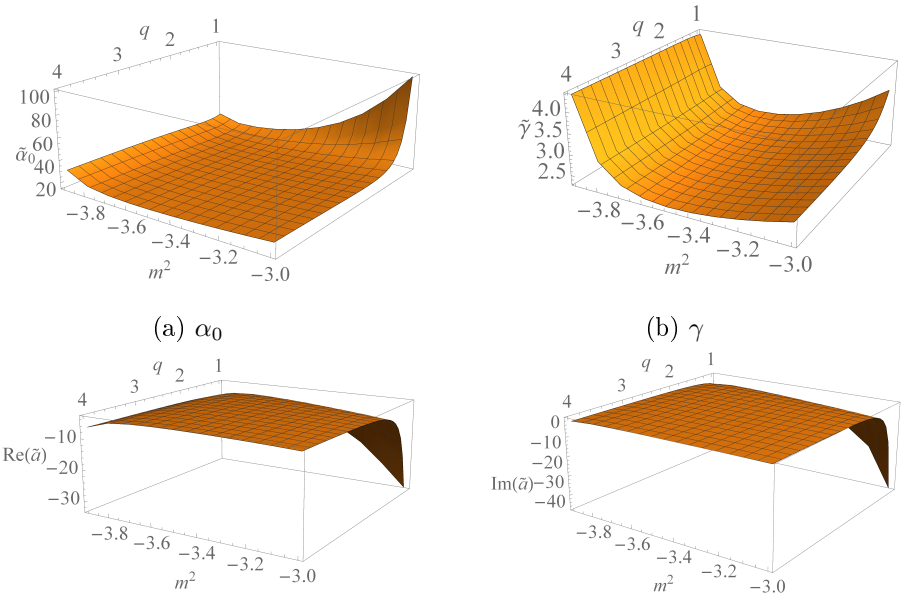


(a) $\alpha_0$ (b) $\gamma$

(c) Re($a$) (d) Im($a$)

Figure 2.8: The parameters in the Ginzburg-Landau action as a function of $q$ and $m^2$. The parameter $\beta$ follows from Fig. 2.3b . The tildes above the parameters imply that they are scaled with appropriate powers of $\mu$ to make them dimensionless.

rotational invariance to fix the direction of $\mathbf{k}$, such that $k$ denotes the component in that direction. Naturally the spectral function is symmetric in $k$. In accordance with the Green's function in eq. (2.34) obtained in the Ginzburg-Landau model, we see that the spectral function vanishes for $\omega = 0$, since $\alpha$, $\beta$, and $\gamma$ are real coefficients. Furthermore, for small $\omega$ and $\mathbf{k}$, we also see a quadratic dispersion as predicted by eq. (2.34), which is shifted upward from $\omega = 0$ since $\alpha$ is nonzero. When $\omega$ is large compared to $\mu$ and $T_c$, we recover the spectral function from pure AdS, which is given by (see e.g. Ref. [60])

$$\rho_{\text{AdS}}(\omega, \mathbf{k}) = \frac{2\nu}{\pi} \text{Im} \left( \frac{\sqrt{-\omega^2 + |\mathbf{k}|^2}}{2} \right)^{2\nu} \frac{\Gamma(-\nu)}{\Gamma(\nu)}, \tag{2.36}$$

where $\nu = \sqrt{d^2 + 4m^2}/2$ as before and $\Gamma$ denotes the gamma function. In

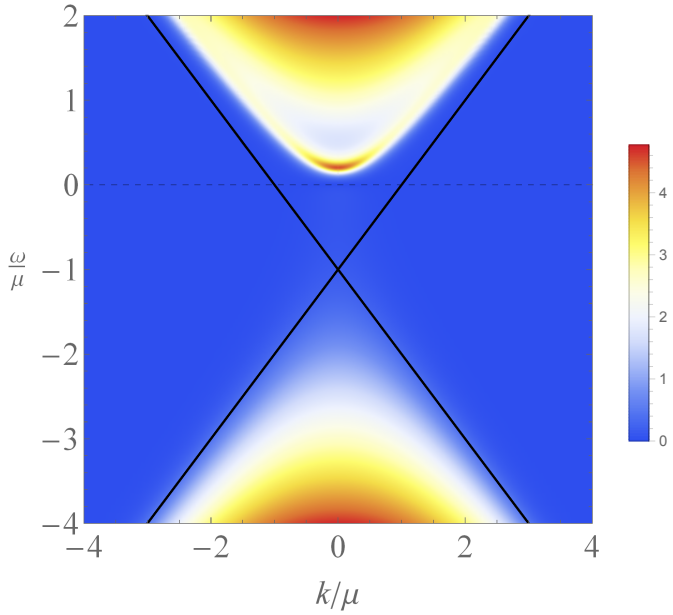


Figure 2.9: The spectral function for $T = 1.5T_c$, $q = 3$, and $m^2 = -3.5$. Here and in all following plots of the spectral functions, we have shown the absolute value of the spectral functions and divided by a factor $\mu^{2\nu}$ to make them dimensionless.

Fig. 2.9 we observe that the spectral weight fills the light cone which is shifted down by the chemical potential, i.e., $|\omega + \mu| = |k|$. This cone is shown in black in the figure, where the momentum space domain is taken small enough such that shift is still visible.

In Fig. 2.10 , the spectral function for $T = T_c$ is shown. As before, we can distinguish two regimes here, namely the UV regime in which we recover the AdS result and the IR regime in which the physics can be described with the Ginzburg-Landau model. In the latter regime we again see the quadratic dispersion predicted by eq. (2.34), which gives a peak centered at $\omega_{\text{peak}} = -\gamma|\mathbf{k}|^2 \text{Re}(a)/|a|^2$ since now $\alpha = 0$ in eq. (2.18).

Notice that in Ref. [54], a similar approach to the retarded Green's function is given for the zero-momentum case. Although the UV results are different because Ref. [54] uses alternative quantization, the IR results are comparable, i.e., in both cases the results can be described in the low-frequency

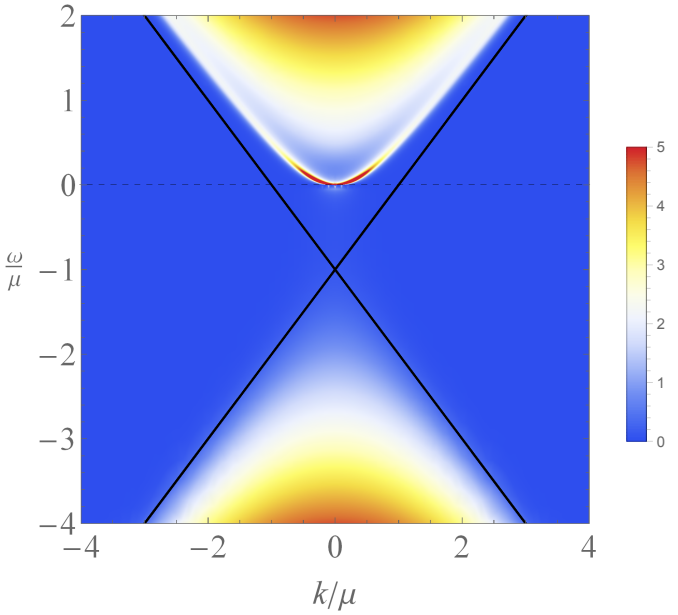


Figure 2.10: The spectral function as $T \to T_c$ for $q = 3$ and $m^2 = -3.5$.

limit with the Ginzburg-Landau model.

## 2.4 Discussion

Determining the full Green's function in the superconducting phase requires a formidable numerical calculation. To this end, we must solve the full system of linearized equations of motion for the fluctuations in the scalar field $\delta\phi$, the gauge field $\delta A_\mu$ and the metric tensor $\delta g_{\mu\nu}$, where this time the bulk geometry is given by the numerical functions $f$, $\chi$, $A_t$ and $\phi$ discussed in the previous section. Fortunately, the remainder of this thesis focusses on single-particle spectral functions that are found by having probe fields propagate on a gravitational bulk theory. Since these probe fields do not backreact on the bulk geometry, including coupling between fluctuations of different bulk fields will not be necessary. As such, we restricted our discussion in this chapter to the normal phase. However, in Ref. [1] we provide for an alternative calculation which gives more insight in the physics of the order

parameter dynamics in the superconducting phase.

# 3 Massive Dirac fermions from holography

## 3.1 Introduction

The holographic principle has established itself as a common instrument for the description of strongly coupled systems. While originally applied to supersymmetric theories such as $\mathcal{N} = 4$ super-Yang-Mills theory [6, 39, 40], it was soon realized that the correspondence could be used to model real-world systems as well, such as quantum chromodynamics and the quark-gluon plasma [63, 64]. In addition, over the past decade holography has been extended to include condensed-matter theory, which has led to the description of many strongly coupled condensed-matter phenomena by means of weakly coupled gravitational theories [50, 56, 65, 66]. These descriptions provide a great tool to compute thermodynamic and hydrodynamic properties, and besides this, also the spectra of bosonic or fermionic operators that are present in the dual condensed-matter field theory.

Condensed-matter systems are usually described by nonrelativistic Dirac fermions. In holography, a common approach to cope with nonrelativistic systems is to use a Lifshitz background, which leads to a dynamical scaling exponent $z$ in the boundary theory that is different from its value in relativistic theories, i.e., $z \neq 1$ [67–70]. Alternatively, an asymptotically anti-de Sitter gravity theory may have an emergent infrared (IR) Lifshitz geometry with a scaling exponent $z$ different from 1, so that the dynamics obtained from such theories can be reminiscent of nonrelativistic physics when restricted to the long-wavelength and low-frequency limit. However, Lifshitz backgrounds generally yield gapless particle-hole symmetric spectra and in both of these approaches, a missing ingredient is a Dirac mass in the spectrum. Such models are therefore great candidates for the description of effectively massless systems, such as single- or bilayer graphene, or the more recently discovered Dirac and Weyl semimetals [56, 62, 71]. For other purposes, it is desirable to extend the holographic model to also be able to describe spectral functions of massive fermionic operators that are ubiquitous in condensed matter. In

this work we study the fermionic spectral functions that are obtained from such an extension.

To see what such an extension entails, it is important to realize that the reason that the fermionic spectra obtained from holography are in general gapless is twofold. Firstly, by introducing a probe Dirac spinor in the gravitational bulk theory, the fermionic spectral function on a boundary theory corresponds to a chiral fermion and is therefore massless [72–76]. Secondly, introducing a mass in the boundary theory requires introducing a new scale in the conformal field theory (CFT), which implies that it is necessary to add a deformation to the bulk. The latter deformation was introduced in Refs. [41, 77], which focused on a model for the conductivity of a topological Weyl semimetal. In this paper, the model used to obtain the fermionic spectral functions includes such a deformation, as well as an additional Dirac spinor in the bulk, yielding the required amount of degrees of freedom on the boundary to describe a Dirac fermion. A model with two Dirac fermions in the bulk has already been used in Ref. [78] to study Dirac semimetals. In this work we additionally introduce a coupling of the two Dirac fermions in the bulk to provide a coupling between the chiral fermions on the boundary, which is necessarily present for massive fermions. A similar construction was very recently described in Ref. [79], which appeared while completing this paper, where the approach was used to study semimetals with nodal lines. We would like to stress that our emphasis here is not on Weyl or nodal-line semimetals, but more generally on the description of fermionic spectra in condensed-matter systems which generally contain a Dirac mass. In these spectra, this mass can for instance be interpreted as an effective mass or gap in a band structure, which is the viewpoint taken here. However, an alternative viewpoint of the framework we present could be to interpret this mass as a real particle mass. This could then serve as a starting point for a holographic description for e.g. strongly coupled ultracold Fermi gases, which contain massive atoms.

In experiments we are usually interesed in single-particle spectral functions rather than the correlation functions of a composite fermion that are typically obtained in holography. Such single-particle spectral functions can be obtained from semiholography [80, 81]. Therefore, this paper also covers the incorporation of the aformentioned extension to massive Dirac fermions in a semiholographic framework.

This paper is organized as follows. In section 2, we firstly present the pro-

cedure to obtain the Dirac fermion dynamics from holography. This means that we first specify a suitable gravitational background and then present the equations corresponding to the probe fermions propagating on top of this background. Moreover, in this section we also outline the procedure to obtain both the holographic and the semiholographic Green's functions. We present our results in section 3, where we compute the fermionic spectra using numerical solutions to the equations presented in section 2. Concluding in section 4, we discuss our results and comment on possible future directions.

## 3.2 Obtaining massive Dirac fermions from holography

In this section we outline the procedure that we follow to obtain the dynamics of a Dirac fermion with a Dirac mass from holography. This procedure basically consists of solving two sets of coupled differential equations. We start by describing the first set, which gives us the gravitational bulk background that fixes quantities such as the temperature and chemical potential in the boundary field theory. We then derive the second set of differential equations, which describes the propagation of probe fermions in this bulk and gives us the holographic Green's function in the boundary theory. Finally, we derive an expression for the semiholographic Green's function of the Dirac fermion. To this end we use a dynamical-source model which is very similar to the one described in [81], where the semiholographic Green's function for a chiral fermion is derived.

We refer to appendix 3.A for conventions on the Dirac theory and the dimensionless units. Moreover, we always work in $d = 4$ spatial dimensions in the bulk, implying that we consider a three-dimensional system on the boundary.

### 3.2.1 Gravitational theory

We wish to study a boundary theory containing massive Dirac fermions at nonzero chemical potential. As is well known, we can introduce the chemical potential by adding a $U(1)$ gauge field $A_\mu$ to the bulk [56]. As in Ref. [41], we describe the mass deformation by adding a scalar field $\phi$ to the bulk. The mass of $\phi$ is fixed to $m_\phi^2 = -3$, such that the operator dual to $\phi$ has

dimension $\Delta = 2 + \sqrt{4 + m_\phi^2} = 3$. This agrees with the dimension of the operator $\langle \bar{\psi}\psi \rangle$ in a free boundary theory. Hence, the dimensions of the resulting deformation of the boundary theory match the dimensions of a free fermionic mass deformation $M_\psi \bar{\psi}\psi$. We discuss the choice of the mass $m_\phi^2$ in more detail in section 3.2.2.3. The source of the scalar field then acts as a Dirac mass $M_\psi$ on the boundary. The gravitational background we use therefore follows from the action:

$$S_{\text{background}} = \int \mathrm{d}^5 x \sqrt{-g} \left( R + 12 - \frac{1}{4} F^2 - \frac{1}{2} \left( (\partial\phi)^2 + m_\phi^2 \phi^2 \right) \right) . \tag{3.1}$$

Considering static solutions with planar symmetry, we write the *Ansatz* for the metric as

$$\mathrm{d}s^2 = -f(r) e^{-\chi(r)} \mathrm{d}t^2 + \frac{\mathrm{d}r^2}{f(r)} + r^2 \mathrm{d}\mathbf{x}^2 , \tag{3.2}$$

where $(t, r, \mathbf{x})$ denotes the spacetime position in the bulk. Moreover, we use a temporal gauge field $A = A_t(r)\mathrm{d}t$ and $\phi = \phi(r)$ due to planar symmetry. The coordinate $r$ is such that the black-brane horizon is at $r = r_+$, where $f(r_+) = 0$, and the boundary is at $r = \infty$. The Hawking temperature is then given by

$$T = \frac{f'(r_+) e^{-\chi(r_+)/2}}{4\pi} \tag{3.3}$$

and gives the temperature of the boundary theory. The equations of motion describing the background theory are

$$\phi'' + \left( \frac{f'}{f} + \frac{3}{r} - \frac{\chi'}{2} \right) \phi' + \frac{3}{f} \phi = 0 , \tag{3.4}$$

$$A_t'' + \left( \frac{3}{r} + \frac{\chi'}{2} \right) A_t' = 0 , \tag{3.5}$$

$$\chi' + \frac{r}{3} \phi'^2 = 0 , \tag{3.6}$$

$$f' + \left( \frac{2}{r} - \frac{\chi'}{2} \right) f + \frac{r}{6} e^{\chi} A_t'^2 - \frac{r}{2} \phi^2 - 4r = 0 . \tag{3.7}$$

Notice that this background is very similar to those used to describe the holographic superconductor [52], with a fixed bulk scalar mass and an uncharged bulk scalar. Therefore, following the arguments in Ref. [52], a solution to

these equations is again determined by two initial conditions at the horizon $r_+$, namely $\phi(r_+)$ and $A_t'(r_+)$, assuming $A_t(r_+) = 0$. Moreover, using the following symmetry of the equations of motion,

$$r \to ar, \qquad (t, \mathbf{x}) \to (t, \mathbf{x})/a, \qquad f \to a^2 f, \qquad A_t \to a A_t, \quad (3.8)$$

we can put $r_+ = 1$. However, in contrast to the holographic superconductor, the solutions we consider here will also have a fixed nonzero scalar source term $\phi_s$, which is dual to the Dirac mass on the boundary. This means that both initial conditions that determine the background remain free, since we do not have to shoot for a solution without a source. The background is then described by two parameters, which are any two dimensionless ratios formed with the temperature $T$, the source $\phi_s$ and the chemical potential $\mu$ per unit charge, which follows from the boundary value of $A_t$.

One may wonder what happens with the instability that causes the phase transition for the holographic superconductor. A condition for this instability of the Reissner-Nordström solution (with $\phi = 0$) against the spontaneous formation of scalar hair is given by [55]

$$q_\phi^2 > \frac{m_\phi^2}{2} + \frac{d(d-1)}{8}. \quad (3.9)$$

Since in our case $d = 4$, $m_\phi^2 = -3$ and $q_\phi = 0$, we do not satisfy this condition. Hence we do not expect this instability to occur, so that a solution with a nontrivial scalar profile should always have a nonzero source term.

### 3.2.2 Dirac Fermions

We can calculate fermionic Green's functions by having probe Dirac fermions propagate on the fixed background described in the previous section. This is similar to the procedure presented in Refs. [74, 81]. However, the resulting fermionic Green's functions on the boundary correspond to a chiral fermion. The reason is that the Dirac equation in the bulk imposes a relation between the two chiral components of the probe fermion on the boundary. Let us quickly review this case. Denoting the probe fermion by $\psi$, we define the components

$$\psi_{R,L} = \frac{1}{2}\left(1 \pm \Gamma^{\underline{r}}\right)\psi, \qquad \psi_L = \begin{pmatrix} 0 \\ \psi_- \end{pmatrix}, \qquad \psi_R = \begin{pmatrix} \psi_+ \\ 0 \end{pmatrix}, \quad (3.10)$$

where the plus (minus) sign corresponds to $\psi_R$ ($\psi_L$). Note that $\psi = \psi_R + \psi_L$, whereas $\psi_\pm$ are two-component spinors with definite chirality on the boundary. We then add the following action to the bulk:

$$S_{\text{Weyl}} = ig_f \int \mathrm{d}^5x\sqrt{-g}\bar{\psi}\left(\not{D} - M\right)\psi + ig_f \int \mathrm{d}^4x\sqrt{-h}\bar{\psi}_R\psi_L. \tag{3.11}$$

Here $M$ is the bulk Dirac mass, $g_f$ is a coupling constant, $D_\mu = \nabla_\mu - iqA_\mu$ with $\nabla_\mu$ the spinor covariant derivative and $q$ the fermion bulk charge, so that the chemical potential of the spinor is $\mu = qA_t(\infty)$. The boundary action is included to make the variational principle well defined, and is consistent with the Dirichlet boundary condition $\delta\psi_R = 0$. As shown in Ref. [81], writing out the Dirac equation $\left(\not{D} - M\right)\psi = 0$ in chiral components reveals that the relation between them can be written in the form

$$\psi_-(r,k) = -i\xi(r,k)\psi_+(r,k), \tag{3.12}$$

where we Fourier transformed the spinors on slices of constant $r$. As a consequence, the action (3.11) evaluated on shell can be written as

$$S_{\text{Weyl}}^{\text{on shell}} = -ig_f \int_{r=r_0} \frac{\mathrm{d}^4k}{(2\pi)^4}\sqrt{-h}\psi_+^\dagger\psi_- = -g_f \int_{r=r_0} \frac{\mathrm{d}^4k}{(2\pi)^4}\sqrt{-h}\psi_+^\dagger\xi\psi_+. \tag{3.13}$$

Here $r_0$ is a cut-off surface, which as we shall explain later is important when computing a Green's function. Ultimately, we take the limit of $r_0$ going to infinity. From the above action it is clear that $\xi$ is proportional to the holographic Green's function for the chiral boundary operator that is sourced by the boundary value of the chiral spinor $\psi_+$. In other words, the chiral component $\psi_R$ of $\psi$ acts as a source for the chiral operator whose expectation value is contained in $\psi_L$, so that after integrating out $\psi_L$ we are left with the effective action for a chiral fermion. As described in e.g. Ref. [81], from the Dirac equation we can then derive a differential equation for $\xi$. Solving this using infalling boundary conditions, the holographic retarded Green's function for the chiral operator $O$ that couples to $\psi_+$ then follows from

$$G_O(k) = \lim_{r_0\to\infty} r_0^{2M}\xi(r_0,k). \tag{3.14}$$

In the procedure above we have seen that we have to integrate out half of the degrees of freedom of the probe fermion. Therefore, in order to describe a

Dirac fermion on the boundary, we double the amount of degrees of freedom by introducing two bulk fermions $\psi^{(1)}$ and $\psi^{(2)}$. Our goal is then to derive an effective action similar to equation (3.13), but this time with four-component spinors. Using the Dirichlet boundary conditions $\delta\psi_R^{(1)} = 0$ and $\delta\psi_L^{(2)} = 0$, we can derive such an effective action that contains the two chiral fermions $\psi_+^{(1)}$ and $\psi_-^{(2)}$. In order to describe a massive Dirac spinor, we also need to couple these chiral components. We do this by introducing a Yukawa interaction in the bulk, that couples the two fermions to the scalar field with coupling constant $g_Y$. The total action, including the boundary terms consistent with the abovementioned Dirichlet boundary conditions, then looks as follows:

$$\begin{aligned} S_{\text{Dirac}} = {} & ig_f \int \mathrm{d}^5x\sqrt{-g}\left(\bar{\psi}^{(1)}\left(\not{D} - M\right)\psi^{(1)} + \bar{\psi}^{(2)}\left(\not{D} + M\right)\psi^{(2)}\right) \\ & + ig_Y \int \mathrm{d}^5x\sqrt{-g}\phi\left(\bar{\psi}^{(1)}\psi^{(2)} + \bar{\psi}^{(2)}\psi^{(1)}\right) \\ & + ig_f \int \mathrm{d}^4x\sqrt{-h}\left(\bar{\psi}_R^{(1)}\psi_L^{(1)} - \bar{\psi}_L^{(2)}\psi_R^{(2)}\right). \end{aligned} \tag{3.15}$$

Note that we took the mass of $\psi^{(2)}$ to be $-M$ so that the asymptotic behaviors of the sources $\psi_R^{(1)}$ and $\psi_L^{(2)}$ are equal [78]. The equations of motion following from this action are

$$\left(\not{D} - M\right)\psi^{(1)} = -\lambda\phi\psi^{(2)}, \tag{3.16}$$

$$\left(\not{D} + M\right)\psi^{(2)} = -\lambda\phi\psi^{(1)}, \tag{3.17}$$

where $\lambda = g_Y/g_f$. Notice that without the Yukawa term, we would just end up with two copies of eq. (3.13) and therefore describe two uncoupled chiral fermions. The corresponding Green's function would then be ungapped, and could therefore not correspond to the Green's function of the fermions that appear in the Dirac mass deformation that we introduced by adding the scalar field to the background. Hence a term such as the Yukawa term is necessary if we want to describe the dynamics of the Dirac fermion at the boundary. There may however be other possibilities to couple the two chiral components. This Yukawa term has the additional advantage that it does not change scaling dimensions of the operators dual to the bulk spinors.

Let us now define the two bulk Dirac spinors $\Psi \equiv \psi_R^{(1)} + \psi_L^{(2)}$ and $\eta \equiv$

$\psi_L^{(1)} - \psi_R^{(2)}$, i.e.,

$$\Psi = \begin{pmatrix} \psi_+^{(1)} \\ \psi_-^{(2)} \end{pmatrix}, \qquad \eta = \begin{pmatrix} -\psi_+^{(2)} \\ \psi_-^{(1)} \end{pmatrix}. \tag{3.18}$$

With our choice of the Dirichlet boundary conditions, $\Psi$ contains the sources. Similarly to the chiral case, we would then like to integrate out the other components that are contained in $\eta$, and derive an effective action for $\Psi$. Evaluating the action (3.15) on shell, the bulk terms vanish and we can write the boundary term as

$$S_{\text{Dirac}}^{\text{on shell}} = ig_f \int \mathrm{d}^4x \sqrt{-h} \bar{\Psi} \eta. \tag{3.19}$$

Rescaling the spinors to get rid of the spin connection, see the discussion around eq. (3.76) in appendix 3.A.2 for details, the Dirac equation in momentum space can be written as

$$-\left(e_{\underline{r}}^r \partial_r + M\right) \eta + \left(i\tilde{\not{k}} + \lambda\phi\right) \Psi = 0, \tag{3.20}$$

$$\left(e_{\underline{r}}^r \partial_r - M\right) \Psi + \left(i\tilde{\not{k}} - \lambda\phi\right) \eta = 0. \tag{3.21}$$

Here $\tilde{k}_\mu = (-(\omega + qA_t), \mathbf{k})$ so that the slash operator has no $r$-component. As in the chiral case, this imposes a relation between $\Psi$ and $\eta$ which can be written as

$$\eta(r,k) = -i\Xi(r,k)\Psi(r,k). \tag{3.22}$$

The on-shell action then becomes

$$S_{\text{Dirac}}^{\text{on shell}} = g_f \int_{r=r_0} \frac{\mathrm{d}^4k}{(2\pi)^4} \sqrt{-h} \bar{\Psi} \Xi \Psi. \tag{3.23}$$

Here we can see that the $4 \times 4$ matrix $\Xi$ is related to the Green's function for the fermionic operator $O$ that is sourced by the boundary value of the Dirac spinor $\Psi$. More precisely, using infalling boundary conditions that we specify later, the holographic Green's function is given by

$$G_O(k) = -\lim_{r_0 \to \infty} r_0^{2M} \Gamma^{\underline{0}} \Xi(r_0, k). \tag{3.24}$$

We will proceed by deriving a differential equation with which we can compute $\Xi$ directly.

#### 3.2.2.1 Computing the holographic Green's function

Using the Dirac equations in (3.20) and (3.21), we can derive a differential equation which we can solve for $\Xi$, thereby obtaining the holographic Green's function through eq. (3.24). Taking the derivative of (3.22) gives

$$\Xi e^r_{\underline{r}}\partial_r\Psi = ie^r_{\underline{r}}\partial_r\eta - e^r_{\underline{r}}\partial_r\Xi\Psi. \tag{3.25}$$

Multiplying (3.21) by $\Xi$ from the left and substituting the above then gives

$$ie^r_{\underline{r}}\partial_r\eta - e^r_{\underline{r}}\partial_r\Xi\Psi - M\Xi\Psi + \Xi\left(i\tilde{\not{k}} - \lambda\phi\right)\eta = 0. \tag{3.26}$$

Eliminating $\partial_r\eta$ using (3.20) and $\eta$ using (3.22) ultimately gives

$$\left(-(e^r_{\underline{r}}\partial_r + 2M)\Xi + i\left(i\tilde{\not{k}} + \lambda\phi\right) - i\Xi\left(i\tilde{\not{k}} - \lambda\phi\right)\Xi\right)\Psi = 0. \tag{3.27}$$

This shows that we can compute $\Xi$ by solving the first-order nonlinear differential $4\times 4$ matrix equation between the brackets. However, we can greatly reduce the amount of equations we need to solve by exploiting rotational symmetry to set $k_\mu = (-\omega, 0, 0, k_3)$. Using symmetry we can then write[1]

$$\Xi = \Xi_0\Gamma^{\underline{0}} + \Xi_3\Gamma^{\underline{3}} + \Xi_c\mathbb{I}_4 \tag{3.28}$$

where $\mathbb{I}_4$ is the $4\times 4$ identity matrix. The *Ansatz* above in (3.28) shows that there are only three degrees of freedom for which we have to solve. However, it is more insightful to write the equations in eq. (3.27) in terms of $\Xi_\pm \equiv \Xi_0 \pm \Xi_3$. This yields

$$\begin{aligned}
(e^r_{\underline{r}}\partial_r + 2M)\Xi_\pm &= \left(\tilde{\omega}e^0_{\underline{0}} \mp k_3 e^3_{\underline{3}}\right)\left(1 - \Xi_c^2\right) + \left(\tilde{\omega}e^0_{\underline{0}} \pm k_3 e^3_{\underline{3}}\right)\Xi_\pm^2 + 2i\lambda\phi\Xi_c\Xi_\pm, \\
(e^r_{\underline{r}}\partial_r + 2M)\Xi_c &= \left(\tilde{\omega}e^0_{\underline{0}} + k_3 e^3_{\underline{3}}\right)\Xi_+\Xi_c + \left(\tilde{\omega}e^0_{\underline{0}} - k_3 e^3_{\underline{3}}\right)\Xi_-\Xi_c \\
&\quad + i\lambda\phi\left(1 + \Xi_c^2 - \Xi_+\Xi_-\right),
\end{aligned} \tag{3.29}$$

where $\tilde{\omega} = \omega + qA_t$. As a check, notice that for $\lambda = \psi^{(2)} = 0$ the lower-left $2\times 2$ block of $\Xi$ corresponds to the matrix defined in (3.12) for the chiral case. From (3.28) we see that the eigenvalues of this block are exactly $\Xi_\pm$.

[1] This can also be shown by solving (3.21) for $\eta$ and reading off the matrix structure of $\Xi$.

Setting $\lambda = \Xi_c = 0$ in (3.29) indeed recovers the equation for the chiral case, see e.g. Eq. (2.31) in Ref. [81].

These equations can now be solved numerically to obtain the matrix $\Xi$. As they are first-order ODE's, we need to impose one initial condition for each component. Since only $e^0_{\underline{0}}$ diverges at $r_+$, we demand that in both equations the coefficient of this factor vanishes at the horizon. The second equation then yields either $\Xi_c(r_+) = 0$ or $\Xi_+(r_+) = -\Xi_-(r_+)$. However, the latter is not consistent with the infalling boundary conditions, for which we know from the chiral case that the result is $\Xi_\pm(r_+) = i$. We conclude that we must impose $\Xi_c(r_+) = 0$. The first equation then gives that $\Xi_\pm(r_+) = \pm i$, where the infalling boundary conditions require that we choose $+i$ for both cases.

#### 3.2.2.2 Obtaining the semiholographic Green's function

Next, we use semiholography to derive an expression for the single-particle Green's function. We note that our approach is slightly different from the work in Ref. [80], where the authors use semiholography to capture universal IR physics. In contrast, our objective is to use semiholography to obtain the Green's function of an elementary fermion that is for instance measurable in ARPES experiments. To this end, we follow the approach outlined in Ref. [81] for the chiral case, which is constructed such that the obtained semiholographic Green's function $G_R$ satisfies the sum rule that in our case reads

$$\frac{1}{4\pi}\int_{-\infty}^{\infty} \mathrm{d}\omega \,\mathrm{Im}\,\mathrm{Tr}\, G_R(\omega, \mathbf{k}) = 1. \tag{3.30}$$

This procedure implies that we interpret the ultraviolet (UV) cut-off surface at a fixed radial coordinate $r = r_0$ as the boundary on which the single fermions live and interact with the CFT. In practice this means that the sources become dynamical and that the holographic Green's function derived above becomes the self-energy of the elementary fermion. In particular we note that the semiholographic Green's functions obtained in this manner are not restricted to IR physics, as the sum rule above also implies.

Above we have calculated the holographic contribution to the effective action, which is given by eq. (3.23). To this we add the free action on the UV brane for the source $\Psi$:

$$S_{UV} = iZ\int_{r=r_0} \mathrm{d}^4x\sqrt{-h}\bar{\Psi}\left(\not{D} - \tilde{M}_0\right)\Psi. \tag{3.31}$$

Note that we can add this action since we chose the Dirichlet boundary condition corresponding to $\delta\Psi = 0$. The total effective boundary action can then be written as

$$S_{\text{eff}} = \frac{Z\sqrt{-h}}{r_0}\int_{r=r_0}\frac{\mathrm{d}^4k}{(2\pi)^4}\bar{\Psi}\left(-\Gamma^{\underline{a}}\tilde{k}_a - i\tilde{M}_0 r_0 + \frac{g_f r_0}{Z}\Xi\right)\Psi, \tag{3.32}$$

where we Fourier transformed the fields and used that $e^0_{\underline{0}} \approx 1/r_0$ for $r_0$ near the boundary. Notice that the kinetic term now becomes canonically normalized upon rescaling the fields as $\Psi \to \sqrt{r_0/Z\sqrt{-h}}\Psi$. We can then take the following limit:

$$\begin{aligned} &r_0 \to \infty, && g_f \to 0, && \tilde{M}_0 \to 0, \\ &g \equiv \frac{g_f r_0^{1-2M}}{Z} = \text{const.}, && M_0 \equiv \tilde{M}_0 r_0 = \text{const.} \end{aligned} \tag{3.33}$$

The effective action for the elementary Dirac fermion $\Psi$ can then be written as

$$S_{\text{eff}} = \int\frac{\mathrm{d}^4k}{(2\pi)^4}\Psi^\dagger G_R^{-1}\Psi. \tag{3.34}$$

Here the inverse Green's function is given by

$$G_R^{-1}(k) = \begin{pmatrix}\sigma\cdot\tilde{k} & iM_0\\ -iM_0 & -\bar{\sigma}\cdot\tilde{k}\end{pmatrix} + \Sigma \tag{3.35}$$

where $\sigma = (\mathbb{1}_2, \sigma^i)$ and $\bar{\sigma} = (-\mathbb{1}_2, \sigma^i)$ with $\sigma^i$ the Pauli matrices, and where we defined the self-energy

$$\Sigma(k) \equiv g\Gamma^{\underline{0}}\lim_{r_0\to\infty} r_0^{2M}\Xi(r_0, k). \tag{3.36}$$

Using again the rotational symmetry to choose the momentum as $\tilde{k}_\mu = (-\tilde{\omega}, 0, 0, k_3)$ and using the notation of (3.28), we can also write the Green's function as

$$G_R^{-1}(\omega, k_3) = \Gamma^{\underline{0}}\left(\left(\tilde{\omega} + g\Xi_0\right)\Gamma^{\underline{0}} + \left(-k_3 + g\Xi_3\right)\Gamma^{\underline{3}} + \left(-iM_0 + g\Xi_c\right)\mathbb{1}_4\right). \tag{3.37}$$

This expression is evaluated at the boundary, so that $\tilde{\omega} = \omega + \mu$. We absorbed a factor $r_0^{2M}$ in the components of $\Xi$, such that these are finite at

the boundary $r_0 \to \infty$. The above expression shows that $\Xi_0$ is related to a wavefunction renormalization, whereas $\Xi_c$ acts like a mass renormalization.

When $g$ becomes large, the inverse Green's function will be dominated by the self-energy in eq. (3.36). In this limit we recover the holographic Green's function, albeit rescaled by $1/g$ and in alternative quantization. The latter implies that this Green's function corresponds to the Dirichlet boundary conditions $\delta\psi_R^{(2)} = \delta\psi_L^{(1)} = 0$, which gives the inverse of the Green's function in standard quantization.

#### 3.2.2.3 Interpreting semiholography

Before continuing to our results, we briefly comment on the physical picture we have in mind when applying the semiholographic procedure described above. On the one hand, we introduce free single fermions $\Psi$ living on a UV cut-off surface, located at $r_0$. On the other hand, we have a (deformed) CFT, containing a composite fermionic operator $O$.[2] In essence, what happens in semiholography is that we linearly couple these two theories and subsequently integrate out the CFT part in order to obtain the effective Green's function of the fermion. In other words, we describe single fermions $\Psi$ interacting with a fermionic operator $O$ of the CFT.

Since we are doing bottom-up holography, it is not known what the exact physical interpretation of $O$ is. A possible interpretation is to describe single fermions interacting with a completely unrelated composite fermionic operator. However, the physical picture we have in mind is a fermionic condensed-matter system, which at long wavelengths is described by a CFT with a number of collective variables of these fermions, e.g. electrons or atoms. In this case, the composite operator $O$ in the CFT 'contains' the single fermion of interest, such as the electron or the atom. Such a 'self-consistent' interpretation imposes additional restrictions on our model. One example is the choice of the parameter $m_\phi^2$ in the bulk, which we then should indeed choose such that it describes a free-fermion mass deformation. This is because we know that the elementary fermion is described by a free theory in the far UV. Hence, if the fermion is a building block of the CFT, such a mass deformation should exist in the CFT. In contrast, if the CFT is unrelated to the fermion $\Psi$, we might as well have chosen a different value for $m_\phi^2$, as it is

[2] In the description above, $O$ is the operator sourced by $\Psi$.

not clear that a mass-like deformation introduced by the dual field $\phi$ in the CFT should necessarily correspond to that of a free fermion.[3]

In our model, both theories contain a mass scale. In the theory describing the elementary fermion, this mass is denoted by $M_0$. In the CFT the mass scale is set by the source $\phi_s$ of the scalar field $\phi$. The self-consistency requirement mentioned above means that also these two mass scales should be related, and enables us to fix the ratio $M_0/\phi_s$. An argument for this is given in appendix 3.C. Although we use the fixed value presented there, i.e., $M_0/\phi_s = \sqrt[4]{\pi^2/3}$, we do not expect substantial qualitative differences in our semiholographic spectra when choosing a slightly different value for this ratio or for $m_\phi^2$ for that matter.

## 3.3 Fermionic spectral functions

Given a Green's function $G(\omega, \mathbf{k})$, we can compute the spectral function defined as

$$\rho(\omega, \mathbf{k}) = \frac{1}{\pi} \mathrm{Im}\ \mathrm{Tr}\, G(\omega, \mathbf{k}). \tag{3.38}$$

Here we can take the holographic Green's function $G = G_O$ defined in eq. (3.24) to obtain the spectral function of the fermionic operator $O$, or we can take $G = G_O^{-1}$ to obtain the holographic spectral function in alternative quantization. Alternatively, we can use the semiholographic Green's function $G_R$ defined in eq. (3.35) to obtain the spectral function for the elementary fermion $\Psi$. We can think of this as moving away from the limit $g \to \infty$ which corresponds to the holographic Green's function in alternative quantization. It is however important to keep in mind that the holographic results can be obtained independently of semiholography. An important property of the semiholographic Green's function is that in contrast to the holographic one, it obeys the sum rule in eq. (3.30), i.e.,

$$\int_{-\infty}^{\infty} \mathrm{d}\omega \rho(\omega, \mathbf{k}) = 4. \tag{3.39}$$

This implies that $G_R$ is indeed the Green's function of an elementary Dirac fermion, which is a measurable quantity that contains the information about the spectrum of the fermion dynamics. Moreover, this property allows us to

[3] See Ref. [82] for a holographic model where the value of $m_\phi^2$ is varied.

compute momentum distribution functions. The spectral function is normalized such that the sum rule gives the number of degrees of freedom, i.e., 4 for a Dirac fermion.

Before presenting our results, we take a moment to stress on which parameters the spectral functions depend. For the holographic spectral function this means we should state on which parameters the function $\Xi(\omega, \mathbf{k})$ depends. Firstly, this matrix depends on the gravitational background, which is specified by the scales $T$, $\mu$,[4] and $\phi_s$. Besides this, the self-energy depends on the parameters $\lambda$, $q$ and $M$, which all appear in eq. (3.27). Here, $\lambda$ describes the coupling strength between the chiral components of the fermion. Therefore, it is necessarily nonzero for fermions with a mass term. Moreover, the bulk charge $q$ and bulk mass $M$ of the probe fermions are dimensionless parameters that define the CFT in which we calculate the two-point function.

For the semiholographic spectral function, $M$ is restricted to the range $|M| < 1/2$. This is necessary for the sum rule and the Kramers-Kronig relations to hold [81]. The semiholographic spectral function depends on all the parameters above and in addition on $g$ and $M_0$ through eq. (3.37). The parameter $g$ is nonnegative and describes the strength of the coupling between the fermions $\Psi$ and the CFT, i.e., the strength of the self-energy. Here the limit $g \to \infty$ recovers the holographic Green's function in alternative quantization, whereas $g = 0$ corresponds to a free massive Dirac fermion. The mass scale $M_0$ is fixed by $\phi_s$ as explained in section 3.2.2.3 and in appendix 3.C. In this work we scale all dimensionful quantities with $M_0$. This means that from this point on all quantities we refer to are implicitly scaled by the appropriate power of $M_0$ to make them dimensionless.[5] We fix $q = 1$ and $M = 1/4$ unless stated otherwise. We expect that changing these values should result mostly in quantitive rather than qualitative differences in the spectra. In this paper we mainly focus on the low-temperature case $T = 1/100$, unless stated otherwise.

### 3.3.1 Undoped spectra

First of all, we concentrate on the undoped case, i.e., $\mu = 0$. Of first importance is to verify whether the procedure from section 3.2 gives us spectral functions of fermions described by massive Dirac theory. It is important

[4] Actually, $\mu = qA_t(r = \infty)$ which also depends on $q$, but this dependence is trivial.
[5] E.g. instead of $T/M_0$ we say $T$.

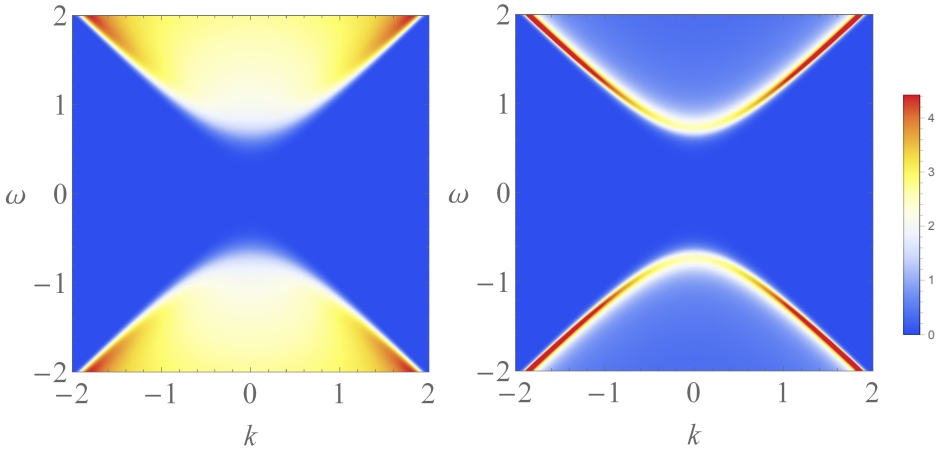


Figure 3.1: (a) The holographic spectral function. (b) The holographic spectral function in alternative quantization. In both (a) and (b), $\lambda = 1$. The legend on the right holds for both figures. Here, and in all the following plots, all quantities are made (scale) dimensionless by dividing by the appropriate power of $M_0$, and we choose $q = 1$, $M = 1/4$, $T = 1/100$ unless stated otherwise.

to note that both the holographic and the semiholographic spectral functions must contain a gap. This is because using the procedure we apply, the spectrum obtained in semiholography should correspond to strongly coupled gapped Dirac fermions. The self-energy, i.e., the holographic Green's function, then contains the effect of strong interactions between these fermions. If the gap were caused by the parameter $M_0$ only, the spectral function would instead correspond to gapped fermions interacting with a strongly coupled gapless CFT, which is not what we are after in this work. We therefore start this section by verifying the appearance of a gap in the holographic spectral functions.

#### 3.3.1.1 Holographic spectra

In figure 5.1a we show the holographic spectral functions for $\lambda = 1$, in both standard and alternative quantization. These contain a gap as desired.[6] To obtain this gap it is imperative that $\lambda$ is nonzero, since this parameter describes the coupling between chiral components. As a consequence, when $\lambda = 0$ we expect no gap in the self-energy, and neither do we expect a peak at nonzero $\omega$ in alternative quantization. This is indeed the case, as is shown in figure 3.2, where we study the dependence on $\lambda$ of the peak appearing in the holographic spectral function in alternative quantization. We observe that a peak at nonzero $\omega$ appears for values of $\lambda$ higher than a nonzero lower bound. Furthermore, for larger values of $\lambda$, the position of the peak grows approximately linearly with $\lambda$, whereas the height remains almost constant. We expect these results by noting that eq. (3.27) only depends on the combination $\lambda\phi$, rather than $\lambda$ and $\phi$ seperately. Therefore, asymptotically the relevant scale is $\lambda M_0$ rather than $M_0$.[7] In the low-temperature regime, $\lambda M_0$ is then the only dimensionful scale left and we therefore expect the peak to be proportional to $\lambda M_0$. This also explains the discrepancy observed in figure 3.2b at low $\lambda$, since here the scale $T/\lambda M_0$ becomes large. We have indeed observed that a peak appears for smaller values of $\lambda$ as well when lowering the temperature further. However, the initial conditions corresponding to eq. (3.29) depend on $\lambda$ but not on $M_0$. It is therefore not completely obvious to us that the position of the peak should grow linearly with $\lambda$, but the numerics show that this is indeed the case. Finally, notice that due to the width of the peak, a large enough value of $\lambda$ is needed before the gap appears. This spread is not solely due to the nonzero temperature, which we have checked numerically by calculating the same spectral functions at lower temperatures and not observing a decrease in the width. As a consequence the observed peak cannot correspond to a long-lived quasiparticle, which we indeed would not expect from a holographic spectral function describing unparticles in a mass-deformed conformal field theory.

[6] Note that this is not a hard gap.

[7] In holography the relevant scale is actually the source $\phi_s$ rather than $M_0$, but as stated before their ratio is fixed in this work.

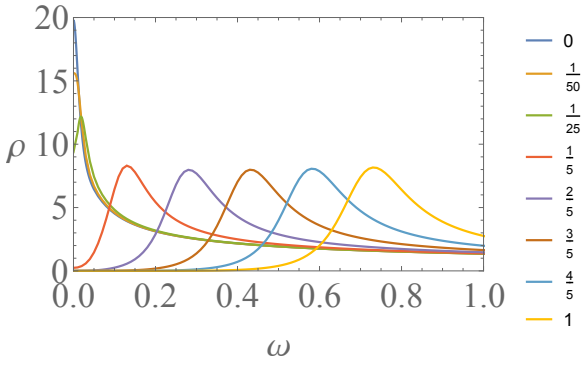


(a)

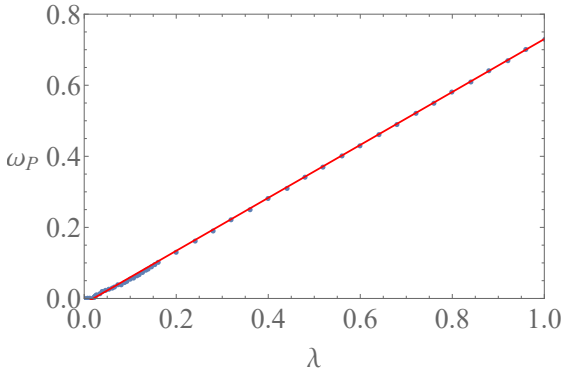


(b)

Figure 3.2: (a) The holographic spectral function in alternative quantization at zero momentum. The legend shows the used values of $\lambda$. (b) The dependence of the peak position $\omega_P$ on $\lambda$.

#### 3.3.1.2 Conductivity

Having shown that a gap is introduced in the holographic spectral functions, it is interesting to see if the CFT now indeed behaves as an insulator. We can check whether this is the case by calculating the conductivity of the CFT. In order to do so, we introduce fluctuations of the gauge field component $\delta A_x(x_\mu) = \delta a_x(r)e^{-i\omega t}$ to the theory. These fluctuations are not coupled to fluctuations of the other fields, even though the background has a nontrivial scalar profile. In particular, in contrast to the holographic superconductor

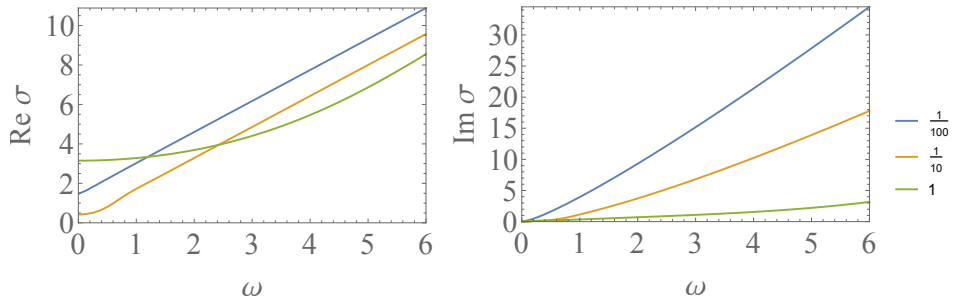


(a) (b)

Figure 3.3: The (a) real and (b) imaginary part the conductivity $\sigma$ of the CFT. The legend shows the value of the temperature for both figures.

model, these gauge fluctuations are not coupled to the scalar fluctuations $\delta\phi$ because the scalar field is uncharged. Moreover, the metric fluctuations $\delta g_{tx}$ are not sourced because we are still considering the undoped case. The fluctuations $\delta a_x$ then satisfy the equation of motion[8]

$$\delta a_x'' + \left(\frac{f'}{f} - \frac{\chi'}{2} + \frac{1}{r}\right)\delta a_x' + \frac{e^{\chi}\omega^2}{f^2}\delta a_x = 0. \tag{3.40}$$

This equation has the asymptotic solution

$$\delta a_x = \delta a_{x(0)} + \delta a_{x(1)} r^{-2} + \frac{\omega^2}{2}\delta a_{x(0)} r^{-2}\log(r) + \cdots . \tag{3.41}$$

By analyzing the action up to second order in the fluctuations, we can then find that the conductivity is given by [83]

$$\sigma(\omega) = 2\frac{\delta a_{x(1)}}{i\omega\delta a_{x(0)}} - \frac{\omega}{2i}, \tag{3.42}$$

where the coefficients $\delta a_{x(0)}$ and $\delta a_{x(1)}$ are found by solving eq. (3.40) with infalling boundary conditions at the horizon.

The results shown in figure 3.3 show that the conductivity does not behave as an insulator. For high temperatures the DC conductivity $\sigma(0)$ is linear

[8] In eq. (3.40) and eq. (3.41), we have not scaled dimensionful quantities like $\omega$ and $\delta a_{x(1)}$ by the mass $M_0$.

in $T$, as we know from the conductivity in a Schwarzschild background [84]. For low temperatures, where the mass scale dominates, this linearity breaks down as expected. However, the mass scale does not induce a gap in the CFT conductivity. A possible explanation for this is the presence of other degrees of freedom in the CFT that are not gapped out by the mass deformation introduced in the model. A similar result was found in Refs. [1, 41]. We could have anticipated this result as well from the fact that the calculation is independent of the coupling $\lambda$, which as we saw in the previous section generates the gap in the spectral functions. We expect however that the fermionic contribution to the conductivity, which can be calculated using the semiholographic fermionic Green's function using the approach explained in Refs. [78, 85, 86], does contain a gap and describes an insulator.

#### 3.3.1.3 Semiholographic spectra

The holographic spectra in section 3.3.1.1 show that the self-energy of the semiholographic Green's function contains a gap. Therefore, the gap in the semiholographic spectra is caused by both the bare mass $M_0$ and the gap in the self-energy. Note that here we are assuming a nonzero coupling $\lambda$. Otherwise, the Dirac field $\Psi$ would correspond to two independent Weyl fermions. Another way of seeing this is by noting from eq. (3.29) that $\Xi_c = 0$ when either $\lambda = 0$ or $\phi = 0$.

In figure 3.4 we show the semiholographic spectral function for $\lambda = 1$ and $g = 1$, which also contains a gap. For the specific set of parameters chosen there, we see that the mass is renormalized to a value smaller than the bare mass. From our previous analysis of figure 3.2b, which gives the values of the renormalized mass for large $g$, we know that this is not always the case. This is again evident in figure 3.5, where we study the dependence of the spectral functions at zero momentum on the coupling constants $g$ and $\lambda$. The values of $\lambda$ in the figures are large enough such that the self-energy has a gap. Clearly, for $g = 0$ the spectral function resembles that of a free Dirac fermion with mass $M_0$. Upon increasing $g$, for both values of $\lambda$ in the figures the mass first renormalizes to a smaller value, but ultimately converges for large $g$ to the value shown in figure 3.2b that is obtained in the holographic spectral functions, which depending on the value of $\lambda$ can be either smaller or bigger than the bare mass. A remarkable feature in both the cases shown is that there exists a value of $g$ at which the mass renormalizes to zero. This

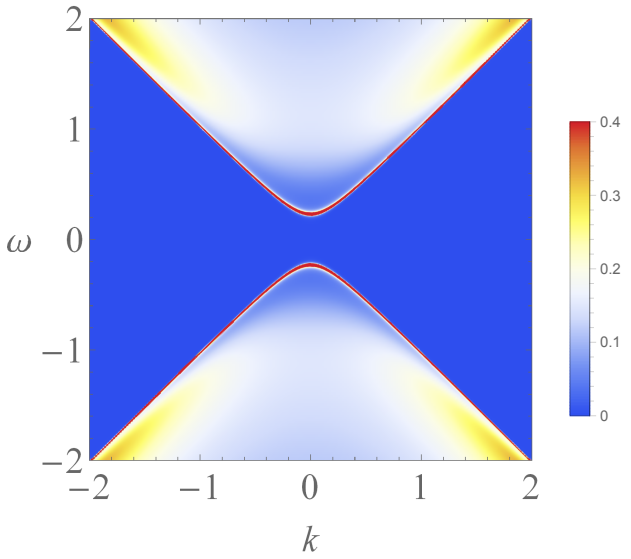


Figure 3.4: The undoped spectral function of the elementary fermion for $\lambda = 1$ and $g = 1$.

can be understood from the general form of the Green's function in eq. (3.37), where we see that the mass is renormalized with a value proportional to $g$. To be more precise, by studying the symmetries of the equations in eq. (3.29), we can write the Green's function for small values of $\omega$ and $k_3$ as

$$G_R^{-1}(k) = \begin{pmatrix} Z_0 \sigma \cdot k & iM_{\text{eff}} \\ -iM_{\text{eff}} & -Z_0 \bar{\sigma} \cdot k \end{pmatrix} \tag{3.43}$$

where $Z_0$ and $M_{\text{eff}}$ are given by

$$Z_0 = 1 + g\partial_\omega \Xi_0(k_\mu = 0), \tag{3.44}$$

$$M_{\text{eff}} = M_0 + ig\Xi_c(k_\mu = 0). \tag{3.45}$$

Referring to appendix 3.B for details, we note that $Z_0$ and $M_{\text{eff}}$ are real constants and $Z_0 > 0$. From this expression it follows that the effective mass changes sign when $g$ assumes the critical value

$$g_c = \frac{iM_0}{\Xi_c(k_\mu = 0)}. \tag{3.46}$$

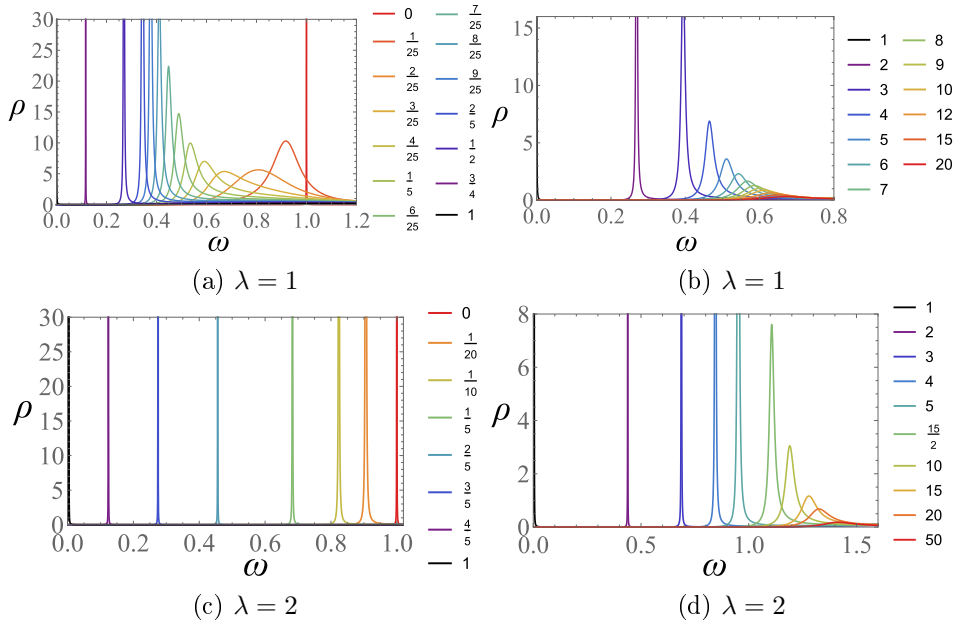


(a) $\lambda = 1$ (b) $\lambda = 1$

(c) $\lambda = 2$ (d) $\lambda = 2$

Figure 3.5: The semiholographic spectral function at zero momentum for several values of $g$. The legends show the value of $g/g_c$. In (a) and (b), $\lambda = 1$ and $g_c = 0.56$. In (c) and (d), $\lambda = 2$ and $g_c = 0.39$. These spectral functions are symmetric in $\omega$ due to particle-hole symmetry. In (c) the peaks are all very sharp because they are at frequencies inside the gap of the self-energy for $\lambda = 2$.

This signals a topological quantum phase transition similar to the one obtained by changing the sign of the mass in free Dirac theory[9] [87–89]. This can for example be seen by defining a winding number as in Ref. [88], which changes when inverting the sign of the Dirac mass.[10] We note that this transition is topological only when the symmetry protecting this winding number is not broken during the transition. Due to the symmetry of the Dirac equation it is not possible to determine which sign of the mass corresponds to

[9] Strictly speaking we cannot see the quantum phase transition, since the temperature in our numerical computation is never exactly equal to zero.

[10] Alternatively, this can be done by studying the behavior of the eigenspinor components of the Dirac Hamiltonian under a parity transformation.

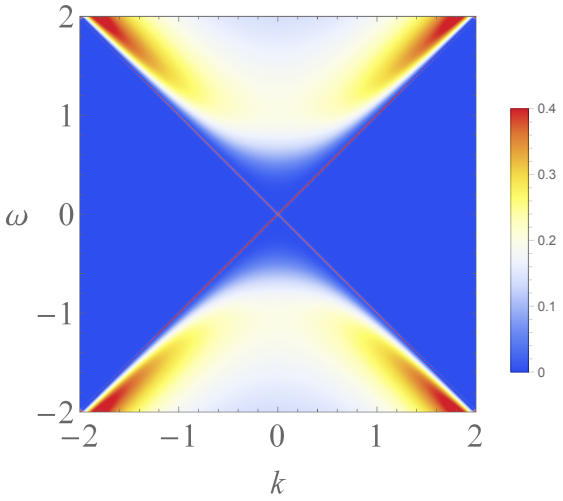


Figure 3.6: The spectral function at $\lambda = 1$ and $g = g_c = 0.56$.

a topologically trivial or nontrivial state. However, regardless of the initial sign of the mass of a state, we can say that to adiabatically transform this state into a state with a changed sign of the mass, i.e., a changed winding number, requires going through a gapless state, given that the protecting symmetry is respected during this transition. At the quantum critical point, $M_{\text{eff}} = 0$ and the spectrum looks like that of a massless quasiparticle, as shown in figure 3.6. Since the dispersion of the peak now resides inside the gap, this time it does look like an infinitely long-lived quasiparticle.

What we have thus shown is that the introduction of the additional scale $g$ in semiholography induces a topological quantum phase transition. This scale is restricted to nonnegative values. Therefore, having obtained a solution for $\Xi$, it is possible to find a quantum critical solution by choosing $g$ as in eq. (3.46), but only if $\text{Im}[\Xi_c(k_\mu = 0)] > 0$. It turns out that for $\lambda > 0$ this is always the case, although $\lambda$ should be large enough to create a gap for eq. (3.46) to hold. Hence for positive $\lambda$, the Dirac fermion described by the holographic limit $g \to \infty$ will always be topologically distinct from the free fermion described by $g = 0$. From the symmetry described in appendix 3.B we can also immediately see that for $\lambda < 0$ this is not the case, since then $\text{Im}[\Xi_c(k_\mu = 0)] < 0$. This can also be seen in figures 3.7 and 3.8. Moreover,

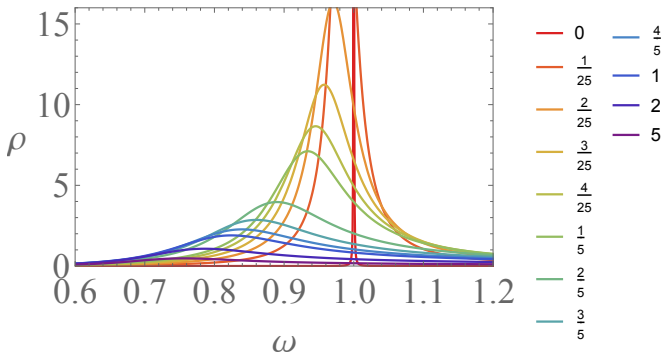


Figure 3.7: The spectral function at $\lambda = -1$ for several values of $g$. The legend shows the value of the dimensionless coupling $g$.

from the symmetry described in appendix 3.B that relates the self-energy corresponding to the bulk mass $M$ to the one for $-M$, it follows that this conclusion does not change when changing the sign of $M$. Specifically, this symmetry implies that when changing only the sign of $M$, the new value of $g_c$ is equal to the inverse of the old one. In fact, numerical analysis shows that $g_c$ is proportional to $\lambda^{-2M}$. Again, we can partially understand this by noting that in eq. (3.29) the asymptotically relevant scale is $\lambda M_0$ rather than $M_0$, so that at low temperatures and $k_\mu = 0$ the asymptotic equation yields that $\Xi_c \propto (\lambda M_0)^{2M}$. However, solving the equation asymptotically yields an integration constant of which it is not entirely clear to us why its dependence on $\lambda$ is negligible.

All the spectral functions presented in this section satisfy the sum rule in eq. (3.39), which we have verified numerically. However, in e.g. figures 3.6 and 3.4, we see that for nonzero $g$ there is also spectral weight at frequencies higher than the position of the peak. This implies that due to interactions the spectral weight of the peak decreases. Numerically integrating over frequency reveals that for the case presented in figure 3.4 the two red peaks carry less than half of the total spectral weight, which shows the significant effect of the interactions. The spread in the spectral weight continues to grow for higher $g$. In figure 3.8, for large enough values of $|\lambda|$ we can clearly distinguish the spectral weight of the peaks due to the renormalized bare mass from the weight that originates from the self-energy. This self-energy contains a continuum rather than a peak, as we can see from figure 3.1a. Therefore,

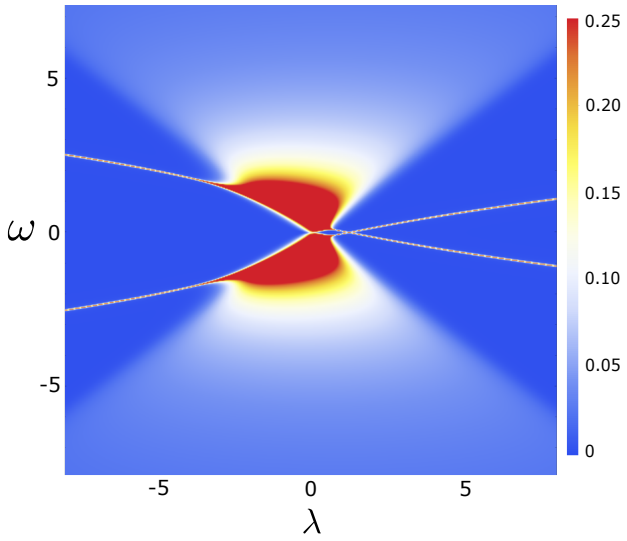


Figure 3.8: The spectral function at $g = 0.5$ and zero momentum as a function of $\lambda$. Here, the quantum critical point is clearly visible for $\lambda = 1.25$, whereas there is no critical point for a negative value of $\lambda$.

rather than an avoided crossing, we observe that the spectral weight merges into one broad peak for small values of $\lambda$. Moreover, in this figure we also see once again that a quantum phase transition occurs at a critical positive value of $\lambda$.

### 3.3.2 Doped spectra

We now turn to the case of nonzero chemical potential. Here we restrict ourselves to $\mu > 0$, as the solution for $\mu < 0$ then easily follows from particle-hole symmetry as described in appendix 3.B. One trivial effect of the chemical potential is that the spectrum will appear shifted in frequency due to the use of grand-canonical energies. More interesting effects such as the formation of Fermi surfaces occur for large enough values of $\mu$. In this subsection we firstly study holographic spectral functions containing such Fermi surfaces. We then proceed with the semiholographic Green's functions with which we can also compute the corresponding momentum distribution functions. Finally, we study the dependence on the couplings $g$ and $\lambda$ of the characteristics of the

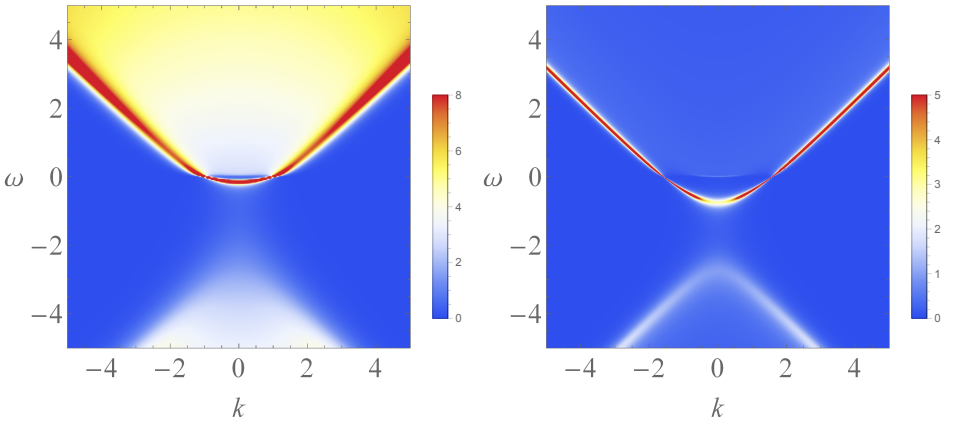


Figure 3.9: The holographic spectral function for $\mu = 2$ and $\lambda = 1$ in (a) standard and (b) alternative quantization. The Fermi surface is most clearly visible in alternative quantization, where $k_F = 1.58$.

theory near the Fermi surfaces.

#### 3.3.2.1 Formation of Fermi surfaces in the holographic spectra

The formation of Fermi surfaces in holographic models was studied before in e.g. Refs. [62, 73–76]. Here we investigate how this formation depends on the parameters in our model, in particular on the size of the gap, i.e., on $\lambda$. In the spectral functions, Fermi surfaces appear as long-lived quasiparticle states at the chemical potential, i.e., at $\omega = 0$. In other words, they appear as poles in the low-temperature spectral function at $\omega = 0$ and at a nonzero Fermi momentum $k = k_F$. Examples of such spectral functions containing a Fermi surface are shown in figure 3.9 in both standard and alternative quantization. In this figure we have set $\mu = 2$ and $\lambda = 1$. The Fermi surface is most clearly visible in alternative quantization. For a Fermi surface to appear in our model we need a sufficiently large chemical potential. This is of course a consequence of the gaps in our spectra. Moreover, we expect that since for larger values of $\lambda$ the gap grows, the chemical potential required for the formation of a Fermi surface will be higher. Conversely, for a fixed chemical potential there exists a critical coupling $\lambda_c$ at which the Fermi

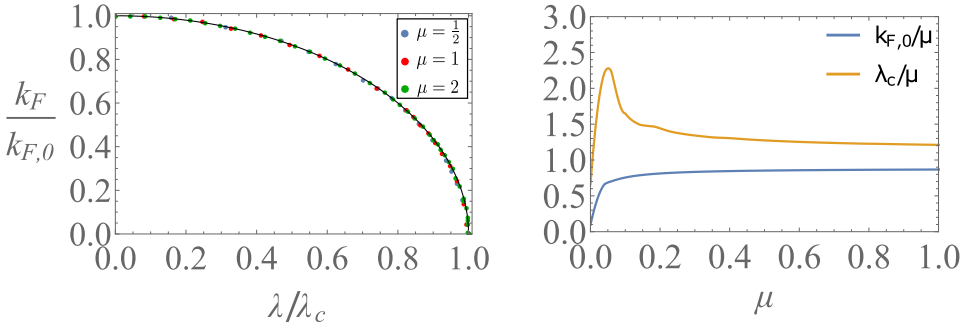


(a) (b)

Figure 3.10: (a) The Fermi momentum $k_F$ corresponding to the holographic Green's function in alternative quantization as a function of the coupling $\lambda$. The Fermi momentum is scaled with its value at $\lambda = 0$ and the coupling $\lambda$ is scaled with the value $\lambda_c$ at which the Fermi surface vanishes. The black curve corresponds to eq. (3.47). (b) The Fermi momentum at $\lambda = 0$ and the critical coupling $\lambda_c$, both scaled with the chemical potential $\mu$.

surface vanishes. This can indeed be seen in figure 3.10, where we plot the Fermi momentum of the spectral function in alternative quantization as a function of the coupling $\lambda$. From figure 3.10a it follows that when scaling the Fermi momentum with its value at $\lambda = 0$, denoted by $k_{F,0}$, the resulting curve is given by

$$\frac{k_F}{k_{F,0}} = \sqrt{1 - \frac{\lambda^2}{\lambda_c^2}}. \tag{3.47}$$

Hence, this curve is independent of $\mu$. Interestingly, this result is very reminiscent of a second-order mean-field quantum phase transition between a state with a Fermi surface and a state without one, if we think of the Fermi momentum as an order parameter. A quantum phase transition between such states was also found in the semiholographic model studied in Ref. [62] and in Ref. [79] in the context of nodal-line semimetals. Furthermore, the result looks similar to the result in non-interacting Dirac theory where $k_F = \sqrt{\mu^2 - m^2}$, with $m$ the Dirac mass of that theory. This suggests that also here we can approximate the band in figure 3.9b by $\omega + \mu = \sqrt{k^2 + m^2}$, up to some mass and wavefunction renormalization. Identifying the mass in

our model with $\lambda$,[11] this seems to suggest that $k_{F,0} \propto \mu$ and $\lambda_c \propto \mu$. As shown in figure 3.10b, this is indeed what we obtain from our numerics when $\mu$ is large enough. For smaller chemical potential the mass and wavefunction renormalization still depend on $\mu$. Notice that the intersection of the curves in 3.10b with the vertical axis occurs at nonzero values, which indicates that also for small chemical potentials $k_{F,0}$ and $\lambda_c$ are proportional to $\mu$ to leading order.

Another feature that is visible in the spectral function in figure 3.9b is a second band that is close to the chemical potential, i.e., near $\omega = 0$. Here the height of the peak is higher for lower values of $k$. A similar feature was observed in the spectral functions in Ref. [73], where the band was interpreted as a so-called critical Fermi ball. Moreover, Refs. [74, 75] report the formation of multiple Fermi surfaces in their models. However, in our model, the imaginary part of the Green's function near the second band is nonzero, so this does not cause additional Fermi surfaces. Since the band is situated at the chemical potential, independent of the value of $\lambda$, it appears to indicate the existence of a many-body fermionic bound state in the theory due to the presence of the Fermi surface that hybridizes with the composite fermions described by the spectral function. We have found that the band is also present for nonzero values of $\mu$ that are small enough such that the band is inside the gap. Therefore the binding energy of this bound state, as compared to the band gap, can be positive or negative in our models.

#### 3.3.2.2 Semiholographic spectra

Fermi surfaces in semiholographic models have been studied before in Refs. [62, 80, 90]. Here, we investigate the influence of a finite semiholographic coupling $g$ on our fermionic spectra. The semiholographic spectral function is shown in figure 3.11a for $g = 4$ and otherwise the same parameters as in figure 3.9. Qualitatively the spectrum bears resemblance to the holographic spectrum in alternative quantization in figure 3.9b, but we observe quantitative differences in the size of the gap and the location of the Fermi surface. Figure 3.11b shows the dependence of the Fermi momentum on both the couplings $\lambda$ and $g$. Here we have taken $\mu = 2$, such that at $g = 0$ there is a Fermi surface located at $k_F = \sqrt{\mu^2 - M_0^2} = \sqrt{3}$, independent of $\lambda$.

[11] This identification can be justified by figure 3.2b.

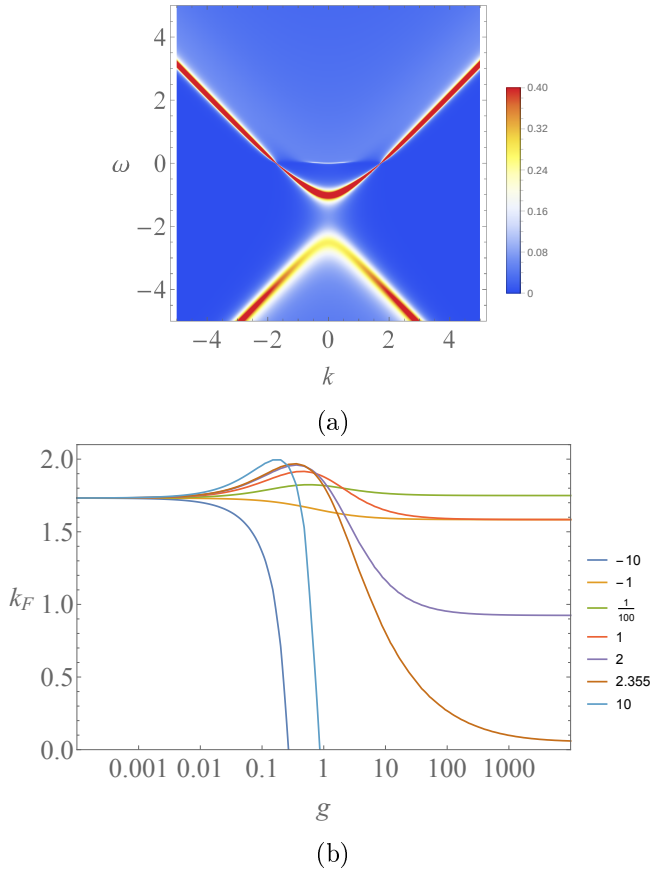


Figure 3.11: (a) The spectral function for $\mu = 2$, $\lambda = 1$ and $g = 4$. There is a Fermi surface at $k_F = 1.72$. (b) The Fermi momentum $k_F$ as a function of $g$. The legend shows the value of the coupling $\lambda$.

Furthermore, in the limit of large $g$ the Fermi momentum converges to the holographic value shown in figure 3.10. Since this value is independent of the sign of $\lambda$, the Fermi momenta for $\lambda = \pm 1$ converge to the same value. Moreover, as we have seen in the holographic case, the Fermi surface disappears for large values of $|\lambda|$, but as seen in the figure, the value at which it disappears increases as we move away from the holographic limit. Finally, we note that for $\lambda > 0$ the Fermi momentum first increases as we increase $g$, after which it decreases to ultimately converge to the large-$g$ value. Since

the Fermi momentum is largest when the effective mass vanishes, the tops of these curves correspond to the quantum critical points $g_c$ mentioned in section 3.3.1, where the spectrum is gapless. The value of $g_c$ can however not be derived from an equation similar to (3.46), since $\Xi_c(k_\mu = 0)$ is not purely imaginary for nonzero chemical potential. In contrast, for $\lambda < 0$ the Fermi momentum converges to the large-$g$ value without passing through such a quantum critical point, in accordance with the findings in section 3.3.1.

Above we considered a case where $\mu > 1$. Here, we have seen that for $g = 0$ there is a Fermi surface. In contrast, in the limit $g \to \infty$, this is only true if $|\lambda| < \lambda_c$, where $\lambda_c$ can be determined from the asymptotic value in figure 3.10b. For finite $g$, this generalizes to two $g$-dependent critical values $\lambda_{c,+}(g) > 0$ and $\lambda_{c,-}(g) < 0$, so that the spectrum only contains a Fermi surface when $\lambda_{c,-} < \lambda < \lambda_{c,+}$. From figure 3.11b we see that $\lambda_{c,+}$ increases as we lower $g$, and diverges to $\infty$ as $g \to 0$. Moreover, as we can see by comparing the curves for $\lambda = \pm 10$, we in general have that $\lambda_{c,-} \neq -\lambda_{c,+}$. The case when $\mu \leq 1$ is slightly more complicated. Here, there is no Fermi surface for the noninteracting case $g = 0$. However, we know from figure 3.10b that there is a Fermi surface when $g \to \infty$ for $|\lambda|$ sufficiently small, i.e., $|\lambda| < \lambda_c$. This means that in this case there must be a critical coupling $g$ above which a Fermi surface forms. On the other hand, for larger $|\lambda|$, there is no Fermi surface when $g = 0$ and neither when $g \to \infty$. In this case, depending on the value of $\lambda$, a Fermi surface can form at an intermediate value of $g$, which disappears again for larger $g$. Alternatively, there can also be values of $\lambda$ for which there is no Fermi surface for any value of $g$.

Besides the critical points mentioned above, we can find critical couplings $g_c$ reminiscent of the ones mentioned section 3.3.1 at which the spectrum is gapless. However, due to the nonzero imaginary part of the self-energy at nonzero doping, the spectrum will in this case be gapless for a larger range of values for $g$. Although interesting, showing the entire phase diagram with the all of the abovementioned critical couplings for all values of $g$, $\lambda$ and $\mu$ is beyond the scope of the present paper.

The semiholographic spectral functions computed in this section obey the sum rule. This allows us to define and compute the momentum distribution function, which we shall do next.

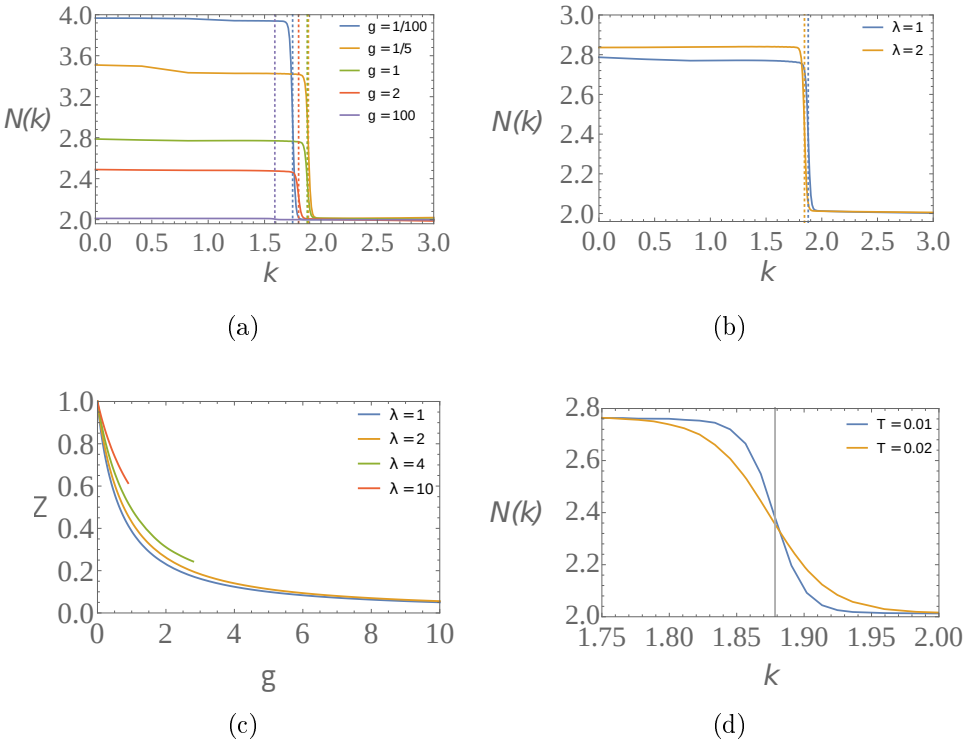


Figure 3.12: The dependence of the momentum distribution function on (a) the coupling $g$, (b) the coupling $\lambda$ and (d) the temperature, and (c) the dependence of the quasiparticle residue on $g$ and $\lambda$. In all plots the chemical potential is fixed to $\mu = 2$ and in all plots except for (d), the temperature is fixed to $T = 1/100$. In (a) $\lambda = 1$, in (b) $g = 1$ and in (d) $g = \lambda = 1$. The dotted lines in (a) and (b) denote the Fermi momenta of the corresponding curves of the same colors, as calculated from the spectral functions. In (d), the gray line denotes the location of the Fermi surface, which does not depend on temperature.

#### 3.3.2.3 Momentum distribution functions

Since our numerical calculations are performed at a small but nonzero temperature, the peaks at the Fermi surface have a small finite width. Therefore the previously obtained values of $k_F$, which is a quantity defined at zero temperature, are formally only approximately at the Fermi surface. Another

indication of the Fermi surface is found by looking for a discontinuity in the momentum distribution of the Dirac fermion, which is defined as

$$N(\mathbf{k}) = \int \mathrm{d}\omega \rho(\omega, \mathbf{k}) n_F(\omega) \tag{3.48}$$

where $n_F(\omega)$ is the Fermi distribution function. In figures 3.12a, 3.12b and 3.12d we have studied the dependence of this quantity on the parameters of our system. Here we have fixed the chemical potential to $\mu = 2$, as we expect that this will not have a large impact on the qualitative behavior besides the location of the Fermi surface. As expected, these momentum distribution functions contain a discontinuity at the Fermi surface, although the discontinuity is smoothed out by the finite temperature. We have however checked that the discontinuity becomes steeper as we decrease the temperature further, as is shown in figure 3.12d.

For small momenta, the value of $N(k)$ depends on the couplings $g$ and $\lambda$, as shown in figure 3.12a and 3.12b. The large deviation from 4 is indeed a signature of strong interactions. It indicates that there is still nontrivial spectral weight above the upper band which can for example be seen in figure 3.11a. For $g = 100$ the spread of spectral weight is so large that the discontinuity is hardly visible in the figure. In contrast, for $g = 1/100$, nearly all spectral weight is contained in the two peaks in the spectrum. Furthermore, for large momenta, $N(k)$ always approaches 2, independent of $g$ and $\lambda$. This shows that even though the spectrum contains a lot of nonzero spectral weight besides the peaks, the weight is still evenly distributed between the region above and below the gap due to the particle-hole symmetry of the undoped system. The discontinuity in the distributions is related to the quasiparticle residue $Z$, which we study in more detail shortly. Since the momentum distribution as defined in eq. (3.48) is the momentum distribution function for the entire Dirac spinor, it contains both particle and hole degrees of freedom of both chiralities. In the free theory, a discontinuity of 2 in the spectral weight corresponds to the spin degrees of freedom only, which corresponds to $Z = 1$. More generally, the quasiparticle residue is equal to one half times the discontinuity in the momentum distribution due to spin degeneracy. Figure 3.12c shows that $Z$ increases as $\lambda$ increases, and decreases for increasing $g$, in accordance with figures 3.12b and 3.12a. Moreover, the curves corresponding to $\lambda = 4$ and $\lambda = 10$ in figure 3.12c terminate at a finite value of $g$. This is because as explained in section 3.3.2.2, when $\lambda$ is

high enough there is a critical value of $g$ above which there is no Fermi surface.

The momentum distributions also slightly decrease at a momentum below $k_F$. This is for example clearly visible in figure 3.12a for the case $g = 1/5$. The reason is that the spectral functions contain a second band above the gap, as was mentioned in the previous section and can also be seen in figure 3.11a. Since this band is situated around $\omega = 0$, it yields a contribution to the momentum distribution for low momenta.

The quasiparticle residue displayed in figure 3.12c is calculated using the self-energy near the Fermi surface. For this purpose, we linearize the theory around the Fermi momentum $k_F$ and $\omega = 0$. Starting with eq. (3.37) and defining the shorthand notation

$$\omega_r \equiv \omega + \mu + g\Xi_0, \tag{3.49}$$

$$k_r \equiv k_3 - g\Xi_3, \tag{3.50}$$

$$M_r \equiv M_0 + ig\Xi_c, \tag{3.51}$$

we see that we can write the trace of the Green's function as

$$\frac{1}{2}\mathrm{Tr}\, G_R = \frac{-1}{\omega_r - \sqrt{k_r^2 + M_r^2}} - \frac{1}{\omega_r + \sqrt{k_r^2 + M_r^2}}. \tag{3.52}$$

Notice that this differs from a trivial free fermionic Green's function, since in general $\omega_r$, $k_r$ and $M_r$ are all complex functions of $\omega$, $k_3$ and all other parameters in our model. On the other hand, we obtain an effective model by linearizing the theory near the Fermi surface, i.e.,

$$\frac{1}{2}\mathrm{Tr}\, G_R = \frac{-Z}{\omega - v_F(k_3 - k_F) - i\Sigma_{\text{eff}}(\omega, k_3)}. \tag{3.53}$$

This defines the quasiparticle residue $Z$, as well as the Fermi velocity $v_F$, which are both real and positive. Moreover, it defines the effective self-energy $\Sigma_{\text{eff}}$ which is a real function of $\omega$ and $k_3$ that vanishes at the Fermi surface at zero frequency. We can compute expressions for these quantities by comparing eq. (3.53) to eq. (3.52). To do so we first note that the latter is dominated by the first term, since this contains a pole exactly at the Fermi

surface.[12] Neglecting the second term then yields

$$\begin{aligned} Z^{-1} &\approx -\partial_\omega \mathrm{Re}\left[\left(\frac{1}{2}\mathrm{Tr}\, G_R(\omega, k_F)\right)^{-1}\right]\Big|_{\omega=0} \\ &\approx 1 + \partial_\omega \mathrm{Re}\Big[g\Xi_0(\omega, k_F) \\ &\qquad - \sqrt{\big(k_F - g\Xi_3(\omega, k_F)\big)^2 + \big(M_0 + ig\Xi_c(\omega, k_F)\big)^2}\Big]\Big|_{\omega=0} . \end{aligned} \tag{3.54}$$

This expression allows us to calculate the quasiparticle residue by calculating the self-energy near the Fermi surface and was used to create figure 3.12c. Note that for $M_0 = \Xi_c = 0$ this reduces to the result in section 4.2.1. in Ref. [62]. Moreover, note that the evaluation at $k_F$ gives an additional implicit dependence on $g$ and $\lambda$. However, since $k_F$ converges for large $g$, we can still see from this expression that then $Z \propto 1/g$, as we also observe in the figure. Deriving a similar expression for the Fermi velocity yields

$$\begin{aligned} v_F &\approx 2Z\, \partial_{k_3} \mathrm{Re}\left[\big(\mathrm{Tr}\, G_R(0, k_3)\big)^{-1}\right]\Big|_{k_3=k_F} \\ &\approx -Z\partial_{k_3} \mathrm{Re}\Big[g\Xi_0(0, k_3) \\ &\qquad - \sqrt{\big(k_3 - g\Xi_3(0, k_3)\big)^2 + \big(M_0 + ig\Xi_c(0, k_3)\big)^2}\Big]\Big|_{k_3=k_F} . \end{aligned} \tag{3.55}$$

Finally, we have that the effective self-energy is given by

$$\begin{aligned} \Sigma_{\text{eff}} &\approx 2Z\mathrm{Im}\left[(\mathrm{Tr}\, G_R)^{-1}\right] \\ &\approx -Z\mathrm{Im}\left[g\Xi_0 - \sqrt{\big(k_3 - g\Xi_3\big)^2 + \big(M_0 + ig\Xi_c\big)^2}\right] . \end{aligned} \tag{3.56}$$

We have plotted this effective self-energy in figure 3.13a. As expected it vanishes at zero frequency,[13] which is related to the fact at the Fermi surface

[12] For $\mu < 0$ the second term would dominate.

[13] In our numerics, it does not vanish exactly. We have however checked that this is due to nonzero temperature. As we lower the temperature, the dependence $\Sigma_{\text{eff}}(0, k_F) \propto T^{3/2}$ seems to approximate our results.

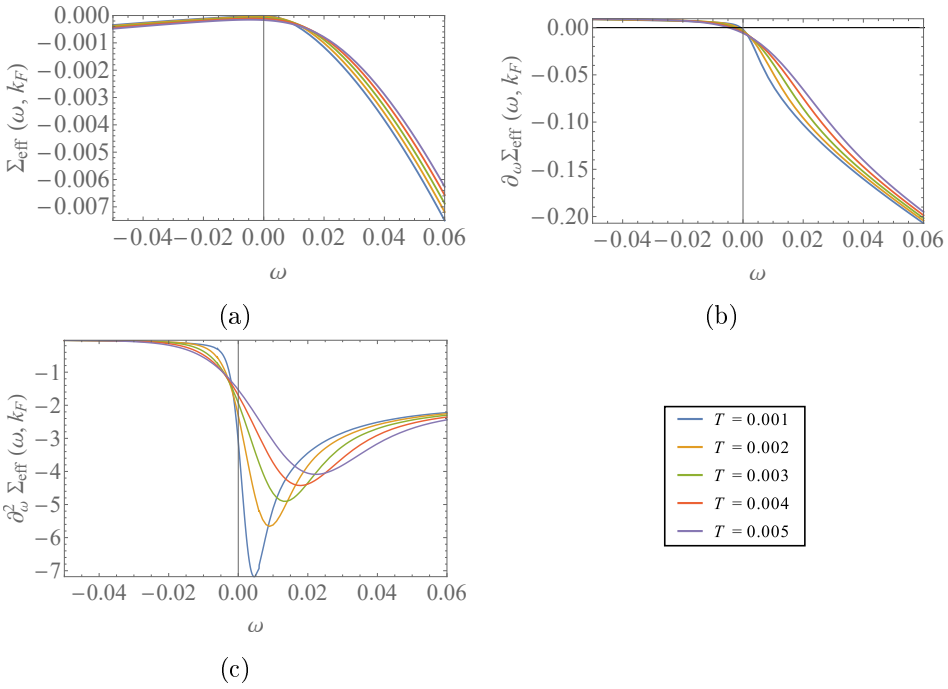


Figure 3.13: (a) The effective self-energy $\Sigma_{\text{eff}}$ at the Fermi momentum, and its (b) first and (c) second derivatives. The legend in the lower right corner holds for all figures. In all graphs, $\mu = 2$, $g = 1$ and $\lambda = 1$.

there is a peak with an infinite lifetime $\tau = -2/\Sigma_{\text{eff}}$. This is indeed visible in figure 3.11a. At nonzero $\omega$, the width associated with the peak increases and so the lifetime becomes shorter. Of interest is the leading order frequency dependence of the self-energy $\Sigma_{\text{eff}}$. If the system behaves as a Fermi liquid, $\Sigma_{\text{eff}}$ should go to zero faster than $\omega$. Figure 3.13b shows that this is indeed the case, since the derivative of $\Sigma_{\text{eff}}$ vanishes at $\omega = 0$. Therefore the system indeed behaves like a Fermi liquid. In figure 3.13c we have also plotted the second derivative of $\Sigma_{\text{eff}}(\omega, k_F)$ for low temperatures. At first sight, these all seem to converge to a finite value as $\omega \to 0$, so that we could conclude that the self-energy follows $\Sigma_{\text{eff}} \propto \omega^2$ for small $\omega$. However, upon closer inspection, the coefficient of $\omega^2$ does not appear to converge as we lower the temperature. This convergence is necessary since we are studying the behavior near the Fermi surface, which is defined at zero temperature. The

problem is that by determining the second derivative at zero frequency, we are inspecting a region where $\omega \lesssim T$, which does not correspond to the low-temperature physics. We do observe that the second derivative converges to a finite value for $\omega \approx 0.05$. Here, $T \ll \omega$, but $\omega$ is small compared to the other scales of the system, i.e., the gap and the chemical potential. We also see such a convergence for negative frequencies, but the convergence is to a different value. Although it is numerically difficult to lower the temperature even further, we believe that in the zero-temperature limit, the function in figure 3.13c converges to a finite value as $\omega \to 0$, which is dependent on whether the limit is taken from above or below.

Although it appears difficult to extract the exact frequency dependence of the effective self-energy at the Fermi surface, it is at least clear that it converges to zero faster than linearly and the system is a Fermi liquid. Moreover, since the second derivative clearly does not converge to 0, we can also conclude $\Sigma_{\text{eff}}(\omega, k_F)$ does not converge exponentially. We have checked that this does not change in the holographic limit of large $g$. This is in contrast to what is found in the models in [62, 91, 92] where fermionic systems are studied using backgrounds with a dynamical scaling exponent $z$ that is emergent in the IR geometry. There, the self-energy behaves as

$$\Sigma_{\text{eff}} \propto \exp\left(-\left(\frac{k_F^z}{\omega}\right)^{\frac{1}{z-1}}\right). \tag{3.57}$$

Apparently, our model does not contain such an exponential behavior, as can also be checked by studying the IR geometry of our model in the zero-temperature limit, which is similar to the one in section 5.2 in Ref. [55].[14]

## 3.4 Conclusions and discussion

In this work we provided a framework to study the dynamics of massive Dirac fermions using holographic and semiholographic models. We find that a gap is induced in the fermionic spectra by coupling two probe fermions in the bulk theory through a Yukawa coupling with the scalar field that provides the mass deformation. Moreover, by extending to a semiholographic model we encounter a quantum critical point at which the effective mass of the fermion

[14] Note however that this reference contains the geometry for $d = 3$.

vanishes. When turning on doping, we have seen that the Yukawa coupling can be used as a parameter that triggers a quantum phase transition between a state with a Fermi surface and a state without one. Studying the momentum distributions near the Fermi surfaces using the semiholographic Green's functions revealed that the described systems show Fermi-liquid behavior. In particular, the effective self-energy at the Fermi momentum converges to zero faster than linearly in frequency, as is expected from Pauli blocking.

An aspect that requires further research is the conductivity in the model. In this work, we have only seen that the CFT conductivity does not behave like an insulator despite the introduced mass deformation. It would be interesting to study if the fermionic contribution to the conductivity does behave like an insulator as expected. To this end we should first use the dressed semiholographic fermionic Green's functions to calculate the current-current correlation function from the one-loop diagram as in Refs. [78, 86]. The next step would then be to also include the vertex corrections.

The principal result of this work is to provide a framework that allows us to compute fermionic spectral functions that are relevant in the study of strongly coupled condensed matter. In particular, using the method described here allows us to include the mass of the fermions in condensed-matter systems. As mentioned in the introduction, this can either be a real particle mass or an effective mass or gap in a Dirac material. The viewpoint taken in this work is the latter, where the Dirac theory is used as an effective description. Basically, this means that the speed $c$ that is set to unity in this paper corresponds to the Fermi velocity of the free massless Dirac theory. From the other point of view, we use Dirac theory to describe actual fermionic particles, and the speed $c$ corresponds to the speed of light. In this case the newly introduced energy scale $mc^2$, where $m$ is the mass of the fermion in the condensed-matter system under study, allows us to research nonrelativistic physics by resorting to the appropriate regime in which the other scales such as $k_BT$, $\hbar\omega$ and $\mu$ are small compared to $mc^2$. It would be interesting to see if we can use this approach to for example study ultracold Fermi gases at unitarity. Besides this, we can of course study a plethora of strongly coupled condensed-matter physics by adding additional ingredients in the bulk theory, such as chiral-symmetry breaking terms as was done in Refs. [41, 77, 79].

# 3.A Conventions

In this appendix we list our conventions. We firstly specify the dimensionless units used throughout the paper, and subsequently give our conventions regarding the Dirac theory.

## 3.A.1 Units

The action for the gravitational background eq. (3.1) reads in SI units

$$S = \int \mathrm{d}^5x\sqrt{-g}\left(\frac{c^3}{16\pi G}(R-2\Lambda) - \frac{1}{4\mu_0 c}F^2 - \left((\partial\phi)^2 + \frac{m_\phi^2 c^2}{\hbar^2}\phi^2\right)\right). \tag{3.58}$$

Here $G$ and $\mu_0$ are Newton's constant and the vacuum permeability respectively in 4 spatial dimensions, and $\Lambda < 0$ is the cosmological constant. The components of the metric $g_{\mu\nu}$ are dimensionless. Defining the anti-de Sitter radius as $L^2 = 6/(-\Lambda)$, the dimensionless units in this paper are obtained by scaling length scales by $L$, so that $\Lambda = -6$. Moreover, we put Boltzmann's constant $k_B = 1$. Consequently, all energy scales, such as $k_B T$, $m_\phi c^2$ and $M_0 c^2$, are in units of $\hbar c/L$. The dimensionless fields are obtained as follows:

$$\tilde{A}_{\tilde{t}} = \sqrt{\frac{16\pi G}{\mu_0 c^6}}A_t, \tag{3.59}$$

$$\tilde{\phi} = \sqrt{\frac{16\pi G}{c^3}}\phi. \tag{3.60}$$

Here the left-hand sides are the dimensionless fields used throughout the paper, where we omitted the tildes.

The Dirac action in eq. (3.11) in SI units reads

$$S = ig_f\int \mathrm{d}^5x\sqrt{-g}\bar{\psi}\left(\not{D} - \frac{Mc}{\hbar}\right)\psi + ig_f\int \mathrm{d}^4x\sqrt{-h}\bar{\psi}_R\psi_L. \tag{3.61}$$

Taking $g_f$ dimensionless, the Dirac field $\psi$ has the dimension of $\sqrt{\hbar}/L^2$. The dimensionless Dirac field can be defined by extracting this factor from the field. Alternatively, there is always an undetermined dimensionless constant

$\hbar c^3/16\pi GL^3$ which can be included in the definition. However, this is equivalent to a redefinition of $g_f$. Furthermore, the dimensionless charge $\tilde{q}$ that resides in the covariant derivative is given by

$$\tilde{q} = \sqrt{\frac{\mu_0 c^6}{16\pi G}} \frac{L}{\hbar c} q. \tag{3.62}$$

We remind the reader that the dimensionless quantities defined in this appendix are dimensionless in SI units, but can still have a nonzero scaling dimension.

## 3.A.2 Dirac theory

Firstly, we define Dirac's gamma matrices in flat spacetime as follows:

$$\Gamma^{\underline{\mu}} = \gamma^{\underline{\mu}} = \begin{pmatrix} 0 & \bar{\sigma}^\mu \\ \sigma^\mu & 0 \end{pmatrix} \qquad \text{for } \mu \neq r, \tag{3.63}$$

$$\Gamma^{\underline{r}} = \gamma^{\underline{5}} = \begin{pmatrix} \mathbb{I}_2 & 0 \\ 0 & -\mathbb{I}_2 \end{pmatrix} = i\gamma^{\underline{0}}\gamma^{\underline{1}}\gamma^{\underline{2}}\gamma^{\underline{3}}. \tag{3.64}$$

Here $\Gamma^{\underline{a}}$ are the gamma matrices defined in the $4+1$ spacetime of the bulk, while $\gamma^{\underline{a}}$ are the usual gamma matrices in $3+1$ dimensions. Notice as well that these indices, such as $\underline{a}$, are underlined, meaning that these are tensors defined in flat spacetime, i.e., $g^{\underline{ab}} = \eta^{\underline{ab}}$. Moreover, $\sigma = (\mathbb{I}_2, \sigma^i)$ and $\bar{\sigma} = (-\mathbb{I}_2, \sigma^i)$ with $\sigma^i$ the Pauli matrices.

Conjugate spinors are defined as

$$\bar{\psi} = \psi^\dagger \Gamma^{\underline{0}}. \tag{3.65}$$

The gamma matrices in a curved background are defined using the vielbeins:

$$\Gamma^\mu = e^\mu_{\underline{a}} \Gamma^{\underline{a}}. \tag{3.66}$$

The vielbeins satisfy $g_{\mu\nu} = e^{\underline{a}}_\mu e^{\underline{b}}_\nu \eta_{\underline{ab}}$ and the inverse vielbeins $e^\mu_{\underline{a}} e^{\underline{a}}_\nu = \delta^\mu_\nu$ and $e^\mu_{\underline{a}} e^{\underline{b}}_\mu = \delta^{\underline{b}}_{\underline{a}}$. Computing these for the metric in eq. (3.2) gives

$$e^{0}_{\underline{0}} = \sqrt{\frac{e^{\chi(r)}}{f(r)}}, \tag{3.67}$$

$$e^{r}_{\underline{r}} = \sqrt{f(r)}, \tag{3.68}$$

$$e^{i}_{\underline{i}} = \frac{1}{r}. \tag{3.69}$$

The slash is defined by

$$\not{X} = \Gamma^{\mu} X_{\mu}. \tag{3.70}$$

Finally, the Dirac action contains the covariant derivative $\not{D} = \not{\nabla} - iq\not{A}$. Here the spinor covariant derivative $\nabla_{\mu}$ is defined as

$$\nabla_{\mu}\psi = \partial_{\mu}\psi + \Omega_{\mu}\psi \tag{3.71}$$

where $\Omega_{\mu}$ is given by

$$\Omega_{\mu} = \frac{1}{8}\omega_{\mu\underline{ab}}[\Gamma^{\underline{a}}, \Gamma^{\underline{b}}] \tag{3.72}$$

with $\omega_{\mu\underline{ab}}$ the spin connection

$$\omega^{\underline{a}}_{\mu\underline{b}} = e^{\underline{a}}_{\nu} e^{\lambda}_{\underline{b}} \Gamma^{\nu}_{\mu\lambda} - e^{\lambda}_{\underline{b}} \partial_{\mu} e^{\underline{a}}_{\lambda}. \tag{3.73}$$

For the metric in eq. (3.2) the only nonvanishing components of the spin connection are $\omega_{t\underline{tr}} = -\omega_{t\underline{rt}}$ and $\omega_{i\underline{ir}} = -\omega_{i\underline{ri}}$. Using this, one can show that the spinor covariant derivative can be written as

$$\not{\nabla}\psi = \not{\partial}\psi + \Gamma^{\underline{r}} F(r)\psi \tag{3.74}$$

where $F$ is a function depending on the radial coordinate only. Defining

$$p(r) = \exp\left(-\int^{r} \mathrm{d}r' F(r')\right), \tag{3.75}$$

we have that

$$\not{\nabla}\,(p\psi) = p\not{\partial}\psi. \tag{3.76}$$

This demonstrates that rescaling both $\psi^{(1)} \to p\psi^{(1)}$ and $\psi^{(2)} \to p\psi^{(2)}$ in eqs. (3.16) and (3.17) gets rid of the spin connection terms in the Dirac equations. Moreover, this rescaling does not affect the matrix $\Xi$ defined in eq. (3.22).

## 3.B Symmetries

In certain cases we can reduce the amount of equations we need to solve by using additional symmetries. From the equations in (3.29) and the imposed initial conditions we can derive that

$$\Xi_{\pm}(\tilde{\omega}, k_3) = \Xi_{\mp}(\tilde{\omega}, -k_3), \tag{3.77}$$
$$\Xi_c(\tilde{\omega}, k_3) = \Xi_c(\tilde{\omega}, -k_3), \tag{3.78}$$
$$\Xi_{\pm}(\tilde{\omega}, k_3) = -\Xi^*_{\mp}(-\tilde{\omega}, k_3), \tag{3.79}$$
$$\Xi_c(\tilde{\omega}, k_3) = -\Xi^*_c(-\tilde{\omega}, k_3). \tag{3.80}$$

The first two symmetries correspond to parity symmetry, whereas the last two represent time-reversal symmetry. From these symmetries it follows that we can solve the system for $k_3 \geq 0$ and use eq. (3.77) and eq. (3.78) to obtain the results for $k_3 < 0$. Moreover, when $\mu = 0$, we only need to solve for $\omega \geq 0$ according to eq. (3.79) and eq. (3.80), which then represent particle-hole symmetry.

Also, the equations in (3.29) as well as the initial conditions are invariant under sending both $\lambda \to -\lambda$ and $\Xi_c \to -\Xi_c$. This symmetry allows us to obtain solutions for $\lambda < 0$ from solutions with $\lambda > 0$. Furthermore, multiplying the matrix equation between the brackets in (3.27) from both the left and the right by $\Xi^{-1}$ reveals that the equations are also invariant under sending $M \to -M$, $\lambda \to -\lambda$ and $\Xi \to \Xi^{-1}$. Consequently, solutions for $M < 0$ can be obtained from solutions with $M > 0$. Finally, solutions for $\mu < 0$ can be obtained from solutions with $\mu > 0$ by exploiting the symmetries in eq. (3.79) and eq. (3.80).

The symmetries in eqs. (3.77)-(3.80) show that for $k_3 = 0$ we have $\Xi_3 = 0$, and that for $\tilde{k}_\mu = 0$, $\Xi_\pm$ is real and $\Xi_c$ is imaginary. This demonstrates that the constants $Z_0$ and $M_{\text{eff}}$ defined in eq. (3.44) and eq. (3.45) respectively are real.

## 3.C RG equations

Throughout the paper, we have fixed the ratio of the scalar source $\phi_s$ and the bare mass $M_0$ originating from the UV action eq. (3.31) to $\alpha \equiv M_0/\phi_s = \sqrt[4]{\pi^2/3}$. Here we present an argument for choosing this specific value. It is important to realize that we could in principle consider models in which

this ratio is a free parameter, so that independent from the argument made here, our semiholographic results can also be seen as a specific case of such models. Moreover, this value is not relevant for our holographic results.

For a mass $m_\phi^2 = -3$, the asymptotic equations of motion in eqs. (5.4), (5.5), (5.6) and (5.7) give

$$\phi = \phi_s r^{-1} + \phi_v r^{-3} - \frac{\phi_s^3}{6} r^{-3} \log r \dots . \tag{3.81}$$

Under a rescaling $r \to \lambda r$ we then get

$$\phi \to \phi_s(\lambda)\lambda^{-1} r^{-1} + \phi_v(\lambda)\lambda^{-3} r^{-3} - \frac{\phi_s(\lambda)^3}{6}\lambda^{-3} r^{-3} (\log r + \log \lambda) \dots . \tag{3.82}$$

As $\phi$ is invariant under this rescaling we get from comparing eq. (3.81) and eq. (5.31) that

$$\phi_s(\lambda) = \phi_s \lambda, \tag{3.83}$$

$$\phi_v(\lambda) = \phi_v \lambda^3 + \frac{\phi_s^3}{6}\lambda^3 \log \lambda. \tag{3.84}$$

This yields the following RG equations for the coefficients $\phi_{s,v}$:

$$\lambda \frac{\mathrm{d}\phi_s(\lambda)}{\mathrm{d}\lambda} = \phi_s(\lambda), \tag{3.85}$$

$$\lambda \frac{\mathrm{d}\phi_v(\lambda)}{\mathrm{d}\lambda} = 3\phi_v(\lambda) + \frac{\phi_s(\lambda)^3}{6}. \tag{3.86}$$

Note that the term with the logarithm generates the nontrivial part of the RG equation in eq. (5.35).

On the other hand, the two-point function found from semiholography is

$$\begin{aligned} \left\langle i\bar{\Psi}\Psi \right\rangle &= \mathrm{Tr} \int \frac{\mathrm{d}^4 k_E}{(2\pi)^4} \frac{1}{-i\not{k}_E + M_0 - i\tilde{\Sigma}} \\ &= \mathrm{Tr} \int \frac{\mathrm{d}^4 k_E}{(2\pi)^4} \frac{1}{k_E^2 + M_0^2 + \tilde{\Sigma}^2 - \{\not{k}_E, \tilde{\Sigma}\}} \left( i\not{k}_E + M_0 - i\tilde{\Sigma} \right), \end{aligned} \tag{3.87}$$

where we used the Euclidean momentum with $k_E^2 = |\mathbf{k}|^2 + k_4^2$ and $k_4 = i\omega$ and where $\{.,.\}$ denotes the anticommutator. Note that the self-energy $\tilde{\Sigma}$ here differs from the self-energy $\Sigma$ defined in eq. (3.36) by a factor of $\Gamma^{\underline{0}}$, since

we are calculating $\langle\bar{\Psi}\Psi\rangle$ rather than $\langle\Psi^\dagger\Psi\rangle$. However, for large momenta its components are also proportional to $k^{2M}$.

Our goal is now to derive an RG equation for $\langle i\bar{\Psi}\Psi\rangle$. To this end, we integrate over a high-momentum shell for which $|k_E| \in (\Lambda e^{-l}, \Lambda)$ where $\Lambda$ is a UV cut-off and $l > 0$. We then look for the logarithmic UV divergence, which should yield the term in the RG equation that can be compared to the nontrivial term in eq. (5.35). For the high momenta in the shell, the integrand in eq. (3.87) can be expanded as

$$\langle i\bar{\Psi}\Psi\rangle_\Lambda = \mathrm{Tr}\int_\Lambda \frac{\mathrm{d}^4k_E}{(2\pi)^4}\frac{1}{k_E^2}\left(1-\frac{M_0^2+\tilde{\Sigma}^2-\{\not{k}_E,\tilde{\Sigma}\}}{k_E^2}\right)\left(i\not{k}_E+M_0-i\tilde{\Sigma}\right) + \dots \tag{3.88}$$

where the dots denote the integration over lower momenta and the second integral is over the shell. Now it is clear that the logarithmic divergence resides in the term[15] proportional to $M_0^3/k_E^4$. To evaluate this term, we use $\mathrm{d}^4k_E = 2\pi^2 k_E^3 \mathrm{d}k_E$ to get

$$\langle i\bar{\Psi}\Psi\rangle_\Lambda = \dots - \frac{M_0^3}{2\pi^2}\int_{\Lambda e^{-l}}^{\Lambda}\frac{\mathrm{d}k_E}{k_E} = \dots - \frac{M_0^3 l}{2\pi^2}\,, \tag{3.89}$$

so that

$$\frac{\mathrm{d}\langle i\bar{\Psi}\Psi\rangle}{\mathrm{d}l} = \dots - \frac{M_0^3}{2\pi^2}. \tag{3.90}$$

Expressing this in terms of $\alpha$ as defined in the beginning of this appendix, and identifying $\phi_v = -\langle i\bar{\Psi}\Psi\rangle/\alpha$,[16] we obtain

$$\frac{\mathrm{d}\phi_v}{\mathrm{d}l} = \dots + \frac{\alpha^4\phi_s^3}{2\pi^2}\,. \tag{3.91}$$

Comparing this with eq. (5.35) then yields $\alpha^4 = \pi^2/3$.

[15] Here we neglect the subtle case $M = 0$.

[16] This follows from comparing the on-shell Klein-Gordon action to the mass deformation.

# 4 Nonrelativistic fermions with holographic interactions and the unitary Fermi gas

## 4.1 Introduction

Our understanding of ultracold Fermi gases has significantly progressed over the past decade, due to the fact that the $s$-wave scattering length, which is the relevant measure for the strength of the interactions in these systems, can be conveniently engineered by tuning a magnetic field near a so-called Feshbach resonance [21, 58]. This allows for an accurate experimental analysis of ultracold gases in both the weakly and strongly coupled regime [24–29]. A particularly interesting situation occurs exactly at resonance, where the external magnetic field is such that the scattering length diverges. At this point collisions between the atoms are unitarity limited and the system becomes almost scale invariant, in the sense that the only length scale at zero temperature is the average interatomic distance that is set by the atomic density and diverges at zero density. Consequently, the thermodynamic properties of the Fermi gas become universal at unitarity [30].

Being strongly coupled, close to scale invariant and experimentally accessible, these ultracold gases at unitarity present a benchmark problem for the application of the holographic AdS/CFT correspondence, which aims to describe a (possibly deformed) conformal field theory (CFT) as a boundary property of a dual theory in a curved spacetime with one more spatial dimension [93]. This correspondence was discovered within string theory [6] and for condensed-matter physics has especially had some successes in the application to emergent relativistic systems such as graphene [71, 94] and Weyl or Dirac semimetals [41, 56, 62, 77, 79, 82, 86, 95]. A common way to deal with nonrelativistic systems in holography is to use instead of an anti-de Sitter (AdS) spacetime background a so-called Lifshitz background [67–70, 96] as a gravitational dual with a dynamical exponent $z = 2$. However, the fermionic spectra obtained in this way are generally particle-hole symmetric and without a mass gap. Hence for the description of an ultracold

gas of massive atoms, a different approach is needed. The purpose of this Letter is to provide this alternative approach to nonrelativistic holography, which allows us to compute nonrelativistic single-particle spectra that can in principle be compared with experiments. Our method uses as its starting point results for the dynamics of Dirac fermions from holography [2], from which we can also obtain single-particle spectra with a mass gap by introducing a mass deformation in the CFT. The introduction of the mass gap allows us to consider the nonrelativistic limit of such spectra, where this mass scale, which contains the speed of light $c$, is large compared to all the other energy scales in the problem. Our most important finding below is that we obtain a data collapse for the spectral functions in the limit $c \to \infty$, i.e., the spectral functions are universal after an appropriate scaling with the chemical potential.

An important advantage of our procedure is that it allows us to directly compare results obtained from a holographic model with experimental data. Therefore, we also extensively discuss the application of our method to ultracold Fermi gases at unitarity. In particular, we determine the equation of state from the single-particle spectra, i.e., the density as a function of the chemical potential and temperature, which is shown in Fig. 4.1 and from which all thermodynamic functions follow. The equation of state can be directly compared with results from experiments [34, 98–100] and from other theoretical models that are based on for example quantum Monte-Carlo methods [35, 36], the Luttinger-Ward formalism [101], Wilsonian renormalization-group methods [37], or more recently the complex Langevin model [97]. Of course, a quantitative comparison requires fine-tuning of the model parameters and possibly also examining different gravitational dual theories. This is beyond the scope of the present paper, in which we primarily focus on the method to obtain universal nonrelativistic spectra from holography. Therefore, the main purpose of the comparison to the unitary Fermi gas is to show that our spectra are able to reproduce many of its qualitative features.

## 4.2 Holographic interactions

To explain most clearly the physical content of our approach, we consider a relativistic Dirac fermion $\Psi$ with bare mass $M_0$ and chemical potential $\mu_0$

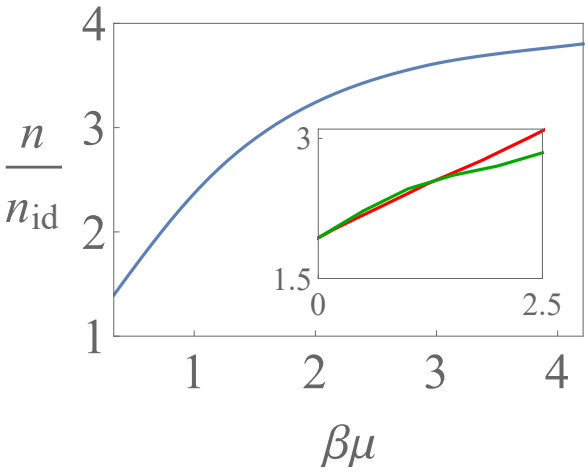


Figure 4.1: The universal equation of state obtained for our nonrelativistic fermions with holographic interactions. The atomic density $n$ divided by the ideal Fermi gas density $n_{\mathrm{id}}$ is shown as a function of the chemical potential times the inverse thermal energy $\beta\mu \equiv \mu/k_B T$. For comparison the inset shows the experimental results of Ref. [34] (red) and the theoretical results from Ref. [97] (green) obtained by the complex Langevin method. Note that our construction of the holographic interactions depends on four dimensionless model parameters that are introduced in the text below and that are not yet fine-tuned to the experiments as these contain effects of the inhomogeneity of the harmonically trapped gas and of the phase transition to the superfluid state. The specific values used are here the same as in Fig. 4.3.

that is linearly coupled to a strongly interacting CFT through a fermionic operator $\mathcal{O}$. Referring to the supplemental material for our conventions in this section on the units (mostly $\hbar = c = 1$) and on the Dirac theory in flat and curved spacetimes [1], the corresponding grand-canonical action is

$$S = \int \frac{\mathrm{d}^4 k}{(2\pi)^4} \left\{ \Psi^\dagger \gamma^0 \left( -\not{K} - i M_0 \right) \Psi + g \Psi^\dagger \mathcal{O} + g \mathcal{O}^\dagger \Psi \right\} + S_{\mathrm{CFT}}, \qquad (4.1)$$

with $k_\mu = (-\omega, \mathbf{k})$, $\not{K} = \gamma^\mu K_\mu$, $\gamma^\mu$ the gamma matrices, $K_\mu = (-\omega - \mu_0, \mathbf{k})$, $g$ a coupling constant and $S_{\mathrm{CFT}}$ the action of the deformed CFT containing

[1] See section 4.C for conventions on units and Dirac theory.

$\mathcal{O}$. To make a connection with condensed-matter physics, we think of the CFT as being formed out of collective variables of the single fermion $\Psi$. From this perspective, the operator $\mathcal{O}$ is then a composite operator containing $\Psi$. We remark that we employ holography in the spirit of a bottom-up approach, in which we only know some global (universal) properties of the action of the CFT. However, the exact microscopic content of the CFT is unknown, so that it is not possible to give an explicit expression for $S_{\rm CFT}$. Nonetheless, we discuss some possible microscopic connections to the unitary Fermi gas at the end of the paper. The CFTs described by holographic models contain a large number of degrees of freedom $N$ [6], which implies that upon integrating out the CFT we can write the retarded Green's function for $\Psi$ as

$$G_R^{-1}(\omega,\mathbf{k}) = -\gamma^0\left(\not{K} + iM_0\right) - \Sigma(\omega,\mathbf{k}), \tag{4.2}$$

with $\Sigma(\omega,\mathbf{k}) \equiv g^2 G_{\mathcal{O}}(\omega,\mathbf{k})$ the self-energy matrix for $\Psi$ that due to the implicit large-$N$ limit only involves the two-point function $G_{\mathcal{O}}$ of $\mathcal{O}$. The latter can be directly obtained from the dictionary of the AdS/CFT correspondence.

Technically, we obtain the above Green's function $G_R$ from a holographic dynamical-source model [62]. The calculation of the Green's function is then a two-step process. The first step is to find the gravitational dual of the CFT, also known as the bulk background, which consists of a so-called asymptotically anti-de Sitter spacetime with an additional spatial coordinate $r$. Moreover, to have a nonzero temperature $T$ and chemical potential $\mu_0$ in the CFT, we need to have a black-hole horizon at $r = r_+$ and a $U(1)$ gauge field $A = A_t \mathrm{d}t$ in the bulk [56]. Finally, consistent with our above interpretation of $\mathcal{O}$, we need to introduce a mass deformation in the CFT. This we achieve by adding also a real scalar field $\phi$ to the gravity theory [41]. The gravitational background is then found by simultaneously solving the Einstein equations, the Maxwell equations and the Klein-Gordon equation. Numerically, this is achieved by integrating the coupled equations of motion for $A_t(r)$, $\phi(r)$ and the metric $g_{MN}(r)$, or equivalently the vielbeins $e_N^M(r)$ [2], from the horizon at $r_+$ to the boundary at $r = \infty$, where the CFT lives [3]. Here we use capital

[2] In this chapter we use the convention that the lower index of the vielbein corresponds to the flat index.

[3] See section 4.A for the actions and corresponding equations of motions used in this section.

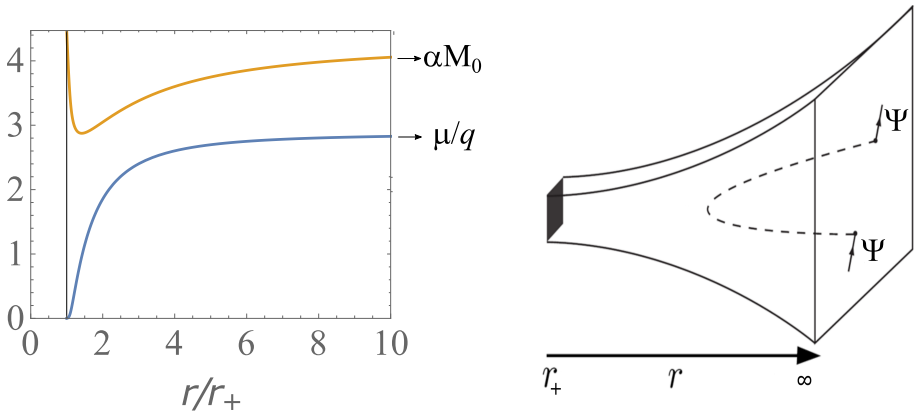


(a) (b)

Figure 4.2: (a) A typical bulk solution of the gauge field $A_t$ (blue) and the scalar field $r\phi$ (yellow). The latter is multiplied by $r$ so that its value at the boundary at $r = \infty$ gives the mass $M_0$, up to the constant $\alpha = \sqrt[4]{3/\pi^2}$ that is derived in Ref. [2]. From the value of $A_t$ at the boundary we can read off the chemical potential divided by the charge $q$. (b) The Witten diagram from which the self-energy for $\Psi$ follows. The dashed line gives the propagator $G_{\mathcal{O}}$, which follows from the propagation of the Dirac fermions in the curved bulk spacetime.

Roman indices in the five-dimensional bulk spacetime, which, as opposed to the Greek indices, include the radial $r$-direction. From the boundary values of the solution we can then read off the chemical potential and the mass $M_0$, as illustrated in Fig. 4.2a, whereas the temperature is equal to the Hawking temperature that follows from the behavior of the metric at the horizon.

The second step is then to find the two-point function $G_{\mathcal{O}}$, that according to the holographic dictionary follows by having two Dirac spinors, which together contain the degrees of freedom of $\Psi$ and $\mathcal{O}$, propagate on the gravitational background found in the first step, as illustrated in Fig. 4.2b. These spinors have bulk charge $q$ under the $U(1)$ gauge field and bulk masses $M$ and $-M$, respectively. Furthermore, they are coupled to the scalar field $\phi$ by a Yukawa coupling with strength $\lambda$, which is necessary to provide a coupling between the chiral components of the boundary spinor $\Psi$ [2]. From the associated equations of motion for these bulk fermions, we can then derive a differential equation for the $4 \times 4$ matrix $\Xi$, which is related to $G_{\mathcal{O}}$ by

$G_{\mathcal{O}}(\omega, \mathbf{k}) = -\lim_{r\to\infty} r^{2M}\gamma^0\Xi(r, \omega, \mathbf{k})$. This equation reads

$$-(e_r^r\partial_r + 2M)\Xi + i\left(i\not{K} + \lambda\phi\right) - i\Xi\left(i\not{K} - \lambda\phi\right)\Xi = 0, \tag{4.3}$$

where now $K_\mu = (-\omega - qA_t, \mathbf{k})$ and $\not{K} = \gamma^\nu e_\nu^\mu K_\mu$. It is supplemented with the initial condition $\Xi(r_+) = i\gamma^0$, corresponding to purely infalling conditions at the horizon. Having solved eq. (4.3), we find the spectral function $\rho(\omega, \mathbf{k}) = \mathrm{Im}[\mathrm{Tr}\, G_R(\omega, \mathbf{k})]/\pi$ of $\Psi$ which depends on the ratios $k_BT/M_0c^2$ and $\mu_0/M_0c^2$ obtained from the gravitational background, and additionally on the dimensionless parameters $q$, $M$, $\lambda$ and $g$ involved in our construction of the holographic interactions. We comment on the physical significance of these model parameters at the end of the paper.

## 4.3 Nonrelativistic limit

The above (semi)holographic model yields relativistic spectral functions that obey the frequency sum rule $\int d\omega\rho(\omega, \mathbf{k}) = 4$ [81] and thus contain both particle and antiparticle peaks, separated by a gap proportional to $M_0c^2$ [2]. The introduction of this mass scale allows us to inspect the nonrelativistic limit by considering temperatures and chemical potentials that are small compared to this scale. For this, however, we first need a suitable definition of the nonrelativistic chemical potential $\mu$, which differs from $\mu_0$ defined above as in the limit $c \to \infty$ we want to measure the chemical potential with respect to the bottom of the particle band as illustrated in Fig. 4.3a. Hence, when $\mu = T = 0$ we expect a delta peak at $(\omega, \mathbf{k}) = (0, \mathbf{0})$. Defining $\mu_0^*$ as the value of $\mu_0$ at which this occurs, the nonrelativistic chemical potential $\mu$ is then proportional to $\mu_0 - \mu_0^*$.

Moreover, for a genuine nonrelativistic spectrum, we should observe that in the regime where $\hbar\omega$ and $\hbar ck$ are small compared to $M_0c^2$, the spectral functions no longer depend on the energy scale $M_0c^2$. Another way of saying this is that the spectra should only depend on the ratio $\beta\mu$ rather than on $k_BT/M_0c^2$ and $\mu/M_0c^2$ separately. An obvious strategy to find such spectra is therefore to analyze spectral functions for several small values of $T$ and $\mu$, keeping the ratio $\beta\mu$ fixed. Our numerical data shown in Fig. 4.3b reveals that we can indeed find a data collapse in this limit, provided that we use the nonrelativistic chemical potential $\mu = Z(\mu_0 - \mu_0^*)$, with the wavefunction renormalization factor $Z$ defined by $1/Z = -2\partial_\omega \mathrm{Re}\left[\mathrm{Tr}\, G_R(\omega, \mathbf{0})\right]^{-1}\big|_{\omega=\omega_0}$

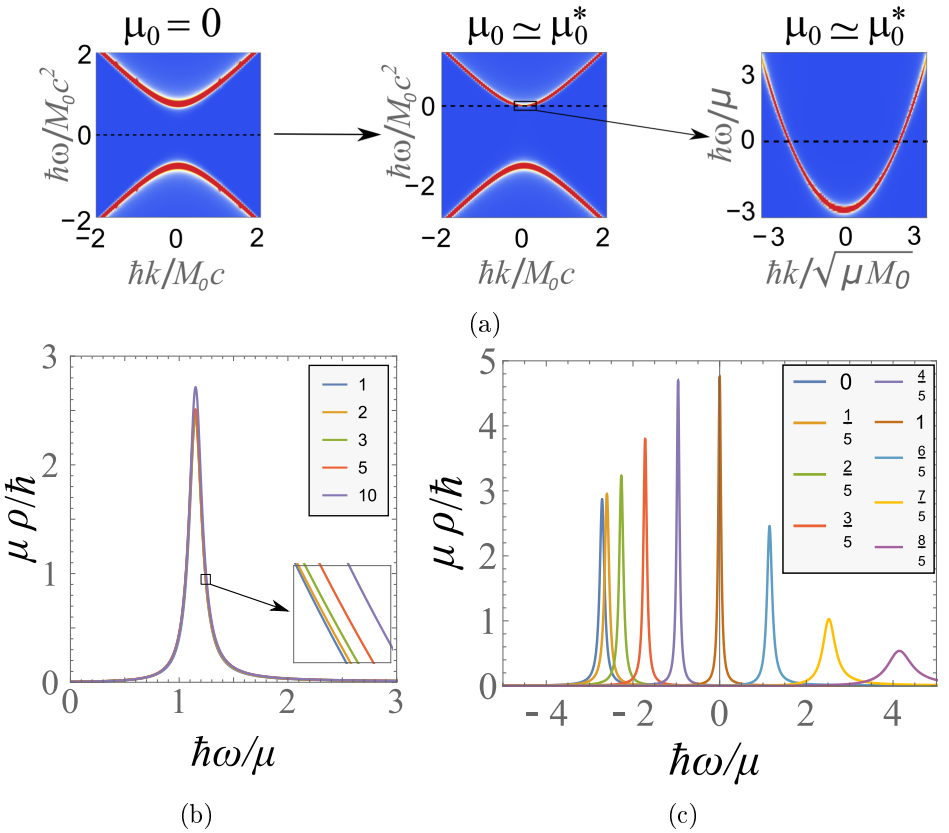


Figure 4.3: (a) Starting with a relativistic spectrum with particle and antiparticle peaks, we obtain nonrelativistic spectra by inspecting the nonrelativistic regime at small $\mu$, where the antiparticle peak decouples. (b) The spectral function at fixed $\beta\mu = 2$ and $k = 6k_F/5$, for several values of $k_BT/M_0c^2$. The legend shows the values of $k_BT/M_0c^2$ in units of $10^{-4}$. (c) The universal spectral functions at fixed $\beta\mu = 2$ for the values of $k/k_F$ shown in the legend. To make this figure, we have fixed $k_BT/M_0c^2 = 10^{-4}$, but note that (b) shows that the dependence of the universal spectral functions on this parameter is negligible. In both (b) and (c) we used $\{q, M, \lambda, g\} = \{1, 49/100, -3/4, 1/3\}$, for which $\hbar k_F \simeq 2.1\sqrt{\mu M_0}$ and $Z \simeq 0.3$. A discussion on the choice of these used model parameters can be found in section 4.B.

with $\omega_0$ the position of the peak at zero momentum. In Fig. 4.3c we show the spectral functions obtained for $\beta\mu = 2$ for several values of $k$. The locations $\omega(k)$ of the peaks in these spectra indeed conform to a nonrelativistic dispersion $\omega(k) = \hbar(k^2 - k_F^2)/2M_{\text{eff}}$ with $k_F$ the Fermi momentum and $M_{\text{eff}} \simeq 0.86M_0$ for the model parameters in the figure that we have chosen such that the spectral functions resemble those of the unitary Fermi gas.

Finally, it is very important to realize that in principle the antiparticle part of the spectrum is still present in our numerics due to the fact that we can make the scale $M_0c^2$ very large, but not truly infinite. However, this part must not be included in the nonrelativistic spectral function that only describes the particles. Naturally, this part of the spectrum also does not collapse. In practice this means that we should cut off the spectrum at some point inside the mass gap. Our results are not very sensitive to this cutoff, provided the scale $M_0c^2$ is taken large enough. By construction, the final spectral functions then also satisfy the desired frequency sum rule $\int \mathrm{d}\omega\rho(\omega, \mathbf{k}) = 2$ for spin-1/2 particles.

## 4.4 Unitary fermions

Unitary fermions constitute, similar to the findings above, a system described at zero temperature by a set of universal constants and whose dimensionless thermodynamic functions depend solely on $\beta\mu$. An example of the former is the constant $\beta_{\text{SF}}$ defined by $\mu = (1 + \beta_{\text{SF}})\epsilon_F$, with $\epsilon_F$ the Fermi energy. Experiments as well as theoretical models have determined that at zero temperature, so in the superfluid phase, $\beta_{\text{SF}} \simeq -0.6$ [27, 28, 34, 36, 102, 103]. The same quantity in the normal phase should in principle be slightly less negative, but is not accurately known at present. Therefore we have for simplicity taken our model parameters such that also $\beta_{\text{N}} \simeq -0.6$. To see this from our spectra we can use that $\epsilon_F = \hbar^2 k_F^2/2m_{\text{id}}$ with $m_{\text{id}}$ the mass of the ideal Fermi gas. The Fermi momentum $\hbar k_F \simeq 2.1\sqrt{\mu M_0}$ follows directly from the dispersion in our spectral functions at low temperatures and the value of the mass $m_{\text{id}} \simeq 0.94M_0$ we obtain from the dispersion of the critical system near $\mu = T = 0$, since our spectral functions indeed contain a very sharp peak in this case.
From our spectral functions we can next calculate the momentum distri-

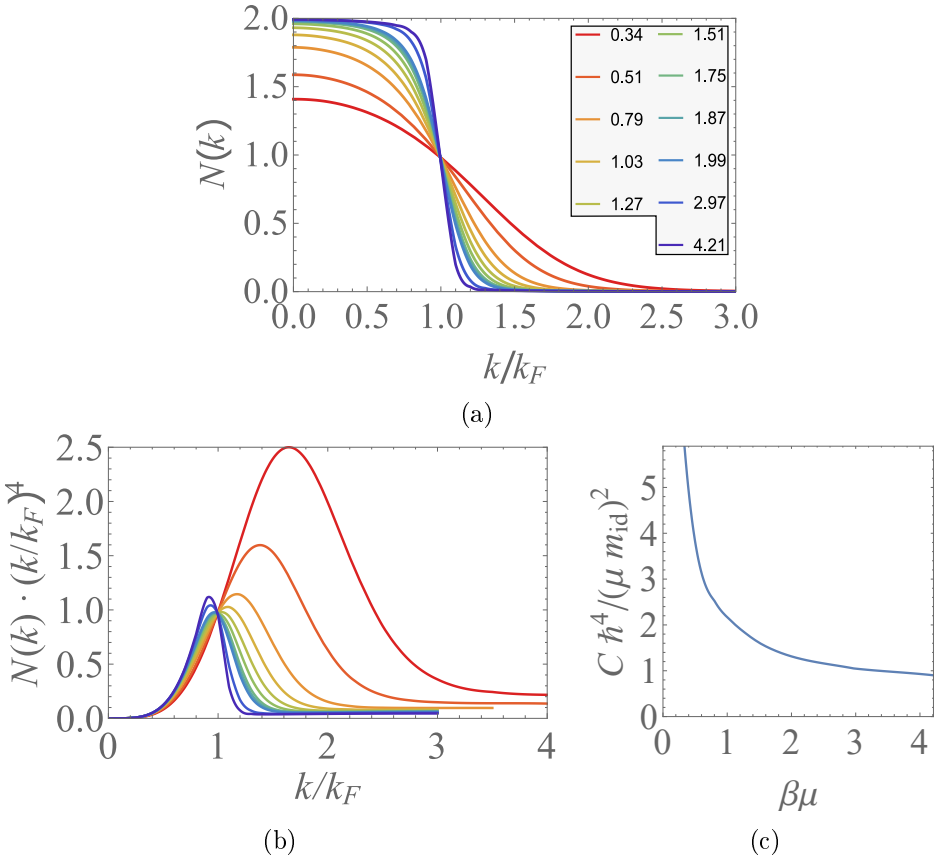


Figure 4.4: (a) The momentum distributions found from the spectral functions integrated with the minimum cut-off frequency $\omega = -10\mu/\hbar$ and including a wavefunction renormalization factor $1/Z$. The legend shows the values of $\beta\mu$. (b) The momentum distributions behave as $1/k^4$ for large $k$, although there are some deviations if $k$ is too large. The coloring is the same as in (a). (c) The contact parameter scaled with $\mu^2 m_{\mathrm{id}}^2/\hbar^4$, as determined from the large momentum tails in (b).

butions $N(\mathbf{k}) = \int \mathrm{d}\omega \rho(\omega, \mathbf{k}) n_F(\hbar\omega)$ with $n_F$ the Fermi-Dirac distribution. These can ultimately be used to determine the equation of state that was already shown previously in Fig. 4.1. Performing the calculation, whose outcome is shown in Fig. 4.4a, we need to realize that the above-mentioned wavefunction renormalization requires us to add an additional factor of $1/Z$

to the momentum distribution. In this manner the integral of $N(\mathbf{k})$ over momentum space approaches the ideal result at low temperatures, as expected from Luttinger's theorem. To understand also physically why this factor is necessary, we note that the spectral functions we obtain generically consist of the nonrelativistic low-frequency peak with a spectral weight of $2Z$ and a long tail at higher frequencies that contains most of the remaining spectral weight. Such tails are a recurring feature in holographic spectra and are related to the non-analytic behavior $(-\omega^2 + c^2k^2)^M$ of the self-energy due to the asymptotically AdS gravitational background. This tail persists even in the low-temperature limit, where the momentum distribution only captures the states at small negative frequencies. We can therefore interpret our spectra as containing a 'coherent' part of weight $2Z$, which is shown in Fig. 4.3 and describes the nonrelativistic unitary fermions, and an 'incoherent' part of weight $2(1 - Z)$.

Comparing the momentum distributions to the results of Ref. [104, 105], we see that many features of the unitary Fermi gas are reproduced by our nonrelativistic fermions. For instance, we have checked that the slope of $N(\mathbf{k})$ at the Fermi momentum does not diverge in the zero-temperature limit, which signals a non-Fermi-liquid behavior and is in agreement with Fig. 6 of Ref. [105]. Moreover, the characteristic asymptotic behavior of the momentum distributions as $C/k^4$ for large $k$ in terms of the contact parameter $C$, is also seen in our data in Fig. 4.4b, although we observe some relativistic corrections for even larger $k$. From this figure we can also read off the contact parameter, which results in Fig. 4.4c. We remind that to calculate the momentum distributions, we must introduce a frequency cutoff inside the gap from which we start integrating the spectral functions. The dependence on this cutoff is negligible for the momentum distributions in Fig. 4.4a themselves, but the cutoff does have some influence on the tails in Fig. 4.4b, as small deviations get amplified by the factor $k^4$. Given these uncertainties and the fact that we can still fine-tune several model parameters, we find the agreement with Fig. 2b of Ref. [105] rather encouraging. Note that our momentum distributions contain also an interesting crossing point, which appears to be a universal feature of strongly interacting systems [106].

Finally, we calculate the total density by integrating the momentum distributions over momentum space. The result, normalized by the ideal Fermi gas density for which the momentum distribution for $\mu > 0$ reads $N_{\mathrm{id}}(k) = 2n_F(\mu k^2/k_{F,\mathrm{id}}^2 - \mu)$, is shown in Fig. 4.1. For low temperatures our result

asymptotically approaches $1/(1+\beta_{\mathrm{N}})^{3/2}$ with $\beta_{\mathrm{N}} \simeq -0.6$, as expected. This limit is not clearly visible in the data of Refs. [34, 97], since there at low temperatures the unitary gas becomes superfluid, a feature that we have not included yet but can also be achieved holographically.

## 4.5 Discussion and outlook

Up to now, we have used holography as a bottom-up approach in which the various model parameters can be tuned to fit to experiments. However, the holographic dictionary also provides insight into the physical significance of these parameters. For instance, the conformal dimension of the operator $\mathcal{O}$ is equal to $2+M$, and $q$ and $\lambda$ determine the strength of the CFT three-point functions $\langle \mathcal{O}^\dagger \mathcal{O}(\Psi^\dagger \Psi)\rangle$ and $\langle \mathcal{O}^\dagger \mathcal{O}(\Psi^\dagger \gamma^0 \Psi)\rangle$, respectively. In the context of the unitary Fermi gas a natural choice for the operator $\mathcal{O}$ is $\Psi^\dagger$ multiplied with the annihilation operator of a Feshbach molecule. If this identification is correct then $g$ would correspond to the atom-molecule coupling of the Feshbach resonance. Exploring these possible microscopic connections in detail is beyond the scope of the present paper and is left for future work. Continuing in the spirit of bottom-up holography, however, our approach allows for many extensions by adding more ingredients to the gravitational dual theory, such as the inclusion of the backreaction on the bulk geometry by a complex scalar field that is dual to the superfluid order parameter and the introduction of a spin and/or mass imbalance.

## 4.A Actions and equations of motion for the bulk theory

In this section we present more details on the gravitational background that is used to obtain the results in the main text. In particular, we present the equations of motion that need to be solved in order to obtain this background. Moreover, we present the equations of motion for the probe Dirac spinors propagating on this background, which ultimately lead to the self-energy of our spectral functions.

### 4.A.1 Gravitational background

The bulk theory contains a gauge field $A = A_t \mathrm{d}t$ to account for the chemical potential in the CFT and a scalar field $\phi$ to account for the mass deformation in the CFT. The scalar field is tachyonic with mass $m_\phi^2 = -3$, such that the corresponding deformation of the CFT has the dimension of a fermionic mass deformation.

The gravitational background follows from the backreaction of these fields on the geometry described by the metric $g_{MN}$, which follows from the action

$$S_{\text{background}} = \int \mathrm{d}^5x\sqrt{-g}\left(R + 12 - \frac{1}{4}F^2 - \frac{1}{2}\left((\partial\phi)^2 + m_\phi^2\phi^2\right)\right). \tag{4.4}$$

Here, $g$ is the determinant of the metric, $R$ is the Ricci scalar, $F = \mathrm{d}A$ and $(\partial\phi)^2 = \partial_M\phi\partial^M\phi$. Moreover, we note that the first two terms in the Lagrangian density represent the standard Einstein-Hilbert Lagrangian $R-2\Lambda$, since in our units the cosmological constant is given by $\Lambda = -6$ as explained in Appendix 4.C.

For the metric $\mathrm{d}s^2 = g_{MN}\mathrm{d}x^M\mathrm{d}x^N$ we use the following *Ansatz*:

$$\mathrm{d}s^2 = -f(r)e^{-\chi(r)}\mathrm{d}t^2 + \frac{\mathrm{d}r^2}{f(r)} + r^2\mathrm{d}\mathbf{x}^2\,, \tag{4.5}$$

where the metric components as well as $A_t$ and $\phi$ only depend on the radial coordinate $r$ due to planar symmetry. The equations of motion following from eq. (4.4) can then be written as

$$\phi'' + \left(\frac{f'}{f} + \frac{3}{r} - \frac{\chi'}{2}\right)\phi' + \frac{3}{f}\phi = 0\,, \tag{4.6}$$

$$A_t'' + \left(\frac{3}{r} + \frac{\chi'}{2}\right)A_t' = 0\,, \tag{4.7}$$

$$\chi' + \frac{r}{3}\phi'^2 = 0\,, \tag{4.8}$$

$$f' + \left(\frac{2}{r} - \frac{\chi'}{2}\right)f + \frac{r}{6}e^{\chi}A_t'^2 - \frac{r}{2}\phi^2 - 4r = 0\,, \tag{4.9}$$

where a prime denotes differentiation with respect to $r$. A gravitational background then follows from solving this system with the initial conditions $f(r_+) = 0$, $A_t(r_+) = 0$, $\chi(r_+) = 0$ and two free initial conditions $\phi(r_+)$ and $A_t'(r_+)$. After solving the system, the solution is rescaled such that in the end $\chi(\infty) = 0$ as required for asymptotically anti-de Sitter spacetimes. It can be shown that $\phi'(r_+)$ is not independent of the other initial conditions.

After numerically solving the above system of equations, we extract the parameters of the CFT. The temperature follows from the metric tensor via

$$T = \frac{f'(r_+)e^{-\chi(r_+)/2}}{4\pi}, \tag{4.10}$$

whereas the chemical potential per unit charge and the mass are given by the boundary values $\mu_0/q = A_t(\infty)$ and $M_0 = \lim_{r\to\infty} r\phi(r)/\alpha$ respectively. Here the proportionality constant $\alpha = \sqrt[4]{3/\pi^2}$ is discussed in Ref. [2], however, note that there $\alpha$ is defined as what is $1/\alpha$ here.

### 4.A.2 Probe spinors

The self-energy of our spectral functions follow from the solution $\Xi$ of Eq. (3) in the main text. To derive this equation, we have two Dirac spinors $\psi^{(1)}$ and $\psi^{(2)}$ propagate on the bulk theory obtained from the equations of motion above. These spinors have masses $M_1 = M$ and $M_2 = -M$ respectively and are coupled to the gauge field $A_M$ with a charge $q$. The associated action is given by

$$\begin{aligned} S_{\text{Dirac}} = {} & ig_f \int \mathrm{d}^5x\sqrt{-g}\left(\bar\psi^{(1)}\left(\not{D} - M\right)\psi^{(1)} + \bar\psi^{(2)}\left(\not{D} + M\right)\psi^{(2)}\right) \\ & + ig_Y \int \mathrm{d}^5x\sqrt{-g}\phi\left(\bar\psi^{(1)}\psi^{(2)} + \bar\psi^{(2)}\psi^{(1)}\right) \\ & + ig_f \int \mathrm{d}^4x\sqrt{-h}\left(\bar\psi_R^{(1)}\psi_L^{(1)} - \bar\psi_L^{(2)}\psi_R^{(2)}\right). \end{aligned} \tag{4.11}$$

where $\bar\psi = \psi^\dagger\Gamma^{\underline{0}}$, $\not{D} = \Gamma^M(\nabla_M - iqA_M)$, $g_f$ and $g_Y$ are coupling constants, $h$ is the determinant of the induced metric on the boundary and $\psi_{R,L}^{(i)} = (1 + \Gamma^{\underline{r}})\psi^{(i)}/2$. The spinor covariant derivative $\nabla$ and the Dirac matrices in $(4+1)$-dimensional flat ($\Gamma^{\underline{M}}$) and curved ($\Gamma^M$) spacetime are defined in

Appendix 4.C. The action consists of a standard Dirac action for the spinors $\psi^{(i)}$, a Yukawa term which is necessary to couple the chiral components of the spinor on the boundary and a boundary action to be consistent with the Dirichlet boundary conditions $\delta\psi_R^{(1)} = 0$ and $\delta\psi_L^{(2)} = 0$. Defining $\lambda = g_Y/g_f$, the equations of motion from the spinor are then

$$\left(\not{D} - M\right)\psi^{(1)} = -\lambda\phi\psi^{(2)}, \tag{4.12}$$

$$\left(\not{D} + M\right)\psi^{(2)} = -\lambda\phi\psi^{(1)}. \tag{4.13}$$

Next, we define the Dirac spinors $\Psi = \psi_R^{(1)} + \psi_L^{(2)}$ and $\eta = \psi_L^{(1)} - \psi_R^{(2)}$, in terms of which the on-shell action is

$$S^{\text{on shell}} = ig_f \int \mathrm{d}^4x\sqrt{-h}\bar{\Psi}\eta. \tag{4.14}$$

The matrix $\Xi$ is now defined in momentum space by

$$\eta(r,k) = -i\Xi(r,k)\Psi(r,k), \tag{4.15}$$

so that $\Xi$ is related to the Green's function for the fermionic boundary operator sourced by the Dirac spinor $\Psi$ on the boundary. Eq. (3) in the main text then follows from the above definition when imposing the Dirac equations for $\Psi$ and $\eta$, which follow from rewriting the Dirac equations for $\psi^{(1)}$ and $\psi^{(2)}$.

## 4.B On the choice of parameters used to obtain nonrelativistic spectra

In general, a spectral function $\rho(\omega, \mathbf{k})$ depends on the gravitational-background parameters $k_BT/M_0c^2$ and $\mu_0/M_0c^2$ and the model parameters $q$, $M$ and $\lambda$ and $g$. Not every set of the parameters $\{q, M, \lambda, g\}$ is suitable to obtain universal nonrelativistic spectra with holographic interactions. Firstly, to satisfy the frequency sum rule, we must have that $-1/2 < M < 1/2$ [81]. Moreover, we can restrict to positive $g$ since the spectral functions only depend on $g^2$. In this section we discuss some more restrictions on this set, which we have taken into account for the values of the paramaters used in the main text. In particular, fixing $q$ and $M$, we find a restriction on $\lambda$.

To derive such restrictions, we should realize that the self-energy contains a gap itself. If the peaks in the nonrelativistic spectral functions are situated inside this gap, they will not be broadened and the resulting spectrum will resemble a noninteracting one, containing delta peaks at each value of $k$. Since the gap in the self-energy $\Xi$ is proportional to $|\lambda|M_0c^2$, we expect this to occur for large values of $|\lambda|$. In the analysis below we indeed find an upper bound for $|\lambda|$.

For $k = 0$, the peak in the nonrelativistic spectrum is not situated inside the gap of the self-energy if we restrict to chemical potentials $\mu_0$ that are greater than the critical chemical potential $\mu_0^*$ in the limit $g \to \infty$. Since for nonrelativistic spectra $\mu_0 \simeq \mu_0^*$, we can write this criterion as

$$\mu_0^*(q, M, \lambda, g) > \mu_0^*(q, M, \lambda, \infty). \tag{4.16}$$

This condition should also be sufficient for nonrelativistic spectral functions at nonzero $k$, provided that the difference between $\mu_0^*(q, M, \lambda, g)$ and $\mu_0^*(q, M, \lambda, \infty)$ is not nonrelativistically small. For parameters satisfying this condition, we indeed find spectra containing peaks with a nontrivial width, such as the ones in the main text.

To see what the above condition implies for the allowed sets of model parameters, we study the behavior of the critical chemical potential $\mu_0^*$ as a function of $\lambda$ and $g$ for fixed $q$ and $M$. Noting that at the critical chemical potential we have that $k_F = 0$, we can use that the Fermi momentum $k_F(\lambda, g, \mu_0)$ at $g = \infty$ depends on $\lambda$ as

$$k_F(\lambda, \infty, \mu_0) = k_{F,0}\sqrt{1 - \frac{\lambda^2}{\lambda_c^2}}, \tag{4.17}$$

where $k_{F,0} = k_F(0, \infty, \mu_0)$ and $\lambda_c$ is defined as the positive value of $\lambda$ at which the Fermi momentum at $g = \infty$ is zero. This dependence is found numerically and is shown in Fig. 4.5. All dependence on $\mu_0$ is contained in $k_F(0, \infty, \mu_0)$ and $\lambda_c(\mu_0)$. Putting eq. (4.17) to zero yields that the critical chemical potential at $g = \infty$ is given by the solution of $|\lambda| = \lambda_c(\mu_0)$. It was furthermore found in Ref. [2] that except for small $\mu_0$, both $k_{F,0}$ and $\lambda_c$ are

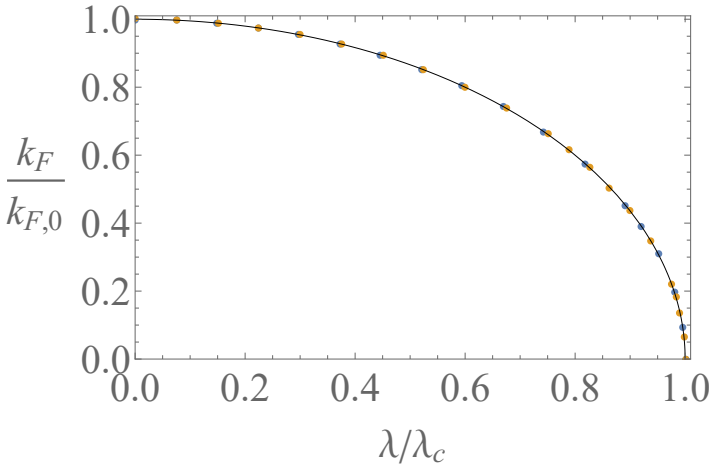


Figure 4.5: The Fermi momentum at $g = \infty$ as a function of $\lambda$ depends on $\mu_0$ only through $k_{F,0}$ and $\lambda_c$. Here, we used $q = 1$, $M = 49/100$ and $k_B T = 10^{-4} M_0 c^2$, which is small enough to determine $k_F$. The values of $\mu_0/M_0c^2$ are 1/2 (blue dots) and 1 (yellow dots). The black curve shows the graph of $\sqrt{1-x^2}$, with $x = \lambda/\lambda_c$.

linear in $\mu_0 > 0$, so that in this regime we can write $\lambda_c \simeq B\mu_0/M_0c^2$ with $B$ a positive coefficient which depends on $q$ and $M$. It follows that at $g = \infty$ we get

$$\mu_0^*(\lambda, \infty) = \frac{|\lambda|}{B} M_0 c^2 \tag{4.18}$$

so that the criterion in eq. (4.16) can be written as $|\lambda| M_0 c^2 < B\mu_0^*(\lambda, g)$.

We proceed by studying the dependence of the critical chemical potential $\mu_0^*$ on $\lambda$ and $g$, of which the result is shown in Fig. 4.6. Clearly, for $g = 0$ we have that $\mu_0^* = M_0c^2$. For $\lambda < 0$, we then find that $\mu_0^*/M_0c^2$ is a monotonic function starting at 1 and asymptotically approaching $|\lambda|/B$. In contrast, when $\lambda > 0$ we observe that $\mu_0^*/M_0c^2$ monotonically decreases to 0 for some value of $g$, after which it monotonically increases to $\lambda/B$. These findings indicate that we can only obey the criterion in eq. (4.16) if $\mu_0^*(\lambda, \infty) < M_0c^2$, i.e.,

$$|\lambda| < B, \tag{4.19}$$

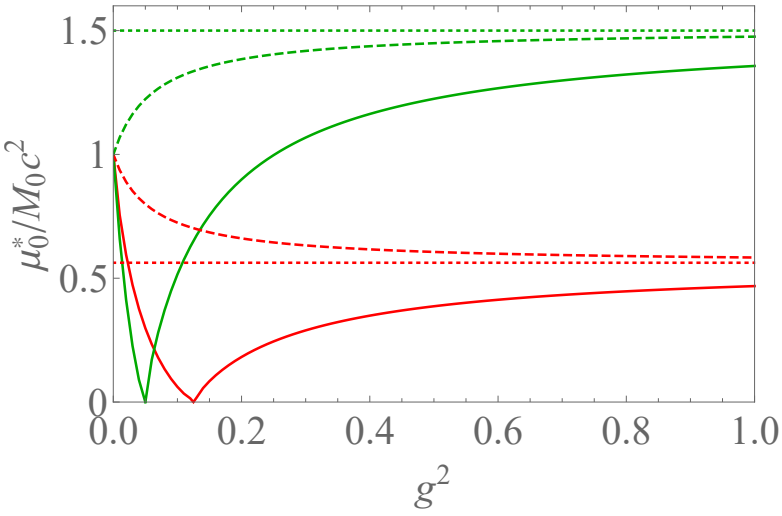


Figure 4.6: The critical chemical potential as a function the coupling $g$. Here $|\lambda| = 3/4$ for the red curves and $|\lambda| = 2$ for the green curves. The solid curves correspond to positive $\lambda$ and the dashed curves correspond to negative $\lambda$. The dotted lines denote the asymptotic values of the curves, which are equal to $|\lambda|/B$. Here we used $q = 1$ and $M = 49/100$, for which $B \simeq 1.33$.

which for fixed values of $q$ and $M$ gives an upper bound for $|\lambda|$. From Fig. 4.6 we furthermore observe that there is no restriction on $g$ for negative $\lambda$, whereas for positive $\lambda$ an upper bound for $g^2$ is required to satisfy eq. (4.19).

For the parameters $q = 1$ and $M = 49/100$, which are used in the main text, we have that $B \simeq 1.33$, so that our choice $\lambda = -3/4$ satisfies the criterion above in eq. (4.19). We remark that we should not choose $|\lambda|$ too small, since then an additional peak near the chemical potential at $\omega = 0$ appears in our spectra. This leads to an avoided crossing between this peak and the particle band, which makes it hard to define the critical chemical potential. Having opted for a negative $\lambda$, the above discussion imposes no further restriction on $g$. However, to obtain nonrelativistic spectra, we should not take $g$ too large. To see this, we note that we can think of $g$ as a measure for the region in momentum space where the holographic interactions dominate the free kinetic part of the Green's function. As a consequence, for large

$g$ we find that the tails at higher frequencies in the spectral functions that were mentioned in the main text persist until deep in the relativistic regime. Moreover, the spectral weight in the gap is then no longer negligible. This is not the case for the value $g = 1/3$ used in the main text, which we have taken to reproduce the value $\beta_N \simeq -0.6$. Finally, the chosen value for $M$ in the main text is also related to the above-mentioned tails. We find that choosing $M$ close to its supremum $1/2$ avoids long tails extending to relativistic $\omega$. In particular, the spectral functions decay faster than $1/\omega$ for large $\omega$, i.e., for $\omega \gg \mu$ but still within the nonrelativistic regime, as is necessary to obey the sum rule.

## 4.C Conventions on units and Dirac theory

The action for the gravitational background in eq. (4.4) in SI units reads

$$S = \int \mathrm{d}^5x\sqrt{-g}\left(\frac{c^3}{16\pi G_5}(R-2\Lambda) - \frac{1}{4\mu_5 c}F^2 - \left((\partial\phi)^2 + \frac{m_\phi^2 c^2}{\hbar^2}\phi^2\right)\right). \tag{4.20}$$

Here $G_5$ and $\mu_5$ are Newton's constant and the vacuum permeability respectively, defined in 4+1 spacetime dimensions. Using the cosmological constant $\Lambda$ we can define the anti-de Sitter radius as $L^2 = 6/(-\Lambda)$, noting that the cosmological constant is always negative in the asymptotically anti-de Sitter spacetimes that we are dealing with. The dimensionless gauge field and scalar field are then defined as

$$\tilde{A}_{\tilde{t}} = \sqrt{\frac{16\pi G_5}{\mu_5 c^6}}A_t, \tag{4.21}$$

$$\tilde{\phi} = \sqrt{\frac{16\pi G_5}{c^3}}\phi. \tag{4.22}$$

The tildes, which we omit in the main text, denote dimensionless quantities. The metric signature is mostly plus and its components are defined by $\mathrm{d}s^2 = g_{MN}\mathrm{d}x^M\mathrm{d}x^N$, with $x^M = \{ct, r, \mathbf{x}\}$ where capital Roman letters refer to $(4+1)$-dimensional spacetime, as opposed to Greek letters for which $x^\mu = \{ct, \mathbf{x}\}$. With this definition of the metric, the components $g_{MN}$ are already dimensionless. All dimensionless units in main text are obtained by scaling

all length scales by $L$, i.e., putting $\Lambda = -6$. As a consequence, when putting $\hbar = 1$ and $c = 1$, all energy (or mass) scales are expressed in units of $\hbar c/L$ (or $\hbar/cL$). This is also true for the temperature $T$, setting Boltzmann's constant $k_B = 1$. Finally, the Dirac fields in eq. (4.11) are in units of $\sqrt{\hbar}/L$ and the dimensionless charge of the probe field is given by

$$\tilde{q} = \sqrt{\frac{\mu_5 c^6}{16\pi G_5}} \frac{L}{\hbar c} q. \tag{4.23}$$

In the main text we use the dimensionless units defined here for bulk parameters such as $M$ and $q$. For quantities defined in the CFT we use SI units, which means we restore $c$, $\hbar$ and $k_B$.

The Dirac matrices in flat $(3+1)$-dimensional spacetime are given by

$$\gamma^{\underline{\mu}} = \begin{pmatrix} 0 & \bar{\sigma}^\mu \\ \sigma^\mu & 0 \end{pmatrix} \tag{4.24}$$

where $\sigma = (\mathbb{I}_2, \sigma^i)$ and $\bar{\sigma} = (-\mathbb{I}_2, \sigma^i)$ with $\sigma^i$ the Pauli matrices and $\mathbb{I}_2$ the $2\times2$ identity matrix. Moreover, we use underlined indices for tensors and Dirac matrices defined in flat spacetime, so that $g^{\underline{MN}} = \eta^{\underline{MN}} = \mathrm{diag}(-1,1,1,1,1)$. The gamma matrices $\Gamma^{\underline{M}}$ in $(4+1)$-dimensional flat spacetime are given by $\Gamma^{\underline{\mu}} = \gamma^{\underline{\mu}}$ for $\mu \neq r$ and

$$\Gamma^{\underline{r}} = \gamma^{\underline{5}} \equiv i\gamma^{\underline{0}}\gamma^{\underline{1}}\gamma^{\underline{2}}\gamma^{\underline{3}} = \begin{pmatrix} \mathbb{I}_2 & 0 \\ 0 & -\mathbb{I}_2 \end{pmatrix}. \tag{4.25}$$

The vielbeins $e^{\underline{M}}_{N}$ that appear in the Dirac action in eq. (4.11) in curved spacetime are defined by

$$g_{MN} = e^{\underline{P}}_{M} e^{\underline{Q}}_{N} \eta_{\underline{PQ}} \tag{4.26}$$

where the inverse vielbeins satisfy $e^{M}_{\underline{P}} e^{\underline{P}}_{N} = \delta^{M}_{N}$ and $e^{P}_{\underline{M}} e^{\underline{N}}_{P} = \delta^{\underline{N}}_{\underline{M}}$. For the metric in eq. (4.5) this gives

$$e^{0}_{\underline{0}} = \sqrt{\frac{e^{\chi(r)}}{f(r)}}, \tag{4.27}$$

$$e^{r}_{\underline{r}} = \sqrt{f(r)}, \tag{4.28}$$

$$e^{i}_{\underline{i}} = \frac{1}{r}. \tag{4.29}$$

In the main text, we have omitted the underlines and only use the Dirac matrices in flat spacetime. Moreover, all vielbeins in the main text are such that their lower index corresponds to the flat one.

The spinor covariant derivative $\nabla_M$, which also appears in the Dirac action in eq. (4.11), is defined as

$$\nabla_M \psi = \partial_M \psi + \Omega_M \psi \tag{4.30}$$

with $\Omega_M$ given by

$$\Omega_M = \frac{1}{8} \omega_{M \underline{NP}} [\Gamma^{\underline{N}}, \Gamma^{\underline{P}}] \tag{4.31}$$

and the spin connection $\omega^{\underline{M}}_{\underline{NP}}$ given by

$$\omega^{\underline{M}}_{\underline{NP}} = e^{\underline{M}}_{Q} e^{R}_{\underline{P}} \Gamma^{Q}_{NR} - e^{Q}_{\underline{P}} \partial_N e^{\underline{M}}_{Q}. \tag{4.32}$$

Here $\Gamma^M_{NP}$ denotes the Christoffel connection. The spin connection does not appear in the equation for $\Xi$ in the main text, as we can remove it by rescaling the probe spinors by a function depending on $r$ only, see appendix A.2 in Ref. [2] for details.

# 5 Towards nonrelativistic bosons from holography

## 5.1 Introduction

Ultracold Fermi gases at or near unitarity provide a rich playground for modelling strongly coupled physics. The principal reason for this is that the discovery [21] and the experimental observation [24] of Feshbach resonances in ultracold gases have greatly improved the experimental accessibility of this regime. This has led to many theoretical models of such ultracold gases [3, 35–37, 97, 101] that can be directly compared to the abundant experimental data [25–29, 34, 98–100]. In particular, due to the universal behavior that these Fermi gases exhibit in the unitarity limit, they constitute a perfect test case for the application of the AdS/CFT correspondence to nonrelativistic systems. This has been explored in Ref. [3].

An analogous comparison for ultracold strongly coupled Bose gases is more intricate. Although Feshbach resonances exist for both fermions and bosons, the stability of the Bose gas is burdened by a large atomic loss rate. This loss rate, which is caused by three-body recombination processes due to the existence of so-called Efimov states [10], increases in the vicinity of the resonance [11] and at low temperatures [15–17]. It is therefore more complicated to experimentally realize a unitary Bose gas that is metastable for a sufficiently large amount of time. In spite of this, if such a metastable Bose gas can indeed be created, it should exhibit universal features similar to its fermionic counterpart.

We therefore examine here the construction of a holographic model for such ultracold Bose gases by generalizing the approaches in Refs. [2, 3] to the bosonic case. This method firstly consists of introducing a mass gap in the spectrum of relativistic bosons obtained by holography. Subsequently, we should study the nonrelativistic limit, in which this newly introduced mass scale is large compared to all the other scales in the system. As a starting point, we will work towards a universal metastable Bose gas, assuming that

we can neglect the loss rate caused by Efimov trimers. However, this is still work in progress. In this chapter we mainly concentrate on the first step towards this goal, i.e., introducing a mass gap in the spectrum of a Klein-Gordon field obtained from (semi)holography.

The outline of this chapter as follows. We start by describing in section 5.2 the method to obtain the spectral function of an elementary Klein-Gordon field from holography. To this end we generalize the dynamical-source model in Ref. [81] to the case of bosons, already including a mass deformation in the bulk. In section 5.3 we subsequently show, for zero chemical potential, that this procedure indeed introduces a mass gap in both the holographic and semiholographic spectra. Finally, we present some of our findings when turning on the chemical potential in section 5.4. These findings, however, require more research which is postponed to future work. In this chapter we use the same dimensionless units as in chapter 3.

## 5.2 Obtaining massive bosons from holography

In this section we discuss a procedure that yields the dynamics of a massive boson from holography. This procedure consists of two steps that are similar to those used to obtain massive fermions in Ref. [2]. In the first step we determine the gravitational background, which fixes the temperature, chemical potential and the bare mass parameter in the boundary field theory. The second step consists of determining the holographic Green's function of the massive scalar field in the boundary. This amounts to solving the Klein-Gordon equation of this scalar field on top of bulk geometry found previously. Lastly, in this section we also derive the semiholographic Green's function of the scalar field using a dynamical-source model and discuss the corresponding frequency sum rule.

### 5.2.1 Gravitational theory

The boundary we wish to study consists of massive spinless bosons at a nonzero chemical potential $\mu$ and at a temperature $T$. To this end we can take the gravitational background as in Ref. [2], which includes a black brane that gives rise to a temperature in the field theory, a gauge field $A = A_t \mathrm{d}t$

that yields a chemical potential and a scalar field $\phi$ to account for a mass deformation. The action for this background reads

$$S_{\text{background}} = \int \mathrm{d}^5x\sqrt{-g}\left(R + 12 - \frac{1}{4}F^2 - \frac{1}{2}\left((\partial\phi)^2 + m_\phi^2\phi^2\right)\right), \quad (5.1)$$

where $F = \mathrm{d}A$. In contrast to Ref. [2], we now fix the mass of the scalar field to $m_\phi^2 = -4$, saturating the Breitenlohner-Freedman bound. In this way, the operator dual to $\phi$ has dimension $\Delta = 2$ and the dimension of the corresponding deformation in the boundary theory matches that of a free bosonic mass deformation. The source of the scalar field provides the bare mass $M_0^2$ for the elementary Klein-Gordon field on the boundary, up to a proportionality constant that we discuss in appendix 5.A. We use the following *Ansatz* for a static metric tensor with planar symmetry:

$$\mathrm{d}s^2 = -f(r)e^{-\chi(r)}\mathrm{d}t^2 + \frac{\mathrm{d}r^2}{f(r)} + r^2\mathrm{d}\mathbf{x}^2\,, \quad (5.2)$$

where $(t, r, \mathbf{x})$ denotes the spacetime position in the bulk, with the boundary being at $r = \infty$. This metric has a black-brane horizon at $r = r_+$, so that $f(r_+) = 0$. The temperature in the field theory is then equal to the Hawking temperature of this black brane, given by

$$T = \frac{f'(r_+)e^{-\chi(r_+)/2}}{4\pi}\,, \quad (5.3)$$

where the prime denotes differentiation with respect to $r$.

The gravitational bulk is now found by solving the equations of motion, which are given by

$$\phi'' + \left(\frac{f'}{f} + \frac{3}{r} - \frac{\chi'}{2}\right)\phi' + \frac{4}{f}\phi = 0\,, \quad (5.4)$$

$$A_t'' + \left(\frac{3}{r} + \frac{\chi'}{2}\right)A_t' = 0\,, \quad (5.5)$$

$$\chi' + \frac{r}{3}\phi'^2 = 0\,, \quad (5.6)$$

$$f' + \left(\frac{2}{r} - \frac{\chi'}{2}\right)f + \frac{r}{6}e^{\chi}A_t'^2 - \frac{2}{3}r\phi^2 - 4r = 0\,. \quad (5.7)$$

A solution to these equations is specified by the two initial conditions $\phi(r_+)$ and $A_t'(r_+)$, see e.g. the discussion in Ref. [2]. The corresponding boundary theory is described by two dimensionless parameters, formed out of the three dimensionful parameters $T$, $\mu$ and $M_0$.

We remark that we only consider solutions that correspond to a nonzero mass $M_0$. According to Ref. [55], for our current setup there should also exist holographic-superconductor solutions, for which the scalar source vanishes. This is because we satisfy the criterion

$$q_\phi^2 > \frac{m_\phi^2}{2} + \frac{d(d-1)}{8}, \tag{5.8}$$

where in our case $d = 4$, $m_\phi^2 = -4$ and $q_\phi = 0$. We will not consider these unsourced solutions, and neither will we consider solutions where the profile of the scalar $\phi$ has nodes.

### 5.2.2 Green's function for the massive boson

As dictated by the holographic dictionary, we obtain the bosonic Green's function by having a probe complex scalar field $\sigma$ propagate on the bulk described above. Note that this scalar field is different from the real scalar field $\phi$ which induces the mass deformation. The dynamics of the probe scalar are described by the bulk action

$$S_{\mathrm{KG}} = -g_b \int \mathrm{d}^5x\sqrt{-g}\left(|D\sigma|^2 + m_\sigma^2|\sigma|^2\right) + S_{\mathrm{bdy}}, \tag{5.9}$$

where $g_b$ is a coupling constant, $D_\mu = \nabla_\mu - iqA_\mu$ with $\nabla$ the covariant derivative, $q$ is the bulk charge of $\sigma$ under the $U(1)$ gauge field $A_\mu$ so that the chemical potential equals $qA_t(\infty)$, $m_\sigma$ is the bulk mass of the probe scalar and $S_{\mathrm{bdy}}$ is a boundary action that we specify later. The Klein-Gordon equation that follows from eq. (5.9) reads

$$\left(D^2 - m_\sigma^2\right)\sigma = 0. \tag{5.10}$$

Fourier transforming $\sigma$ on slices of constant $r$, we can write this as

$$\sigma'' + \left(\frac{f'}{f} - \frac{\chi'}{2} + \frac{3}{r}\right)\sigma' - \frac{m_\sigma^2 + \frac{|\mathbf{k}|^2}{r^2} - (\omega + qA_t)^2\,\frac{e^\chi}{f}}{f}\sigma = 0, \tag{5.11}$$

where now $\sigma = \sigma(r;\omega,\mathbf{k})$. Here the functions $f$, $A_t$ and $\chi$ are fixed and given by the bulk geometry described in the previous subsection. From this equation we can derive that asymptotically, the behavior of $\sigma$ is described by two linearly independent fall-offs,[1] i.e.,

$$\sigma = \sigma_s r^{-\Delta_-} + \sigma_v r^{-\Delta_+} + \cdots , \tag{5.12}$$

where $\Delta_\pm = 2 \pm \nu$ with

$$\nu \equiv \sqrt{4 + m_\sigma^2}. \tag{5.13}$$

The coefficient $\sigma_s$ now corresponds to a scalar source in the boundary theory. The boundary action in eq. (5.9) that is consistent with this interpretation is given by

$$S_{\text{bdy}} = -g_b \int_{r=r_0} \mathrm{d}^4x \sqrt{-h} \Delta_- |\sigma|^2, \tag{5.14}$$

where $r_0$ is a cutoff surface that will ultimately be sent to infinity.[2] Including this boundary action, we can indeed show that the total on-shell action in momentum space can be written as

$$S_{\text{KG}}^{\text{on shell}} = g_b \int \frac{\mathrm{d}^4k}{(2\pi)^4} \sigma_s^*(k) G_{\mathcal{O}}(k) \sigma_s(k), \tag{5.15}$$

where $k_\mu = (-\omega, \mathbf{k})$ and where $G_{\mathcal{O}}$ is the Green's function for the expectation value of the operator $\mathcal{O} = 2\nu\sigma_v$ that is sourced by $\sigma_s$, i.e.,

$$G_{\mathcal{O}}(k) = 2\nu \frac{\sigma_v(k)}{\sigma_s(k)}. \tag{5.16}$$

In short, the above implies that to find the holographic Green's function of the massive boson in the field theory, we must solve the Klein-Gordon equation in eq. (5.11) and subsequently determine the ratio of the resulting coefficients $\sigma_v$ and $\sigma_s$. For the *retarded* Green's function, we must supplement eq. (5.11) with infalling boundary conditions at the horizon, which implies that $\sigma$ behaves as[3]

$$\sigma \propto (r - r_+)^{-\frac{i\omega}{4\pi T}}. \tag{5.17}$$

[1] For the values of $m_\sigma^2$ we will be considering, the dots in the expansion in eq. (5.12) contain no powers of $r$ with exponents in the interval $(-\Delta_+, -\Delta_-)$.

[2] We have neglected a factor of $\sqrt{f}/r_0$ in the boundary action, since for large $r$ we have that $f = r^2$ to leading order.

[3] The other behavior near the horizon that is allowed by eq. (5.11) is $\sigma \propto (r - r_+)^{i\omega/4\pi T}$. This behavior corresponds to outgoing boundary conditions and yields the advanced Green's function instead.

### 5.2.3 Semiholographic Green's function

To make a connection with the unitary Bose gas, the object we ultimately want to obtain is the Green's function for an elementary boson. Therefore, we consider here a relativistic Klein-Gordon field $\varphi$, which we linearly couple to the strongly interacting (deformed) CFT through a bosonic operator $\mathcal{O}$. The corresponding grand-canonical action for this setup is given by

$$S = \int \frac{\mathrm{d}^4 k}{(2\pi)^4} \left\{ -\varphi^* \left( K^2 + M_0^2 \right) \varphi + g\varphi^* \mathcal{O} + g\mathcal{O}^* \varphi \right\} + S_{\mathrm{CFT}} \tag{5.18}$$

where $K_\mu = (-\omega - \mu, \mathbf{k})$, $K^2 = -(\omega + \mu)^2 + |\mathbf{k}|^2$ and $S_{\mathrm{CFT}}$ is the action of the CFT that contains $\mathcal{O}$. From the above, we can find the effective semiholographic Green's function for the elementary scalar field $\varphi$ by integrating out the CFT, which yields

$$G_R^{-1}(\omega, \mathbf{k}) = -(\omega + \mu)^2 + |\mathbf{k}|^2 + M_0^2 - \Sigma(\omega, \mathbf{k}), \tag{5.19}$$

where $\Sigma = g^2 G_{\mathcal{O}}$, so that the Green's function $G_{\mathcal{O}}$ serves as the self-energy of $\varphi$.[4] Here we implicitly used that the CFT contains a large number $N$ of degrees of freedom, which makes sure that only the two-point function of $\mathcal{O}$ appears in the self-energy. This two-point function follows from the AdS/CFT correspondence using the procedure described in the previous subsection.

We note that the picture to keep in mind is a condensed-matter system that is described by elementary bosons corresponding to $\varphi$ and collective variables thereof. Consistent with this viewpoint, the composite operator $\mathcal{O}$ should then be interpreted as such a collective variable, which contains $\varphi$. According to the discussion in Ref. [2], this self-consistent picture imposes a fixed relation between the source of the scalar field and the free mass parameter, which in the present case is given by $M_0^2/\phi_s = 2\pi$, see appendix 5.A for details.

#### 5.2.3.1 Dynamical-source model

Similar to what was done in Ref. [81] for chiral fermions and in Ref. [2] for Dirac fermions, we can derive the semiholographic Green's function in

[4] Note, however, that $\Sigma$ has units of energy squared. This is because to define the nonrelativistic Green's function, we need a wavefunction renormalization factor which is dimensionful, as opposed to the one in the fermionic case.

eq. (5.19) from a dynamical-source model. In order to do so, we start with the holographic contribution to the effective action given in eq. (5.15), which is defined on a UV brane at a fixed radial coordinate $r = r_0$. We then add a free action for the source $\sigma_s$ on the UV brane that we write as

$$S_{UV} = -Z r_0^{-2\Delta_-} \int_{r=r_0} \mathrm{d}^4x \sqrt{-h} \left( |D\sigma_s|^2 + \tilde{M}_0^2 |\sigma_s|^2 \right), \tag{5.20}$$

where we extracted a factor of $r_0^{-2\Delta_-}$ so that $Z$ is dimensionless. Consequently, the total effective boundary action becomes

$$S_{\text{eff}} = -Z r_0^{2\nu-2} \int \frac{\mathrm{d}^4k}{(2\pi)^4} \sigma_s^*(k) \left( K^2 + \tilde{M}_0^2 r_0^2 - \frac{g_b}{Z} r_0^{2-2\nu} G_{\mathcal{O}} \right) \sigma_s(k), \tag{5.21}$$

where we used that $\sqrt{-h} \simeq r_0^4$ and $qA_t \simeq \mu$ for $r_0$ near the boundary and that $4 - 2\Delta_- = 2\nu$. To obtain a canonically normalized kinetic term, we then rescale the source as $\sigma_s \to r_0^{1-\nu}/\sqrt{Z}\sigma_s \equiv \varphi$. Subsequently, we take the limit

$$r_0 \to \infty, \qquad g_b \to 0, \qquad \tilde{M}_0 \to 0, \tag{5.22}$$

such that

$$g^2 \equiv \frac{g_b}{Z} r_0^{2-2\nu} = \text{const.}, \qquad M_0 \equiv \tilde{M}_0 r_0 = \text{const.} \tag{5.23}$$

The effective action then becomes

$$S_{\text{eff}} = -\int \frac{\mathrm{d}^4k}{(2\pi)^4} \varphi^*(k) G_R(k)^{-1} \varphi(k), \tag{5.24}$$

with $G_R$ as in eq. (5.19).

#### 5.2.3.2 Sum rule

The retarded Green's function $G_R(\omega, \mathbf{k})$ in eq. (5.19) corresponds to an elementary scalar field $\varphi$. To demonstrate the sum rule, we use the case where the background is given by a pure anti-de Sitter spacetime as an example, where there is also no deformation by temperature, chemical potential or mass. The holographic Green's function is then given by [60]

$$G_{\mathcal{O}}^{\text{AdS}}(k) = 2\nu \left( \frac{k}{2} \right)^{2\nu} \frac{\Gamma(-\nu)}{\Gamma(\nu)}, \tag{5.25}$$

with $k^2 = -(\omega + i\epsilon)^2 + |\mathbf{k}|^2$. This yields the retarded Green's function

$$G_R^{\mathrm{AdS}}(k) = \frac{1}{k^2 + \tilde{g}k^{2\nu}}, \tag{5.26}$$

with

$$\tilde{g} \equiv g^2 2^{1-2\nu} \frac{\Gamma(1-\nu)}{\Gamma(\nu)}. \tag{5.27}$$

Using the similarity to eq. (3.15) in Ref. [81], we conclude that $G_R$ has no poles in the upper half-plane if we restrict ourselves to $\nu \in (0,1)$. This corresponds to tachyonic masses in the range $m_\sigma^2 \in (-4,-3)$. In this range we also automatically have that $\tilde{g} > 0$, although it should be noted that we already anticipated this result by restricting ourselves to $g_b/Z > 0$ when we defined $g^2$. Defining the spectral function $\rho(\omega,\mathbf{k}) = \operatorname{Im} G_R(\omega,\mathbf{k})/\pi$, it therefore follows that

$$\int \mathrm{d}\omega\, \omega \rho^{\mathrm{AdS}}(\omega,\mathbf{k}) = 1. \tag{5.28}$$

The necessary factor of $\omega$ follows from dimensional analysis and is consistent with the canonical commutation relation $[\dot{\varphi}^*(\mathbf{x}), \varphi(\mathbf{x}')] = i\delta(\mathbf{x}-\mathbf{x}')$ of an elementary scalar field $\varphi$, where the dot denotes a time derivative. We remark that $\rho^{\mathrm{AdS}}$ itself integrates to 0 as it is odd in $\omega$.

The above sum rule should also hold for more general gravitational backgrounds when using $\nu \in (0,1)$, provided we do not introduce any poles in the upper half-plane. Although this is generally difficult to check analytically, we will always check this by numerical integration when needed.

## 5.3 Bosonic spectral functions

What we should first of all demonstrate is that the spectra obtained from the procedure above indeed resemble those of strongly interacting massive Klein-Gordon fields. This implies that not only the semiholographic, but also the holographic spectral function should be gapped, as the self-energy should contain the effect of the strong interactions between massive bosons. In this section we therefore start by studying the appearance of this gap by firstly calculating the undoped holographic spectra, found from the holographic Green's function in eq. (5.16), which corresponds to the semiholographic self-energy. We furthermore study the holographic spectral functions

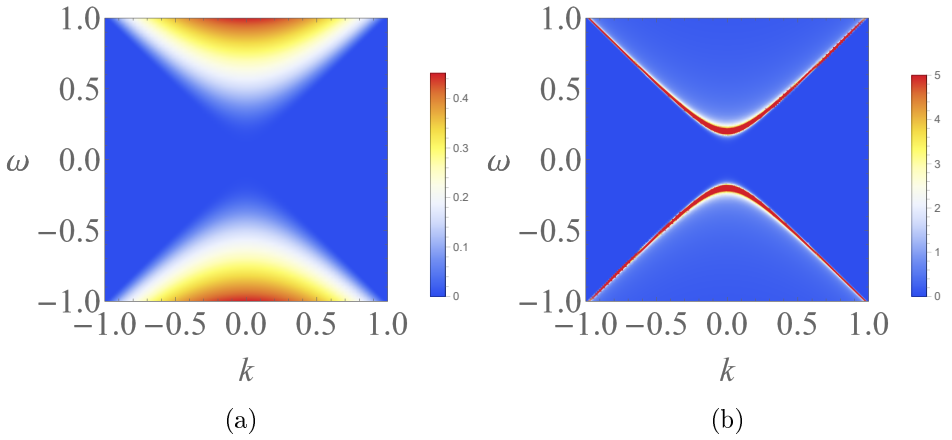


Figure 5.1: The absolute value of the holographic spectral function in standard (a) and alternative (b) quantization, for $m^2 = -3.5$. Here, and in all following plots in this section, all quantities are made (scale) dimensionless by dividing by the appropriate power of $M_0$ and we use $T/M_0 = 1/100$.

in alternative quantization, where $\sigma_v$ plays the role of the source instead.[5] The latter can also be found from the semiholographic spectral functions in the limit $g \to \infty$. We then proceed by moving to finite $g$ and studying the semiholographic spectral functions. The resulting spectra in the case of zero doping are shown in Fig. 5.1 and indeed show the desired gap. We thus find that the deformation in the CFT by the scalar field $\phi$ is sufficient to gap the bosonic spectra, as opposed to the fermionic spectra in Ref. [2] where an additional Yukawa coupling of the probe Dirac fields to $\phi$ was required. Therefore our holographic spectra without doping only depend on temperature and the parameter $m_\sigma^2$.

We investigate the dependence of the gap on the parameter $m_\sigma^2$ by studying the position of the peak at zero momentum that appears in the holographic spectrum in alternative quantization. The result is shown in Fig. 5.2. Most importantly, we observe that the gap is present for all allowed values of the bulk mass of the probe scalar. We furthermore see that for more negative $m_\sigma^2$ the position of the peak shifts to higher frequencies and the width increases.

[5] This is only possible in the range $m_\sigma^2 \in (-4, -3)$. Moreover, we need a boundary action different from eq. (5.14) for this.

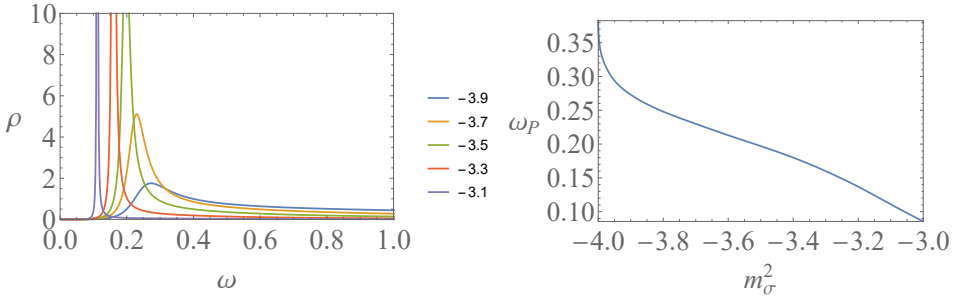


(a) (b)

Figure 5.2: (a) The holographic spectral function in alternative quantization at zero momentum, where the legend shows the used value of $m_\sigma^2$. The spectral functions are antisymmetric in frequency due to particle-hole symmetry. (b) The $m_\sigma^2$-dependence of the position of the peak maximum $\omega_P$ in the spectra.

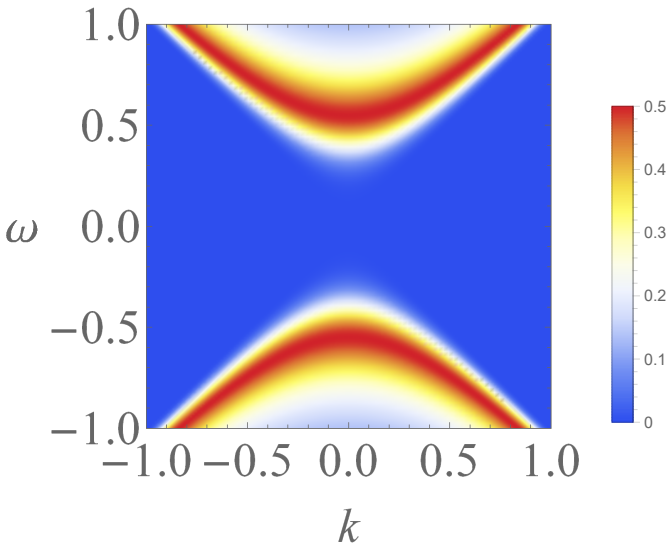


Figure 5.3: The absolute value of the semiholographic spectral function for $m_\sigma^2 = -3.5$ and $g = 1$.

Moving on to finite $g$, we see that the semiholographic spectral function in Fig. 5.3 contains a gap that is renormalized to a value smaller than $M_0$. As we have seen in Fig. 5.1, the same occurs in the limit $g \to \infty$ for any value of $m_\sigma^2$. To see whether this is generic, we calculate the spectral functions at zero momentum for several values of $m_\sigma^2$ and $g$. The result of this calculation is shown in Fig. 5.4. What we observe here is that for bulk mass values near $m_\sigma^2 = -3$, as in Fig. 5.4a, the peak position as a function of $g$ indeed monotonically decreases from $M_0$, approaching the value shown in Fig. 5.2b. However, this is no longer true for values of $m_\sigma^2$ closer to the BF bound. Here, the peak shifs to higher frequencies for small $g$. After this, the peaks in Fig. 5.4b shift to lower frequencies again and approach the value shown in Fig. 5.2b. Alternatively, for masses very close to the BF bound $m_\sigma^2 = -4$ the peak may continue to move to higher frequencies as in Fig. 5.4c, while at the same time a second peak appears near the value shown in Fig. 5.2b. At some $g$, the maximum spectral weight of this second peak exceeds that of the first peak, causing the discontinuity in Fig. 5.4d. In short, we find that the peak location does not necessarily renormalize to a value smaller than $M_0$ for any $g$. Contrarywise, we also observe that the low-frequency interval of the spectral functions with negligible spectral weight generally shrinks, with an upper limit that does renormalize to a value smaller than $M_0$, due to the large width of the peaks. Hence, the holographic interactions always reduce the size of the gap.

Band structures in condensed matter often have an effective description in terms of Dirac theory, where the speed of light plays the role of the Fermi velocity. For the bosonic spectra obtained in this section, such an interpretation as an effective description of a nonrelativistic condensed-matter system is less obvious. It may therefore be unsurprising that as opposed to the spectra obtained in Ref. [2], our spectra do not exhibit exotic features such as a critical coupling $g$ at which the boson becomes effectively massless. Nonetheless, we can still hope to obtain nonrelativistic physics from our model using the method described in Ref. [3]. This means we introduce a chemical potential to bring the bottom of the particle band near $\omega = 0$ and subsequently take the nonrelativistic limit to decouple the antiparticle part of the spectrum. The fact that our spectra always contain a gap is therefore very promising, as this is crucial to be able to apply said method.

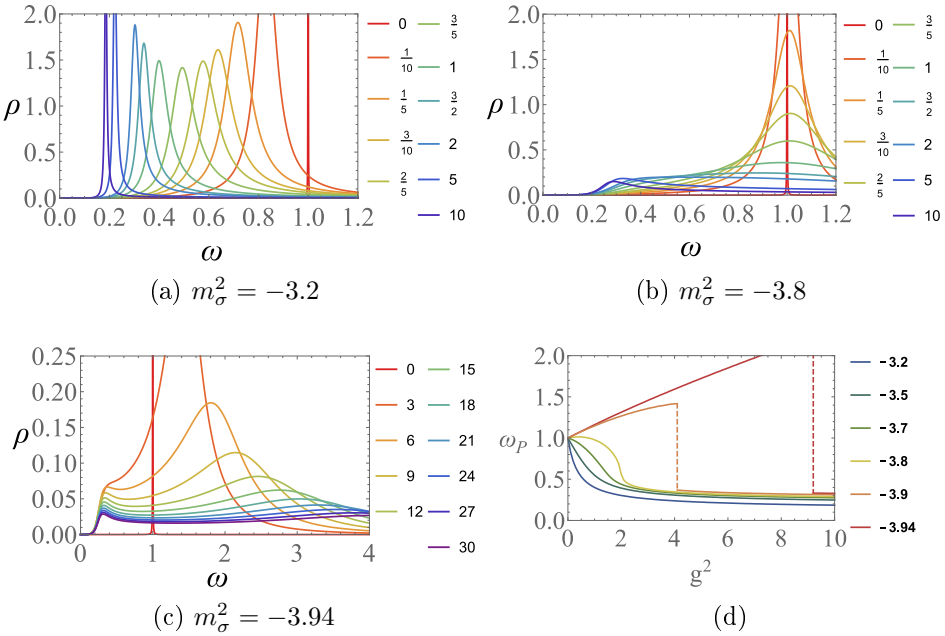


Figure 5.4: (a)-(c) The semiholographic spectral function at zero momentum for several values of $m_\sigma^2$. The legends show the value of $g$. (d) The position of the peak in the spectral functions as a function of $g^2$, where the legend shows the value of $m_\sigma^2$. The value of $\omega_P$ shown here corresponds to the frequency at which the spectral function has its global maximum.

## 5.4 Doped spectra and outlook

Our next mission is to study the spectral functions of $\varphi$ with $\mu > 0$. The effect of a nonzero chemical potential is that it breaks the particle-hole symmetry.[6] As we work grand canonically, the spectrum will appear to have shifted down in frequency. Similar to the procedure in Ref. [3], we can then attempt to define a nonrelativistic chemical potential $\mu_{\mathrm{NR}}$ with respect to the bottom of the particle band in the spectrum. This means that at $\mu_{\mathrm{NR}} = 0$ and $T = 0$ the spectrum should have a delta-peak at $(\omega, \mathbf{k}) = (0, \mathbf{0})$.

In pursuit of this goal we therefore study the behavior of $\mu^*(T, g)$, which

[6] This symmetry implies that for $\mu = 0$ we have that $\rho(\omega, \mathbf{k}) = \rho(-\omega, \mathbf{k})$, which is a consequence of the initial condition in eq. (5.17).

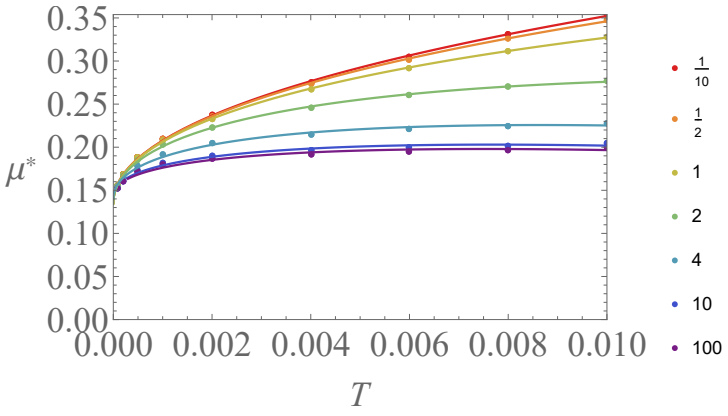


Figure 5.5: The behavior of $\mu^*/M_0$, at which the semiholographic Green's function contains a pole, as a function of $T/M_0$. Here we fixed $m_\sigma^2 = -3.5$ and $q = 3$. The legend shows the value of $g$. Here the dots are the values we computed, whereas the curves show a fit to $\mu^* = \alpha + \beta\sqrt{T} + \gamma T$, where the three coefficients depend on $g$.

we define as the value of the chemical potential $\mu$ at which such a delta-peak occurs. At this value, the semiholographic Green's function in eq. (5.19) should have a pole. We therefore plot the first positive value of $\mu$ at which the inverse Green's function at zero frequency and momentum vanishes in Fig. 5.5, for fixed bulk parameters $m_\sigma^2 = -3.5$ and $q = 3$. Although $\mu^*$ does seem to converge to a nonzero value at $T = 0$, its temperature dependence is rather peculiar. In particular, as shown in the figure, $\mu^*$ seems to behave approximately as $\mu^*(T) - \mu^*(T = 0) \propto \sqrt{TM_0}$ at low temperatures. Restoring SI units then reveals that this is proportional to the speed of light $c$. This makes it very hard to define the nonrelativistic chemical potential, as it seems that even in the nonrelativistic limit where $T \ll M_0$, a small change in temperature leads to a very large difference in the position of the pole as $c \to \infty$.

Another curious property of $\mu^*$ in Fig. 5.5 is that for small $g$, it does not seem to converge to $\mu^* = M_0$. To investigate why this behavior occurs, we first note that the position of the pole in the Green's function is given by the solution of

$$G_{\mathcal{O}}(0; \mu^*) = \frac{M_0^2 - \mu^{*2}}{g^2}, \tag{5.29}$$

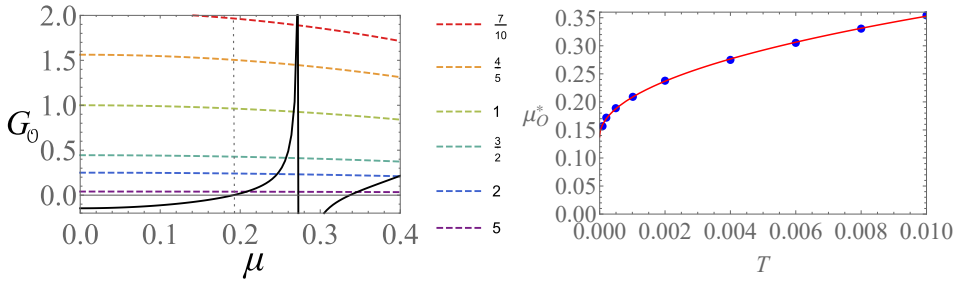


(a) (b)

Figure 5.6: (a) The Green's function $G_{\mathcal{O}}$ as a function of $\mu/M_0$ (black curve) for $T/M_0 = 1/250$, $q = 3$ and $m_\sigma^2 = -3.5$. Here the dashed curves are given by the right-hand side of eq. (5.29), where the legend shows the value of $g$. The vertical dotted line shows the value of the smallest root of $G_{\mathcal{O}}$. (b) The lowest value of the chemical potential at which the self-energy at zero frequency and momentum has a pole, as a function of the temperature for $q = 3$ and $m_\sigma^2 = -3.5$. The fit in red is given by $\mu^*_{\mathcal{O}} \simeq 0.14M_0 + 2.3\sqrt{TM_0} - 1.2T$.

where the left-hand side is evaluated at $(\omega, \mathbf{k}) = (0, \mathbf{0})$ and does not depend on $g$. The value of the Green's function of $\mathcal{O}$ as a function of $\mu$ is shown in Fig. 5.6a for a fixed temperature of $T/M_0 = 1/250$. The right-hand side of eq. (5.29) is shown in this figure as well, for several values of $g$. Hence, $\mu^*$ follows by reading off the first intersection of the dashed curves with the black curve. The most outstanding feature in this plot is the pole in the Green's function $G_{\mathcal{O}}$, which occurs at some value $\mu = \mu^*_{\mathcal{O}}$. This pole resembles the one that occurs in the Green's function of the order parameter fluctuations in the holographic superconductor when approaching the critical point from the normal phase. As opposed to the holographic superconductor case, here we have an additional scale in our system set by $M_0$, so that $\mu^*_{\mathcal{O}}$ is not necessarily proportional to the temperature, as is shown in Fig. 5.6b.

The above-mentioned pole at $\mu^*_{\mathcal{O}}$ acts as an upper bound for $\mu^*$ that is independent of $g$. This easily follows from the fact that $G_{\mathcal{O}} < 0$ for $\mu = 0$, as can be seen from Fig. 5.6a.[7] Since for all $g$ the right-hand side of eq. (5.29) is positive at $\mu = 0$ and vanishes at $\mu = M_0 > \mu^*_{\mathcal{O}}$, any dashed curve in Fig. 5.6a indeed has to intersect $G_{\mathcal{O}}$ at some $\mu^* < \mu^*_{\mathcal{O}}$. This is true for

[7] We have checked that this is true for any value of $m_\sigma^2$.

any nonzero $g$, which explains why we do not observe the convergence to $\mu^* = M_0$ for small $g$. Moreover, the large-$g$ behavior of $\mu^*$ in Fig. 5.5 is also explained by Fig. 5.6a, where we see that it approaches the value at which $G_{\mathcal{O}}$ vanishes, denoted by the vertical dotted line. This also follows immediately from inspecting eq. (5.29).

The above analysis shows that the strange behavior of $\mu^*$ is mainly caused by the existence and the behavior of the pole of $G_{\mathcal{O}}$. This makes it complicated to find a suitable definition of the nonrelativistic chemical potential. Such a definition and the subsequent study of the nonrelativistic regime is left for future work. For now, we remark that a possible direction is to see whether we can define a nonrelativistic chemical potential depending on temperature. Alternatively, we may have to define $\mu^*$ using a solution of eq. (5.29) at a higher $\mu$, although we note that $G_{\mathcal{O}}$ has more poles there. Finally, we can tune the bulk parameters, in particular $q$, to see if this leads to a more favorable behavior of the self-energy.

## 5.A RG equations

In this work we fixed the ratio of the source $\phi_s$ of the scalar field in the gravitational background and the square of the bare mass parameter $M_0^2$ that appears in the UV action in eq. (5.20) to $\alpha \equiv M_0^2/\phi_s = 2\pi$. We remark that it is principle possible to regard $\alpha$ as a free parameter in the semiholographic Green's function and that the value of $\alpha$ does not affect the result in the holographic limit $g \to \infty$. In this section we present an argument for the specific value of $\alpha$ quoted above.

From the equations of motion for the background in eqs. (5.4)-(5.7), we can derive that near the boundary the scalar field behaves as

$$\phi = \phi_s r^{-2} \log r + \phi_v r^{-2} + \cdots . \tag{5.30}$$

We now consider a rescaling $r \to \lambda r$ so that $\phi$ becomes

$$\phi \to \phi_s(\lambda)\lambda^{-2} r^{-2} (\log r + \log \lambda) + \phi_v(\lambda)\lambda^{-2} r^{-2} + \dots . \tag{5.31}$$

However, $\phi$ is invariant under such a rescaling. Hence, from comparing the coefficients in the above equations of $r^{-2}$ and $r^{-2}\log r$ we find

$$\phi_s(\lambda) = \phi_s \lambda^2, \tag{5.32}$$

$$\phi_v(\lambda) = \phi_v \lambda^2 - \phi_s \lambda^2 \log \lambda. \tag{5.33}$$

This lead to the following RG equations for $\phi_{s,v}$:

$$\lambda \frac{\mathrm{d}\phi_s(\lambda)}{\mathrm{d}\lambda} = 2\phi_s(\lambda), \tag{5.34}$$

$$\lambda \frac{\mathrm{d}\phi_v(\lambda)}{\mathrm{d}\lambda} = 2\phi_v(\lambda) - \phi_s(\lambda). \tag{5.35}$$

The second of these equations contains a nontrivial term that originates from the logarithm in eq. (5.33).

Moreover, using the two-point function found from the semiholographic effective action in eq. (5.19), we have that

$$\left\langle |\varphi(x)|^2 \right\rangle = \int \frac{\mathrm{d}^4 k_E}{(2\pi)^4} \frac{1}{k_E^2 + M_0^2 - g^2 G_{\mathcal{O}}} \tag{5.36}$$

where $k_E^2 = |\mathbf{k}|^2 + k_4^2$ with $k_4 = i\omega$. To derive the RG equation for $\left\langle |\varphi|^2 \right\rangle$ we introduce a UV cut-off $\Lambda$ and subsequently integrate over the high-momentum shell $|k_E| \in (\Lambda, e^{-l}, \Lambda)$, where $l > 0$. For these high momenta we expand the integrand above as

$$\left\langle |\varphi(x)|^2 \right\rangle = \int_\Lambda \frac{\mathrm{d}^4 k_E}{(2\pi)^4} \frac{1}{k_E^2} \left(1 - \frac{M_0^2 - g^2 G_{\mathcal{O}}}{k_E^2}\right) + \dots . \tag{5.37}$$

Here the dots contain the integration over lower momenta and we used that for high momenta $k_E^2$ always dominates the Green's function $G_{\mathcal{O}}$. Evaluating the logarithmically divergent term yields

$$\left\langle |\varphi(x)|^2 \right\rangle = \dots - \frac{M_0^2}{8\pi^2} \int_{\Lambda e^{-l}}^{\Lambda} \frac{\mathrm{d}k_E}{k_E} = \dots - \frac{M_0^2 l}{8\pi^2} \tag{5.38}$$

where we used $\mathrm{d}^4 k_E = 2\pi^2 k_E^3 \mathrm{d}k_E$. This then leads to

$$\frac{\mathrm{d}\left\langle |\varphi(x)|^2 \right\rangle}{\mathrm{d}l} = \dots - \frac{M_0^2}{8\pi^2}. \tag{5.39}$$

In terms of $\alpha$ as defined in the beginning of this appendix, this yields[8]

$$\frac{\mathrm{d}\phi_v}{\mathrm{d}l} = \dots - \frac{\alpha^2 \phi_s}{4\pi^2}, \tag{5.40}$$

which gives $\alpha = \pm 2\pi$ after comparing with eq. (5.35). We pick $\alpha = 2\pi$ as $\phi_s$ is positive in our numerical calculations.

[8] Here we use the on-shell Klein-Gordon action for $\phi$.

# 6 Nederlandse samenvatting

In de theoretische natuurkunde proberen we systemen uit de natuur te begrijpen door ze te vertalen naar wiskundige modellen. Zoals de titel al aangeeft, is dit proefschrift hierop geen uitzondering. De systemen die we hier willen beschrijven zijn extreem koude gassen, die bestaan uit atomen die sterke wisselwerkingen met elkaar hebben. Deze systemen willen we vertalen naar een vrij speciaal soort modellen, die ook wel bekendstaan als holografische modellen.

## Ultrakoude gassen met ultrasterke wisselwerkingen

Laten we eerst wat meer ingaan op de systemen die we willen beschrijven. Dit zijn ultrakoude gassen met typische temperaturen variërend van enkele nanokelvins tot enkele microkelvins. Dat is grofweg een paar miljard keer zo klein als de temperatuur uit het weerbericht van vandaag.[1] Wat er zo speciaal is aan deze ultrakoude gassen, is de grote mate van controle die onze experimentele collega's over ze hebben. In het bijzonder is het relatief eenvoudig om de effectieve interacties tussen de atomen in zo'n gas in te stellen. Dit komt doordat de interacties in deze gassen door slechts één parameter worden bepaald: de zogenaamde verstrooiingslengte.[2] De effectieve waarde van die verstrooiingslengte kan experimenteel worden aangepast door een magnetisch veld aan te leggen. Dit maakt het mogelijk om ultrakoude atomen met zeer sterke wisselwerkingen te bestuderen. Er bestaat in het bijzonder een specifieke waarde van het magnetische veld waarop een resonantie optreedt, wat betekent dat de verstrooiingslengte oneindig groot wordt. We spreken dan van *unitaire* gassen of atomen. In dit proefschrift zoeken we naar een holografische beschrijving van zulke ultrakoude unitaire gassen.

[1] Ervan uitgaande dat er vandaag geen records worden verbroken, ligt de temperatuur tussen de 184 Kelvin en 330 Kelvin.

[2] Dit is een gevolg van de lage temperatuur van het gas. Zie de introductie in hoofdstuk 1 voor meer details.

## Gassen als hologrammen

Met een holografische beschrijving bedoelen we simpelweg dat we een model opstellen met behulp van een techniek die holografie heet. Bij dit woord denken we natuurlijk meteen aan hologrammen, zoals die op onze creditcards of uit series als Star Trek. Een definiërende eigenschap van zulke hologrammen is dat ze een driedimensionaal object afbeelden op een tweedimensionaal oppervlak. Met andere woorden, het driedimensionale object en het tweedimensionale oppervlak bevatten dezelfde informatie.

In dit proefschrift bestuderen we iets soortgelijks: we kijken naar twee systemen die dezelfde informatie bevatten, terwijl een van deze systemen een extra dimensie heeft. Toch is de holografie die we hier gebruiken van een net iets andere soort. Ze is namelijk gebaseerd op het zogenaamde *holografische principe* van de kwantumzwaartekracht. Dit principe[3] postuleert dat er een dualiteit bestaat tussen twee fysische systemen, namelijk een systeem met zwaartekracht in $d+1$ dimensies en eentje zonder zwaartekracht in $d$ dimensies. Zo'n dualiteit houdt in dat deze twee theorieën dezelfde fysica beschrijven en dus dezelfde fysische informatie bevatten. Vanwege het verschil in dimensies zou je het $d$-dimensionale systeem dus kunnen zien als een soort holografische afbeelding van het $d+1$-dimensionale systeem.

In dit proefschrift gebruiken we dit principe om modellen voor ultrakoude gassen te op te stellen. Grof gezegd gaan we ervan uit dat we deze gassen, die net als wij in drie dimensies leven, kunnen zien als holografische afbeeldingen van bepaalde gravitationele duale systemen in vier dimensies,[4] in overeenstemming met het bovenstaande holografische principe. Het uiteindelijke doel is dan om die gravitationele dualen te vinden. Met andere woorden, we stellen modellen op voor bepaalde zwaartekrachttheorieën die op het eerste gezicht in de verste verte niet lijken op ultrakoude gassen. Echter, dankzij de holografische dualiteit kunnen we uit deze modellen toch informatie halen over de fysische eigenschappen van ultrakoude atomen.

Unitaire gassen lijken om meerdere redenen een perfecte kandidaat voor een aanpak gebaseerd op holografie. Ten eerste geeft het holografische principe een dualiteit tussen een theorie met sterke interacties en eentje met

[3] Om preciezer te zijn: we maken we in dit proefschrift gebruik van een van de bekendste voorbeelden van het holografische principe, namelijk de *AdS/CFT-correspondentie*.

[4] Hiermee bedoelen we ruimtelijke dimensies. Het systeem met zwaartekracht leeft dus in een vijfdimensionale ruimtetijd.

zwakke interacties. Aangezien zoals hierboven gezegd de interatomaire wisselwerkingen in unitaire gassen zeer sterk zijn, betekent dit dat we een duale zwaartekrachttheorie moeten opstellen waar de wisselwerkingen zeer zwak zijn. Dit is voordelig, omdat het meestal erg moeilijk is om berekeningen uit te voeren voor systemen met sterke interacties. Daarentegen weten we precies hoe we met systemen met zwaartekracht en zwakke interacties om moeten gaan. Dit soort systemen wordt namelijk beschreven door Einsteins algemene relativiteitstheorie, de theorie die de werking van zwaartekracht beschrijft als een kromming van de ruimtetijd. Uit deze theorie volgen exotische[5] voorspellingen voor ons universum, zoals het bestaan van zwarte gaten en de recent waargenomen zwaartekrachtgolven. Wij gebruiken de relativiteitstheorie echter niet om een accurate beschrijving van ons universum te geven, maar om een duale theorie voor unitaire gassen te vinden. De modellen die we hiertoe opstellen zijn nog veel exotischer, dat wil zeggen, zeer verschillend van ons eigen universum.[6] Ondanks die verschillen kunnen we gelukkig nog steeds gebruik maken van de algemene relativiteitstheorie, maar dan toegepast op net wat andere universa dan het onze.

Daarnaast beschrijft holografie universele eigenschappen van schaalinvariante systemen, of deformaties daarvan. Ultrakoude unitaire gassen vertonen precies zulk universeel gedrag, met andere woorden, de fysische eigenschappen hangen niet af van het type atomen dat wordt gebruikt. Verder zijn ze bijna schaalinvariant, in die zin dat de enige schalen die voorkomen in het systeem worden gegeven door de dichtheid en de temperatuur van het gas.

Ondanks het feit dat unitaire gassen bij uitstek geschikt lijken voor de holografische methode, is het niet triviaal om zomaar een holografisch model ervoor op te schrijven. Dit blijkt wel uit het feit dat dit proefschrift zo'n honderd pagina's aan onderzoek bevat. Hoewel we hierin uiteindelijk een aantal eigenschappen van zulke gassen kwalitatief weten te reproduceren, vormen de hoofdstukken van dit proefschrift slechts een stap in de richting van zulke modellen. We zullen nu kort ingaan op de inhoud deze hoofdstukken.

[5] Hoewel dit woord vaak met warme landen wordt geassocieerd, is de typische temperatuur van zwarte gaten in theorie vaak nog kleiner dan die van ultrakoude gassen.

[6] Ze bevatten bijvoorbeeld zwarte gaten die er uitzien als een plat vlak. Verder beschrijven ze een universum met vier ruimtelijke dimensies in plaats van drie. Ten slotte hebben ze een negatieve kosmologische constante. De kosmologische constante is een grootheid uit de relativiteitstheorie en bestaat ook in ons eigen universum, maar daar heeft ze een positieve waarde volgens de recente kosmologische observaties.

## Supergeleiding en zwarte gaten

Een van de eerste toepassingen van holografie is een model voor supergeleiding, het verschijnsel waarbij een elektrische stroom zonder weerstand wordt geleid. In hoofdstuk 2 bestuderen we dit model, dat bekendstaat als de holografische supergeleider. Het gravitationele duale systeem van deze supergeleiders bestaat uit het 'standaard' zwaartekrachtsysteem van de holografie,[7] dat gedeformeerd is om een supergeleider met een temperatuur en een dichtheid te kunnen beschrijven.[8] Deze twee ingrediënten, een temperatuur en een dichtheid dus, zullen uiteindelijk ook voorkomen in de modellen die we willen gebruiken voor de beschrijving van een unitair gas.

## Massa kweken

Naast de twee bovengenoemde ingrediënten hebben wij nog een derde nodig. Een atoomgas bestaat namelijk uit deeltjes met een massa. In hoofdstuk 3 laten we zien hoe we zo'n massa kunnen incorpereren in een holografisch model. Verder gaan we hier in op hoe we met holografie elementaire deeltjes zoals atomen[9] kunnen beschrijven.

## Weg met de relativiteit

Nu we een massa geïntroduceerd hebben, hebben we ook een extra energieschaal in ons model. Dit is een gevolg van Einsteins wereldberoemde formule uit zijn speciale relativiteitstheorie, namelijk $E = mc^2$, waar $E$ de energie, $m$ de massa en $c$ de lichtsnelheid is. Deze energieschaal komt typisch niet voor in de beschrijving van ultrakoude gassen, omdat de lichtsnelheid daar kan worden beschouwd als zijnde oneindig. Dit betekent met andere woorden dat de correcties als gevolg van het feit dat de lichtsnelheid eindig is, oftewel de relativistische correcties, verwaarloosbaar zijn in deze systemen.

[7] Dit is de zogenaamde Anti-de Sitter-ruimtetijd.

[8] Naast deze twee ingrediënten bevat de holografische supergeleider nog een extra deformatie. Deze is nodig om de overgang van een normaal naar een supergeleidend materiaal te beschrijven.

[9] Een atoom bestaat natuurlijk uit allerlei subatomaire deeltjes en is in die zin dus niet echt elementair. De energie die nodig is om een atoom te ontbinden is echter groot genoeg om dit detail te kunnen verwaarlozen.

We moeten daarom in onze holografische modellen ook het gebied bekijken waar deze extra energieschaal oneindig groot is ten opzichte van alle andere energieschalen in ons model. Hoe we dit precies doen is het onderwerp van hoofdstuk 4. Ook reproduceren we hier een aantal kwalitatieve eigenschappen van unitaire gassen die zijn waargenomen in experimenteel geprepareerde gassen.

## Instabiele tegenhangers

Om koude microscopische systemen[10] zoals ultrakoude gassen te beschrijven, gebruiken we in de natuurkunde de wetten van de zogenaamde kwantummechanica. Volgens deze wetten bestaan er ruwweg twee soorten deeltjes die zich net wat anders gedragen, namelijk bosonen en fermionen. Het meeste onderzoek in dit proefschrift gaat over unitaire gassen die bestaan uit fermionische atomen. Een reden hiervoor is dat experimenteel geprepareerde bosonische unitaire gassen vaak instabiel blijken. Desalniettemin wordt er nog steeds veel onderzoek gedaan naar de realisatie van zulke gassen, wat voor ons een reden is om ook hiervoor holografische modellen op te stellen. De eerste stappen in deze richting zijn te vinden in hoofdstuk 5.

[10] Preciezer gezegd, systemen waarvan de thermische golflengte een grootte heeft die vergelijkbaar is met of groter is dan de gemiddelde afstand tussen de microscopische deeltjes. Deze thermische golflengte hangt af van de temperatuur en wordt groter naarmate de temperatuur lager wordt.

# Bibliography


[1] N. W. M. Plantz, H. T. C. Stoof, and S. Vandoren, Journal of Physics B: Atomic, Molecular and Optical Physics **50**, 064001 (2017).

[2] N. W. M. Plantz, F. García Flórez, and H. T. C. Stoof, Journal of High Energy Physics **2018**, 123 (2018).

[3] N. W. M. Plantz and H. T. C. Stoof, (2018), arXiv:1810.09759 [cond-mat.quant-gas] .

[4] G. 't Hooft, *Conference on Highlights of Particle and Condensed Matter Physics (SALAMFEST)*, Conf. Proc. **C930308**, 284 (1993).

[5] L. Susskind, J. Math. Phys. **36**, 6377 (1995).

[6] J. Maldacena, International Journal of Theoretical Physics **38**, 1113 (1999).

[7] T. Kovachy, J. M. Hogan, A. Sugarbaker, S. M. Dickerson, C. A. Donnelly, C. Overstreet, and M. A. Kasevich, Physical Review Letters **114**, 143004 (2015).

[8] A. E. Leanhardt, T. A. Pasquini, M. Saba, A. Schirotzek, Y. Shin, D. Kielpinski, D. E. Pritchard, and W. Ketterle, Science **301**, 1513 (2003).

[9] H. Stoof, D. Dickerscheid, and K. Gubbels, *Ultracold Quantum Fields*, Theoretical and Mathematical Physics (Springer Netherlands, 2014).

[10] V. Efimov, Phys. Lett. **33B**, 563 (1970).

[11] F. Chevy and C. Salomon, Journal of Physics B: Atomic, Molecular and Optical Physics **49**, 192001 (2016).

[12] P. Naidon and S. Endo, Rept. Prog. Phys. **80**, 056001 (2017).

[13] T. Kraemer, M. Mark, P. Waldburger, J. G. Danzl, C. Chin, B. Engeser, A. D. Lange, K. Pilch, A. Jaakkola, H.-C. Nägerl, and R. Grimm, Nature **440**, 315 (2006).

[14] M. Zaccanti, B. Deissler, C. D'Errico, M. Fattori, M. Jona-Lasinio, S. Müller, G. Roati, M. Inguscio, and G. Modugno, Nature Physics **5**, 586 (2009).

[15] B. S. Rem, A. T. Grier, I. Ferrier-Barbut, U. Eismann, T. Langen, N. Navon, L. Khaykovich, F. Werner, D. S. Petrov, F. Chevy, and C. Salomon, Phys. Rev. Lett. **110**, 163202 (2013).

[16] U. Eismann, L. Khaykovich, S. Laurent, I. Ferrier-Barbut, B. S. Rem, A. T. Grier, M. Delehaye, F. Chevy, C. Salomon, L.-C. Ha, and C. Chin, Phys. Rev. X **6**, 021025 (2016).

[17] R. J. Fletcher, A. L. Gaunt, N. Navon, R. P. Smith, and Z. Hadzibabic, Phys. Rev. Lett. **111**, 125303 (2013).

[18] P. Makotyn, C. E. Klauss, D. L. Goldberger, E. A. Cornell, and D. S. Jin, Nature Physics **10**, 116 (2014).

[19] C. Eigen, J. A. P. Glidden, R. Lopes, N. Navon, Z. Hadzibabic, and R. P. Smith, Phys. Rev. Lett. **119**, 250404 (2017).

[20] R. Duine and H. Stoof, Physics Reports **396**, 115 (2004).

[21] E. Tiesinga, B. J. Verhaar, and H. T. C. Stoof, Phys. Rev. A **47**, 4114 (1993).

[22] D. Kleppner, Physics Today **57**, 12 (2004).

[23] S. Inouye, M. R. Andrews, J. Stenger, H.-J. Miesner, D. M. Stamper-Kurn, and W. Ketterle, Nature **392**, 151 (1998).

[24] C. A. Regal, M. Greiner, and D. S. Jin, Phys. Rev. Lett. **92**, 040403 (2004).

[25] M. W. Zwierlein, C. A. Stan, C. H. Schunck, S. M. F. Raupach, A. J. Kerman, and W. Ketterle, Phys. Rev. Lett. **92**, 120403 (2004).

[26] Y. Sagi, T. E. Drake, R. Paudel, R. Chapurin, and D. S. Jin, Phys. Rev. Lett. **114**, 075301 (2015).

[27] T. Bourdel, L. Khaykovich, J. Cubizolles, J. Zhang, F. Chevy, M. Teichmann, L. Tarruell, S. J. J. M. F. Kokkelmans, and C. Salomon, Phys. Rev. Lett. **93**, 050401 (2004).

[28] M. Bartenstein, A. Altmeyer, S. Riedl, S. Jochim, C. Chin, J. H. Denschlag, and R. Grimm, Phys. Rev. Lett. **92**, 120401 (2004).

[29] B. A. Olsen, M. C. Revelle, J. A. Fry, D. E. Sheehy, and R. G. Hulet, Phys. Rev. A **92**, 063616 (2015).

[30] T.-L. Ho, Phys. Rev. Lett. **92**, 090402 (2004).

[31] J. Bardeen, L. N. Cooper, and J. R. Schrieffer, Phys. Rev. **106**, 162 (1957).

[32] S. Tan, Annals of Physics **323**, 2971 (2008).

[33] Y. Sagi, T. E. Drake, R. Paudel, and D. S. Jin, Phys. Rev. Lett. **109**, 220402 (2012).

[34] M. J. H. Ku, A. T. Sommer, L. W. Cheuk, and M. W. Zwierlein, Science **335**, 563 (2012).

[35] E. Burovski, E. Kozik, N. Prokof'ev, B. Svistunov, and M. Troyer, Phys. Rev. Lett. **101**, 090402 (2008).

[36] G. E. Astrakharchik, J. Boronat, J. Casulleras, and S. Giorgini, Phys. Rev. Lett. **93**, 200404 (2004).

[37] K. B. Gubbels and H. T. C. Stoof, Phys. Rev. Lett. **100**, 140407 (2008).

[38] S. Piatecki and W. Krauth, Nature Communications **5**, 3503 (2014).

[39] S. Gubser, I. Klebanov, and A. Polyakov, Physics Letters B **428**, 105 (1998).

[40] E. Witten, Adv. Theor. Math. Phys. **2**, 253 (1998).

[41] K. Landsteiner and Y. Liu, Physics Letters B **753**, 453 (2016).

[42] V. L. Ginzburg and L. D. Landau, Zh. Eksp. Teor. Fiz. **20**, 1064 (1950).

[43] L. Gor'kov, Sov. Phys. JETP **9** (1959).

[44] J. R. Schrieffer, *Theory of superconductivity*, Advanced book program (Perseus, Reading, MA, 1999).

[45] E. Burovski, N. Prokof'ev, B. Svistunov, and M. Troyer, Phys. Rev. Lett. **96**, 160402 (2006).

[46] A. Bulgac, J. E. Drut, and P. Magierski, Phys. Rev. Lett. **96**, 090404 (2006).

[47] A. Bulgac, J. E. Drut, and P. Magierski, Phys. Rev. A **78**, 023625 (2008).

[48] S. S. Gubser, Class. Quant. Grav. **22**, 5121 (2005).

[49] S. S. Gubser, Phys. Rev. **D78**, 065034 (2008).

[50] S. A. Hartnoll, C. P. Herzog, and G. T. Horowitz, Phys. Rev. Lett. **101**, 031601 (2008).

[51] G. T. Horowitz, *From Gravity to Thermal Gauge Theories: The AdS/CFT Correspondence*, Lect. Notes Phys. **828**, 313 (2011).

[52] S. A. Hartnoll, C. P. Herzog, and G. T. Horowitz, Journal of High Energy Physics **2008**, 015 (2008).

[53] C. P. Herzog, P. K. Kovtun, and D. T. Son, Phys. Rev. **D79**, 066002 (2009).

[54] J.-H. She, B. J. Overbosch, Y.-W. Sun, Y. Liu, K. Schalm, J. A. Mydosh, and J. Zaanen, Phys. Rev. **B84**, 144527 (2011).

[55] G. T. Horowitz and M. M. Roberts, Journal of High Energy Physics **2009**, 015 (2009).

[56] S. A. Hartnoll, Classical and Quantum Gravity **26**, 224002 (2009).

[57] H. Kleinert, Fortschritte der Physik **26**, 565 (1978).

[58] C. Chin, R. Grimm, P. Julienne, and E. Tiesinga, Rev. Mod. Phys. **82**, 1225 (2010).

[59] M. Bartenstein, A. Altmeyer, S. Riedl, S. Jochim, C. Chin, J. H. Denschlag, and R. Grimm, Phys. Rev. Lett. **92**, 203201 (2004).

[60] D. T. Son and A. O. Starinets, JHEP **09**, 042 (2002).

[61] M. Kaminski, K. Landsteiner, J. Mas, J. P. Shock, and J. Tarrio, JHEP **02**, 021 (2010).

[62] U. Gürsoy, V. Jacobs, E. Plauschinn, H. Stoof, and S. Vandoren, Journal of High Energy Physics **2013**, 127 (2013).

[63] G. Policastro, D. T. Son, and A. O. Starinets, Phys. Rev. Lett. **87**, 081601 (2001).

[64] P. K. Kovtun, D. T. Son, and A. O. Starinets, Phys. Rev. Lett. **94**, 111601 (2005).

[65] J. McGreevy, Adv. High Energy Phys. **2010**, 723105 (2010).

[66] S. Sachdev, "Condensed matter and AdS/CFT," in *From Gravity to Thermal Gauge Theories: The AdS/CFT Correspondence* (Springer Berlin Heidelberg, Berlin, Heidelberg, 2011) pp. 273–311.

[67] D. T. Son, Phys. Rev. D **78**, 046003 (2008).

[68] K. Balasubramanian and J. McGreevy, Phys. Rev. Lett. **101**, 061601 (2008).

[69] S. Kachru, X. Liu, and M. Mulligan, Phys. Rev. D **78**, 106005 (2008).

[70] M. Taylor, (2008), arXiv:0812.0530 [hep-th] .

[71] J. Crossno, J. K. Shi, K. Wang, X. Liu, A. Harzheim, A. Lucas, S. Sachdev, P. Kim, T. Taniguchi, K. Watanabe, T. A. Ohki, and K. C. Fong, Science **351**, 1058 (2016).

[72] M. Henningson and K. Sfetsos, Physics Letters B **431**, 63 (1998).

[73] S.-S. Lee, Phys. Rev. D **79**, 086006 (2009).

[74] H. Liu, J. McGreevy, and D. Vegh, Phys. Rev. D **83**, 065029 (2011).

[75] T. Faulkner, H. Liu, J. McGreevy, and D. Vegh, Phys. Rev. D **83**, 125002 (2011).

[76] M. Čubrović, J. Zaanen, and K. Schalm, Science **325**, 439 (2009).

[77] K. Landsteiner, Y. Liu, and Y.-W. Sun, Phys. Rev. Lett. **116**, 081602 (2016).

[78] V. P. J. Jacobs, S. J. G. Vandoren, and H. T. C. Stoof, Phys. Rev. B **90**, 045108 (2014).

[79] Y. Liu and Y.-W. Sun, (2018), arXiv:1801.09357 [hep-th] .

[80] T. Faulkner and J. Polchinski, Journal of High Energy Physics **2011**, 12 (2011).

[81] U. Gürsoy, E. Plauschinn, H. Stoof, and S. Vandoren, Journal of High Energy Physics **2012**, 18 (2012).

[82] C. Copetti, J. Fernández-Pendás, and K. Landsteiner, Journal of High Energy Physics **2017**, 138 (2017).

[83] G. T. Horowitz and M. M. Roberts, Phys. Rev. D **78**, 126008 (2008).

[84] P. Kovtun and A. Ritz, Phys. Rev. D **78**, 066009 (2008).

[85] V. P. J. Jacobs, S. Grubinskas, and H. T. C. Stoof, Journal of High Energy Physics **2015**, 33 (2015).

[86] V. P. J. Jacobs, P. Betzios, U. Gürsoy, and H. T. C. Stoof, Phys. Rev. B **93**, 195104 (2016).

[87] A. P. Schnyder, S. Ryu, A. Furusaki, and A. W. W. Ludwig, Phys. Rev. B **78**, 195125 (2008).

[88] G. E. Volovik, JETP Letters **91**, 55 (2010).

[89] M. A. Silaev and G. E. Volovik, JETP Letters **95**, 25 (2012).

[90] B. Douçot, C. Ecker, A. Mukhopadhyay, and G. Policastro, Phys. Rev. D **96**, 106011 (2017).

[91] S. A. Hartnoll, D. M. Hofman, and D. Vegh, Journal of High Energy Physics **2011**, 96 (2011).

[92] N. Iqbal, H. Liu, and M. Mezei, Journal of High Energy Physics **2012**, 86 (2012).

[93] J. Zaanen, Y. Liu, Y. Sun, and K. Schalm, *Holographic Duality in Condensed Matter Physics* (Cambridge University Press, 2015).

[94] S. Hartnoll, A. Lucas, and S. Sachdev, *Holographic Quantum Matter*, The MIT Press (MIT Press, 2018).

[95] Y. Liu and Y.-W. Sun, Journal of High Energy Physics **2018**, 189 (2018).

[96] U. Gürsoy, A. Jansen, W. Sybesma, and S. Vandoren, Phys. Rev. Lett. **117**, 051601 (2016).

[97] L. Rammelmüller, A. C. Loheac, J. E. Drut, and J. Braun, Phys. Rev. Lett. **121**, 173001 (2018).

[98] C. Cao, E. Elliott, J. Joseph, H. Wu, J. Petricka, T. Schäfer, and J. E. Thomas, Science **331**, 58 (2011).

[99] J. A. Joseph, E. Elliott, and J. E. Thomas, Phys. Rev. Lett. **115**, 020401 (2015).

[100] S. Nascimbène, N. Navon, K. J. Jiang, F. Chevy, and C. Salomon, Nature **463**, 1057 (2010).

[101] R. Haussmann, M. Punk, and W. Zwerger, Phys. Rev. A **80**, 063612 (2009).

[102] T. N. D. Silva, Journal of Physics B: Atomic, Molecular and Optical Physics **49**, 225301 (2016).

[103] R. B. Diener, R. Sensarma, and M. Randeria, Phys. Rev. A **77**, 023626 (2008).

[104] J. E. Drut, T. A. Lähde, and T. Ten, Phys. Rev. Lett. **106**, 205302 (2011).

[105] R. Rossi, T. Ohgoe, E. Kozik, N. Prokof'ev, B. Svistunov, K. Van Houcke, and F. Werner, Phys. Rev. Lett. **121**, 130406 (2018).

[106] N. Chandra, M. Kollar, and D. Vollhardt, Phys. Rev. B **59**, 10541 (1999).

# Acknowledgments

Having worked on the contents of this thesis for four years, I suppose some acknowledgments are in order. Let's start with a short version: I am very grateful to my promotor, ITF friends and colleagues, non-physics friends, girlfriend and family. It would be tedious to mention all of these people explicitly, so instead I'm taking the easy way out by acknowledging everyone using the cliché 'you know who you are'. Nevertheless, there are of course some people whose names I should mention.

Om te beginnen uiteraard mijn promotor Henk. Ik heb altijd genoten van onze samenwerking en ontzettend veel van je geleerd. Verder was het fijn dat ik vaak zo je kantoor kon binnenstappen, of bij een random ontmoeting in de koffiekamer een discussie kon starten. Ten slotte is het tof om met je baas een metalconcert te kunnen bezoeken. Stefan, ondanks dat je om bureaucratische redenen uiteindelijk niet officieel promotor bent, beschouwde ik onze discussies ook altijd als waardevol en leerzaam, tijdens zowel mijn promotie als mijn masterscriptie. Het was me eveneens een genoegen om onder jouw supervisie twee vakken te begeleiden.

Next, thanks to all of my colleagues that contributed to the nice atmosphere at the ITF. Ten eerste Guido, wie ik op het ITF waarschijnlijk in totaal het meest gezien heb de afgelopen jaren. Ik heb geluk gehad met jou als kantoorgenoot en zal je lampensmaak niet snel vergeten. Moreover, thanks to Simonas and Damian, who although I haven't seen them quite as much have still been nice office mates as well. Additionally, I thank Enea and Francisco for having been great master students to supervise, Wanda en Olga voor alle snacks op de donderdagen, Drian voor alle pizzatrips en dat we de PLaneTs hebben behoed voor uitsterven, Jorgos en Rembert voor de regelmatige concerten and all the (ex-)colleagues with whom I spent time during coffee breaks, sick lunch discussions, drinks, beer tastings, and so on. Tot slot bedank ik Erik voor zo'n 9 jaar aan discussies die me sowieso een betere natuurkundige hebben gemaakt en voor het zijn van mijn paranimf en een geweldige maat.

Al mijn niet-natuurkundige vrienden ben ik dankbaar voor de nodige afleiding van de wetenschap. In het bijzonder bedank ik Vince voor het fotograferen tijdens mijn promotie. Bastiaan, bedankt voor het last-minute ontwerpen van de kaft van mijn proefschrift en uiteraard voor de motivatie voor de vele klimsessies, waar ik anders waarschijnlijk al lang mee gekapt was. Stef, bedankt voor zo'n 9 jaar aan concerten, festivals, chillavonden, enzovoorts, en voor het zijn van mijn paranimf en grote broeder.

Verder bedank ik mijn familie, inclusief schoon- en aanplakfamilie, voor alle onvoorwaardelijke steun en dat soort dingen. In het bijzonder pap en mam, zonder wie ik geen opleiding en dus geen proefschrift had gehad. En Shauni, bedankt voor je speciale gave om na al die tijd nog steeds niet compleet gestoord van me te worden.

# About the author

I was born on the first of March in 1991 in Best, The Netherlands. In 2009, I obtained my high-school diploma cum laude at the Heerbeeck College in this same village. Afterwards, I enrolled in the bachelor's program Applied Physics at the Eindhoven University of Technology, where in 2012 I received my bachelor's degree cum laude. In the same year, I started the master's program Theoretical Physics at Utrecht University, which I concluded with a thesis on phase transitions of black holes and magnetic AdS black branes in $\mathcal{N} = 2$ supergravity, under supervision of prof. Stefan Vandoren. After I obtained my master's degree cum laude in 2014, I started as a PhD candidate at the Institute for Theoretical Physics at Utrecht University, under supervision of prof. Henk Stoof. This thesis contains the results of my PhD research.